Non- Abelian gauge theory for Rashba and Dresselhaus Spin-Orbit Interaction

Nelson Bolívar

Collégium Sciences et Techniques
École Doctorale Energie Mécanique et Matériaux (EMMA)

Facultad de Ciencias
Escuela de Física

Thèse présentée pour l'obtention du titre de
Docteur de l'Université de Lorraine
en Sciences Physiques de la Matière Condensée
par **Nelson Bolívar**

Théorie de jauge non abélienne pour l'interaction spin-orbite de Rashba et Dresselhaus

Rashba and Dresselhaus Spin Orbit Interactions as Non-Abelian Gauge Field Theory

Membres du jury:

Rapporteurs:	Carmen Muñoz	Professeur, Instituto de Ciencia de Materiales de Madrid
	Francisco Mireles	Professeur, Centro de Nanociencias y Nanotecnología-UNAM
Examinateurs:	Bart van Tiggelen	Directeur de Recherche CNRS
	Daniel Malterre	Professeur, Université de Lorraine
Invitée:	Anamaría Font	Professeur, Universidad Central de Venezuela-UCV
Co-directeurs:	Ernesto Medina	Professeur, IVIC/Universidad Central de Venezuela-UCV
	Bertrand Berche	Professeur, Université de Lorraine

Institut Jean Lamour - Statistical Physics Group
Faculté des Sciences & Technologies - 54500 Vandœuvre-lès-Nancy

Rashba and Dresselhaus Spin Orbit Interactions as Non-Abelian Gauge Field Theory

by

Nelson Bolívar

A thesis submitted for the award of
Doctor of Philosophy

Facultad de Ciencias, Universidad Central de Venezuela (Venezuela)

Escuela de Física

Institut Jean Lamour, Université de Lorraine (France)

Ecole Doctorale Energie Mécanique et Matériaux

September 26, 2014

Acknowlegements

There are countless people to whom I want to say "Thank you". Those people who happened to be in any connection to me and my work during the time of my PhD at the Faculty of Science at U.C.V. and in the Group of Statistical Physics, at the University of Lorraine, have been supporting, friendly and always there to guide me in some way. I wouldn't have managed to solve all of those huge bureaucratic questions without their help, both inside and outside the campus. I want to thank the warm atmosphere they offered me in Nancy, which at some moments reminded me the tropical of my own country.

I am incredibly grateful to my scientific supervisors Bertrand Berche and Ernesto Medina, whom I consider my friends, for the invaluable guidance and encouragement throughout the period of this work.

I also want to thank everybody who showed interest in my work and came to me with their questions, remarks and suggestions, which often were very useful.

The financial support by the Ecole Doctorale (EMMA) that enabled me to study for the Degree of PhD is especially acknowledged.

Last but not least I am sincerely thankful to my two families, my parents and brothers, the Bolívars, and the Taylors, specially to Sofi. They all have been the balance and the most supportive people during this period. To all my friends for their support, their jokes and the good times throughout my studies. And simply for being such important people for me.

Contents

Introduction

The present thesis is devoted to the understanding of persistent currents in two dimensional or quasi-two dimensional (quasi-2D) mesoscopic systems. Those systems are widely known in a large range of materials, like superconductors, semiconductors and Graphene [1, 2, 3]. Our aim is to obtain a deeper understanding in closed geometries, such as rings, and derived its electronics and topological properties. In particular we are interested in one dimensional rings also called Aharonov-Bohm rings, which offers a primary ground for studying the topology consequences on each material, but also they are a wonderful playground to test both, numerical and analytical techniques in quantum mechanics, that may reveal in the simplest systems a rich variety of phenomena. We stressed through the work that these phenomena are also achievable through experimental set-ups, setting the variables an parameters in the best of the known experiments at this moment.
First, we will briefly review heterostructures, where the charge carriers are confined to form a set of discrete energy levels. In this materials spin degeneracy of electrons and holes is due to the combine effect of inversion symmetry in space and time, when the confining potential through which the carriers move is inversion-asymmetric the spin degeneracy is removed, even in the absence of an external magnetic field $\boldsymbol{B}$. In heterostructures, this spin splitting can be the consequence of a bulk inversion asymmetry (BIA) of the underlying crystal (e.g. a zinc blende structure [4]), and of a structure inversion asymmetry (SIA) of the confinement potential [5]. The splitting due to SIA is known as Rashba Spin Orbit interaction and the BIA splitting the Dresselhaus Spin Orbit interaction.

The SIA can be achieved or even tuned by applying a transversed electric field, making it suitable for spin-electronic dynamics. In a material with this properties, shaped in a ring geometry, some interesting phenomena occurs, such as the charge and spin persistent currents. These currents are the result of the band-structure of the material and a shifting of the wave-vector due

the gauge field associated to a static magnetic field, leading to a motion of the electrons in the loop [6], which in summary is an electrical current flowing around a ring which is constant in time and which is not driven by a power source external to the ring. For the persistent current in a ring to be measurable, the ring must be cold ($\leq 1K$) and small ($\leq 1\mu m$). This characteristic behavior leaded us to the questions of whether it is possible to achieve spin filtering by means of interferometry in loops. We proposed a device based on a Mach-Zehnder interferometer, which is an apparatus that is intended to determine the relative phase shift between two beams derived by splitting a unique source. In this work, already published [7], we consider a two-dimensional system consisting of noninteracting electrons subject to both Rashba and Dresselhaus spinorbit interactions. The device has two beam splitters and mirrors, the first can be implemented with a combination of quantum point contacts that absorb the electron beam and transmits one electron a the time. This is done with equal probability on each arm direction in the interferometer.

The amplitudes collected into the final detectors can be modeled by generalized comparator transmission and reflection matrices and obtain the conditions on to achieved spin filtering.

In the same order of ideas we studied a different closed geometry [8], we addressed the electronic states of a mesoscopic ring in the presence of Rashba Spin Orbit coupling and a $U(1)$ gauge field. Formulating a spin symmetric coupling to an ideal lead we implemented a voltage probe following Büttiker's approach [9]. The lead coupled to a reservoir that supplied decoherent electrons to the system. We studied the spin and charge persistent currents, computed in the presence of a Rashba interaction and we found two distinct scenarios for the electron filling, each one translates into two different behaviors of the currents. The degradation of the persistent currents depends uniformly on the reservoir coupling charaterized by ϵ but due to the fact that currents emerge from different depths of the fermi sea, they depend non uniformly in temperature, this "shields" the currents with a protective gap.

We approached a non-Abelian gauge formulation for the Rashba and Dresselhaus hamiltonians, which is relevant in spintronics of non-centrosymmetric materials. The gauge fields defined are proportional to the $SU(2)$ generators and also to potential gradients of extrinsic and intrinsic origin which results in a $U(1) \times SU(2)$ formulation. We derived from the corresponding Lagrangian the equations of motion and conserved spin currents. It is shown that the mandatory presence of a Proca mass type term fixes the gauge and solves in consequence the gauge dependence of the spin current and therefore the ambiguities of the spin current reported in the literature. The invariant gauge subgroup of this theory will be studied.

It will also lead us to the study of the spin-orbit coupling in an interesting and recent approach, the non-abelian $SU(2)$ gauge theory formulation.
We studied a non-Abelian gauge formulation for the Rashba and Dresselhaus hamiltonians, which is relevant in spintronics of non-centrosymmetric materials, those that do not posses a point group with an inversion center. In this formulation the gauge fields defined are proportional to the Pauli matrices, the $SU(2)$ generators, and also to potential gradients due to SO interaction of extrinsic and intrinsic origin. This results in a $U(1) \times SU(2)$ theory for the SO coupling already studied in the literature [10, 11]. We derived from the corresponding Lagrangian of this theory the equations of motion and the conserved spin currents [12]. It is shown that the mandatory presence of a Proca mass type term fixes the gauge and solves in consequence the gauge dependence of the spin current and therefore clears the ambiguities of the spin current reported in the literature [13].

Finally the problem of persistent charge and spin currents is addressed on a Corbino disk built from a graphene sheet. The growing interest in graphene and graphene-like materials, a 2-dimensional carbon material [14], raises questions about how Aharonov graphene rings will behave. The interesting properties of graphene around in the vicinity of the Dirac points, gapless points in the band-structure, made graphene a unique material. In these points the electron behave like masless particles, obeying Dirac equation. An extensive study of this materials have been done in the tight-binding approach with some specific boundary conditions [15, 16]. Recent works has shown that is possible to write a continuous derivation of these boundary conditions so we can consider the boundary as a wave function phase and find analytical expressions for persistent charge and spin currents [17].
In our work [18], we consistently derive the Hamiltonian including kinetic, intrinsic (ISO) and Rashba spin-orbit interactions in cylindrical coordinates. The Hamiltonian is carefully considered to reflect hermiticity and covariance. We use the linear response definition in order to determine the charge persistent currents. We also determine the spin and pseudo spin polarizations associated with such equilibrium currents. For the intrinsic case one can also compute the correct currents by properly defining the bare velocity operator associated with ISO problem or alternatively the ISO group velocity operator associated with the free case. Charge currents for both SO couplings reach maximal values in the vicinity of half integer flux quanta. Such maximal currents are protected from thermal effects because contributing levels plunge ($\sim$1K) into the Fermi sea at half integer flux values. Such a mechanism, makes them observable at

readily accessible temperatures. Spin currents only arise for the Rashba coupling, due to the spin symmetry of the ISO spectrum. For the Rashba coupling, spin currents are cancelled at half integer fluxes but they remain finite in the vicinity, and the same scenario above protects spin currents.
The main results of this thesis are published in: [7, 8, 12, 13, 18].

The set-up of the thesis is the following. In chapter 1 we give a brief review of heterostructures, sketching the Kane model and how the microscopic approach give birth to SO coupling in condensed matter. In chapter 2 we introduce persistent currents, both charge and spin and the most relevant temperature effects in the literature. Chapter 3 is devoted to introduce the non-Abelian formulation of the SO interaction and the computation of the Noether currents. In chapter 4 an interferometer device is propose as a spin filtering apparatus that take advantage of the SO coupling and its non-Abelian formulation ina 2-dimensional gas. A mesoscopic ring is studied in chapter 5, including spin effects when coupled to a reservoir. The chapter 6 dedicates to introduce graphene. Finally in chapter 7 we develop a corbino graphene ring and study the persistent currents. Conclusions are collected in the last chapter.

Chapter 1

Spin-Orbit Coupling in a Quasi-2 Dimensional Electron Gas

In this chapter we review the microscopic origin of the SO coupling in the interface between semiconducting materials where is possible to form a quasi-2 dimensional structure due to the confining of the electrons in the junction. A brief sketch of the $\boldsymbol{k} \cdot \boldsymbol{p}$ method is used to obtain the relevant parameters in the microscopic structure of semiconductors junctions, based mostly in the work of Winkler [1].

1.1 Heterostructures

The Spin Orbit Coupling (SOC) is responsible for affecting the spin degrees of freedom by the orbital state of the electron. This gives room for a variety of phenomena as the doubling of spin states, anomalous Hall effect in ferromagnetic materials and effects of electronic delocalization. The SOC brings a new kind of universality class, the symplectic class, which is added to the well known orthogonal and unitary ones, associated to the classification of the conducting states in electronic systems weakly disordered.

The SOC in atomic systems is described by the non-relativistic approximation at low energies of the Dirac equation. The non-relativistic limit can be obtained in a consistent form by a canonical Foldy-Wouthuysen transformation of the Dirac equation, where after keeping the low

order in $1/2m_0c^2$ we obtain [11],

$$\Delta H = -\frac{\hbar}{4m_0^2c^2}\boldsymbol{\sigma}\cdot(\mathbf{p}\times\mathbf{E}) - \frac{e\hbar^2}{8m_0^2c^2}\nabla\cdot\mathbf{E}, \tag{1.1}$$

where the first term is identified as the SOC, and the second is called the Darwin term. Here $\mathbf{E} = -\boldsymbol{\nabla}\Phi$ where Φ is the electromagnetic potential, m_0 is the electron bare mass and $\boldsymbol{\sigma}$ is the Pauli matrices vector.

In a given periodic potential the electronic states are characterized by the energy bands. The SOC in this cases has remarkable effects on these band structure when electric fields are present, for instance in non-centrosymmetric semiconductors the SOC splits the p valence bands, opening a gap that is proportional to the interaction strength.

Let us focus on the interface between several semiconductors, that forms a heterostructure. The semiconductors forming such a system must have similar crystal structure, with close band structure. A compound as the GaAs has a lattice constant $a_0 \approx 5.65325$Å and other compounds of the type $Al_xGa_{1-x}As$ has $a_0 = 5.65330$Å. The small difference is around a 0.00005 which make then suitable to form a heterostructure. Since the fundamental gap in each semiconductors is different, each band is shifted in energy respect to the other creating a discontinuity between the conduction bands. To make this clear let us consider a heterojunction between two materials with fundamental gaps related by $E_g^A < E_g^B$. According to the electron affinity rule the ground levels for both semiconductor are aligned. The offset is given by the lower edge of the conduction band and the vacuum level. For $Al_{0,3}Ga_{0,7}As$ and GaAs is $\Delta E_c = 0.33$eV and for the valence band $\Delta E_v = 0.04$eV. The energy gap of $Al_{0,3}Ga_{0,7}As$ is larger than the GaAs. An heterostructure formed by two layers of $Al_{0,3}Ga_{0,7}As$ and one central layer of GaAs creates a potential well that traps the charge carriers. The charge carriers are introduced by doping the system, in the case of semiconductors type-n as n-$Al_xGa_{1-x}As$ the doping is made with silicon atoms. A drawback of doping this way is that the impurities after donating electron or holes are left electrically charged, causing Coulomb scattering, and diminishing the carriers mobility also introducing decoherence in the system. This may affect the topological effects on the wavefunctions, by erasing the phases acquired by the electrons and create energy gaps. A remote doping can solves the scattering situation, this is achieved for example by creating a junction between an intrinsic and a type-n semiconductor. If the type-n

has a larger gap than the intrinsic then the electrons will migrate from the donor impurities in the type-n to the intrinsic semiconductor. The electric field generated by the impurities deform the energy conduction band and the electrons are trapped in the junction forming a Quasi 2-dimensional electron gas (2DEG).

1.2 Band structure of semiconductors with SOC

As we stated before, the SOC naturally arises from the non relativistic limit of the Dirac equation, by performing successive canonical transformations in order to eliminate the lower components in the Dirac spinor [19]. The full resulting Hamiltonian is the following

$$H = \left[\frac{\boldsymbol{\Pi}^2}{2m_0} + e\phi\right] \mathbb{1}_{2\times 2} - \left[\frac{\boldsymbol{\Pi}^4}{8{m_0}^3c^2} - \frac{e\hbar^2}{8{m_0}^2c^2}\boldsymbol{\nabla}\cdot\boldsymbol{E}\right] \mathbb{1}_{2\times 2} - \frac{e\hbar}{2m_0}\boldsymbol{\sigma}\cdot\boldsymbol{B} + \frac{e\hbar\boldsymbol{\sigma}\cdot\boldsymbol{\Pi}\times\boldsymbol{E}}{4{m_0}^2c^2}, \quad (1.2)$$

where the Pauli matrices are $\boldsymbol{\sigma} = (\sigma_x, \sigma_y, \sigma_z)$ and $\boldsymbol{\Pi} = \boldsymbol{p} - e\boldsymbol{A}$ is the kinetic momentum associated to the potential vector $\boldsymbol{A}$.
The first term corresponds to the usual kinetic Hamiltonian with an external electric potential ϕ. The second describes the first relativistic correction to the kinetic energy and the Darwin term that we showed in equation 1.1. The third is the Zeeman interaction describing the coupling between the spin the electron and a magnetic field. Finally the last contribution is the SOC, showed also in equation 1.1, which couples the spin of the electron to its orbital motion in the presence of an electric field.

For states defined over a periodic lattice, the spinors are Bloch functions of the form

$$u_{\nu\boldsymbol{k}} = \sum_{\nu'} c_{\nu'}(\boldsymbol{k}) u_{\nu' 0}, \quad (1.3)$$

where ν labels the energy band including the spin state and the wave vector is restricted to the first Brillouin zone.
The Schrödinger equation for the electron in a periodic potential, in the presence of an electric potential $V_0(\boldsymbol{r})$ is given by,

$$\left(\frac{\boldsymbol{p}^2}{2m_0} + V_0(\boldsymbol{r}) - \frac{\hbar\boldsymbol{\sigma}\cdot\boldsymbol{p}\times\nabla V_0(\boldsymbol{r})}{4{m_0}^2c^2}\right)\psi = E\psi, \quad (1.4)$$

We obtain a $\boldsymbol{k}$ dependent Hamiltonian expanding around $\boldsymbol{k} \approx 0$ and keeping only terms of order $\hbar\boldsymbol{k}$, which gives

$$H_{\boldsymbol{k}\cdot\boldsymbol{p}} = \left(\frac{\boldsymbol{k}^2}{2m_0} + V_0(\boldsymbol{r}) + \frac{\hbar}{4{m_0}^2c^2}\boldsymbol{k}\cdot\boldsymbol{\sigma}\times\nabla V_0(\boldsymbol{r}) \right). \tag{1.5}$$

The eigenstates of this Hamiltonian are associated with the bands borders, and form a complete basis from which we can expand the Bloch function, which integrated over a unit cell gives,

$$\sum_{\nu'} \left\{ \left(E_{\nu 0} - E_{\nu\boldsymbol{k}} + \frac{\hbar^2\boldsymbol{k}^2}{2m_0} \right) \delta_{\nu\nu'} + \frac{\hbar}{m_0}\boldsymbol{k}\cdot\langle\nu 0|\,\boldsymbol{p} + \frac{\hbar}{4m_0c^2}\left(\boldsymbol{\sigma}\times\nabla V_0(\boldsymbol{r})\right)|\nu' 0\rangle \right\} c_{\nu'}\left(\boldsymbol{k}\right) = 0. \tag{1.6}$$

The matrix element of the second term, the $\boldsymbol{k}\cdot\boldsymbol{p}$ term, is the SOC that mixes the band edges.

1.3 The Kane model

The model principle rests on the solution of the Hamiltonian (1.6) over a finite basis. Kane noted that for type III-V semiconductors the valence band edge v_t given by the p orbitals and the edge of the conduction band Γ_{6c} given by the s orbitals are close to each other. In the GaAs this separation is around $E_G \approx 1.5$eV, and both bands are significantly separated from the others.

The basis functions are eigenfunctions of the crystal Hamiltonian 1.5,

$$H_{\boldsymbol{k}\cdot\boldsymbol{p}}(\boldsymbol{k}=0)u_{\nu 0} = E_{\nu 0}u_{\nu 0}. \tag{1.7}$$

Since the crystal potentials are usually complicated functions, we solve the system around the most symmetric points in the Brillouin zone, giving the v_t and the Γ_{6c} points, and looking for the change under some specific symmetry group. The symmetry of the Bloch function of some specific band is the same of its respective orbital near the band edge. Then the functions are such that

$$\psi_{n,j,m_j} = \sum_{m,s} C_m^{CG} R_{nl}(r) Y_l^m(\theta,\varphi)\otimes\sigma_{m_s}.$$

the m, l and m_s are the usual angular momentum and spin quantum numbers with spin $s = 1/2$. The C_m^{CG} are the Clebsch-Gordan coefficients, the Y_l^m are spherical harmonics and σ_{m_s} is the space of the spin degree of freedom. The basis is constructed in such a way that the SOC is

Γ_j	J	m_j	ψ_{j,m_j}	E_j
Γ_{6c}	$1/2$	$1/2$	$\|S\uparrow\rangle$	E_c
Γ_{6c}	$1/2$	$-1/2$	$\|S\downarrow\rangle$	E_c
Γ_{8v}	$3/2$	$1/2$	$\left\|\frac{3}{2},\frac{1}{2}\right\rangle = -\sqrt{\frac{2}{3}}\|Z\uparrow\rangle - \sqrt{\frac{1}{6}}\|(X+iY)\downarrow\rangle$	E_v
Γ_{8v}	$3/2$	$-1/2$	$\left\|\frac{3}{2},-\frac{1}{2}\right\rangle = \sqrt{\frac{1}{6}}\|(X-iY)\uparrow\rangle + \sqrt{\frac{2}{3}}\|Z\downarrow\rangle$	E_v
Γ_{8v}	$3/2$	$3/2$	$\left\|\frac{3}{2},\frac{3}{2}\right\rangle = -\sqrt{\frac{1}{2}}\|(X+iY)\uparrow\rangle$	E_v
Γ_{8v}	$3/2$	$-3/2$	$\left\|\frac{3}{2},-\frac{3}{2}\right\rangle = \sqrt{\frac{1}{2}}\|(X-iY)\downarrow\rangle$	E_v
Γ_{7v}	$1/2$	$1/2$	$\left\|\frac{3}{2},\frac{1}{2}\right\rangle = \sqrt{\frac{1}{3}}\|Z\uparrow\rangle - \sqrt{\frac{1}{3}}\|(X+iY)\downarrow\rangle$	$E_v-\Delta_0$
Γ_{7v}	$1/2$	$-1/2$	$\left\|\frac{3}{2},-\frac{1}{2}\right\rangle = -\sqrt{\frac{1}{3}}\|(X-iY)\uparrow\rangle + \sqrt{\frac{1}{3}}\|Z\downarrow\rangle$	$E_v-\Delta_0$

Table 1.1: Basis functions $|j, m_j\rangle$ in the Kane model

diagonal. The SOC is proportional to $\boldsymbol{L}\cdot\boldsymbol{S}$ which in terms of the total angular momentum is $(J^2 - L^2 - S^2)/2$.

The Bloch basis that comes from the Hamiltonian 1.5 has at the edge (Γ_{6c}, v_t) the same symmetry than the corresponding orbital functions. With the last we form a orbital basis where the Hamiltonian is diagonal. The symmetry can be seen in the labels $\{j, m_l, l, s\}$. In the $s = 1/2$ scenario Γ_{6c} has the same symmetry than the orbital functions s, with $l = 0$ and then $j = 1/2$. The valence edge v_t has the same symmetry than the p orbitals, with $l = 1$ then only the values $j = 1/2$ or $j = 3/2$ are allowed. The SOC has no effect on the Γ_{6c} states, where it affects the v_t states degenerating it in Γ_{8v} and Γ_{7v}.

In the table 1.1 we identify the elements of the basis $\{u_{\nu 0}\}$. Using this basis functions we can compute the matrix elements of the Hamiltonian (1.5).

$$H_{8\times 8} =$$

	$\lvert S\uparrow\rangle$	$\lvert S\downarrow\rangle$	$\left\lvert \frac{3}{2},\frac{3}{2}\right\rangle$	$\left\lvert \frac{3}{2},\frac{1}{2}\right\rangle$	$\left\lvert \frac{3}{2},-\frac{1}{2}\right\rangle$	$\left\lvert \frac{3}{2},-\frac{3}{2}\right\rangle$	$\left\lvert \frac{1}{2},\frac{1}{2}\right\rangle$	$\left\lvert \frac{1}{2},-\frac{1}{2}\right\rangle$
$\langle S\uparrow\rvert$	$E_c+\frac{\boldsymbol{k}^2}{2m_0}$	0	$-\frac{1}{\sqrt{2}}P\hbar k_+$	$\sqrt{\frac{2}{3}}P\hbar k_z$	$\frac{1}{\sqrt{6}}P\hbar k_-$	0	$-\frac{1}{\sqrt{3}}P\hbar k_z$	$-\frac{1}{\sqrt{3}}P\hbar k_-$
$\langle S\downarrow\rvert$	0	$E_c+\frac{\vec{k}^2}{2m_0}$	0	$-\frac{1}{\sqrt{6}}P\hbar k_+$	$\sqrt{\frac{2}{3}}P\hbar k_z$	$\frac{1}{\sqrt{2}}P\hbar k_-$	$-\frac{1}{\sqrt{3}}P\hbar k_+$	$\frac{1}{\sqrt{3}}P\hbar k_z$
$\left\langle \frac{3}{2},\frac{3}{2}\right\rvert$	$-\frac{1}{\sqrt{2}}P\hbar k_-$	0	$E_v+\frac{\vec{k}^2}{2m_0}$	0	0	0	0	0
$\left\langle \frac{3}{2},\frac{1}{2}\right\rvert$	$\sqrt{\frac{2}{3}}P\hbar k_z$	$-\frac{1}{\sqrt{6}}P\hbar k_-$	0	$E_v+\frac{\vec{k}^2}{2m_0}$	0	0	0	0
$\left\langle \frac{3}{2},-\frac{1}{2}\right\rvert$	$\frac{1}{\sqrt{6}}P\hbar k_+$	$\sqrt{\frac{2}{3}}P\hbar k_z$	0	0	$E_v+\frac{\vec{k}^2}{2m_0}$	0	0	0
$\left\langle \frac{3}{2},-\frac{3}{2}\right\rvert$	0	$\frac{1}{\sqrt{2}}P\hbar k_+$	0	0	0	$E_v+\frac{\vec{k}^2}{2m_0}$	0	0
$\left\langle \frac{1}{2},\frac{1}{2}\right\rvert$	$-\frac{1}{\sqrt{3}}P\hbar k_z$	$-\frac{1}{\sqrt{3}}P\hbar k_-$	0	0	0	0	$E_v-\Delta_0+\frac{\vec{k}^2}{2m_0}$	0
$\left\langle \frac{1}{2},-\frac{1}{2}\right\rvert$	$-\sqrt{\frac{2}{3}}P\hbar k_+$	$\frac{1}{\sqrt{3}}P\hbar k_z$	0	0	0	0	0	$E_v-\Delta_0+\frac{\vec{k}^2}{2m_0}$

(1.8)

The eigenvalues are then given by

$$E_c\left(\boldsymbol{k}\right) = \frac{\hbar^2\boldsymbol{k}^2}{2m_0} + \frac{\hbar^2\boldsymbol{k}^2P^2\left(E_G + 2\Delta_0/3\right)}{E_G\left(E_G+\Delta_0\right)}, \tag{1.9}$$

$$E_{hp}\left(\boldsymbol{k}\right) = -E_G + \frac{\hbar^2\boldsymbol{k}^2}{2m_0}, \tag{1.10}$$

$$E_{hl}\left(\boldsymbol{k}\right) = -E_G + \frac{\hbar^2\boldsymbol{k}^2}{2m_0} - \frac{2\hbar^2\boldsymbol{k}^2P^2}{3E_c}, \tag{1.11}$$

$$E_{SO}\left(\boldsymbol{k}\right) = -E_G - \Delta_0 + \frac{\hbar^2\boldsymbol{k}^2}{2m_0} - \frac{\hbar^2\boldsymbol{k}^2P^2}{3\left(E_c+\Delta_0\right)}, \tag{1.12}$$

where $E_G = E_c - E_{\Gamma_8}$ is the fundamental gap and P are the momentum matrix elements, which are wrote explicitly in equation (1.17). The relation of the eigenvalues (1.8) with each band becomes clear when $\boldsymbol{k}$ is written on the quantization axis of the total angular momentum, also since we are interested in adjacent bands around $\boldsymbol{k} \approx 0$, the SOC is only fully considered in these adjacent states. Expanding to second order in perturbation we can classify the states according to their effective masses. The energies are,

$$E_\nu(\boldsymbol{k}) = E_\nu(\boldsymbol{0}) + \frac{\hbar^2\kappa^2}{2m_\nu^*}, \tag{1.13}$$

where,

$$\frac{m_0}{m_\nu^*} = 1 + \frac{2}{m_0}\sum_{\nu'}\frac{P_{\nu\nu'}^2}{E_\nu(\boldsymbol{0}) - E_\nu'(\boldsymbol{0})}. \tag{1.14}$$

The leading contribution is observed in the coupling $P_{\nu\nu'}$ between the adjacent bands ν and ν', and their difference in energy. Then for the effective mass of the valence band m_v^* and the conduction band m_c^* it is a good approximation to use

$$\frac{m_0}{m_{c/v}^*} \approx \frac{2}{m_0}\frac{P_{cv}^2}{E_0}, \tag{1.15}$$

where $E_0 = E_c - E_v$ is the band gap, E_c and E_v are the minimal energy of the conduction band and the maximum of the valence band.

Finally, the Hamiltonian confined into a potential ϕ is,

$$\begin{aligned} H &= \frac{P^2}{3}\Big[\frac{2}{E_0}+\frac{1}{E_0+\Delta_0}\Big]\boldsymbol{k}^2 + V + \frac{P^2}{3}\Big[\frac{1}{E_0}-\frac{1}{E_0+\Delta_0}\Big]\frac{e}{\hbar}\boldsymbol{\sigma}\cdot\boldsymbol{B} \\ &+\frac{eP^2}{3}\Big[\frac{1}{E_0^2}-\frac{1}{(E_0+\Delta_0)^2}\Big]\boldsymbol{\sigma}\cdot\boldsymbol{k}\times\boldsymbol{E} - \frac{eP^2}{6}\Big[\frac{2}{E_0^2}-\frac{1}{(E_0+\Delta_0)^2}\Big]\nabla\cdot\boldsymbol{E}. \end{aligned} \quad (1.16)$$

where the particular coefficients depend on the crystal parameters, E_0 and its matrix elements Δ_0 defined by,

$$\boldsymbol{P}_{\substack{\nu\nu'\\ \sigma\sigma'}} = \langle\nu\sigma|\,\boldsymbol{\Pi}\,|\nu'\sigma'\rangle \quad (1.17)$$

$$\Delta_{\substack{\nu\nu'\\ \sigma\sigma'}} = \frac{\hbar}{4m_0^2c^2}\langle\nu\sigma|\,[\boldsymbol{p}\cdot\boldsymbol{\sigma}\times(\nabla V)]\,|\nu'\sigma'\rangle\,. \quad (1.18)$$

The coefficients are calculated by the Envelope Function Approximation.

1.4 Envelope Function Approximation

The Envelope Function Approximation (EFA) allows us to describe electrons and holes in the presence of magnetic and electric fields, which evolves slowly compare to the length scale of the lattice constant. Let us consider the Schrödinger equation,

$$\left(\frac{(\boldsymbol{p}-e\boldsymbol{A})^2}{2m_0}+V_0(\boldsymbol{r})-\frac{\hbar\boldsymbol{\sigma}\cdot(\boldsymbol{p}-e\boldsymbol{A})\times\nabla V_0(\boldsymbol{r})}{4{m_0}^2c^2}+V(\boldsymbol{r})-\frac{e\hbar}{2m_0}\boldsymbol{\sigma}\cdot\boldsymbol{B}\right)\psi(\boldsymbol{r}) = E\psi(\boldsymbol{r}) \quad (1.19)$$

where $V_0(\boldsymbol{r})$ is a microscopic lattice potential and $V(\boldsymbol{r})$ a slowly varying potential. Similarly to the derivation of the $\boldsymbol{k}\cdot\boldsymbol{p}$ method we expand the wave function in term of the band edge Bloch functions.

$$\psi(\vec{r}) = \sum_{\nu'} f_{\nu'}u_{\nu'0}(\vec{r}). \quad (1.20)$$

The function $f_{\nu'}$ modulates the Bloch functions. Considering that the $V(\boldsymbol{r})$ and $A(\boldsymbol{r})$ potentials vary slowly inside a unit cell, then,

$$\sum_{\nu'}\left[\left(E_{\nu'}(0)+\frac{\boldsymbol{\Pi}^2}{2m_0}+V(\boldsymbol{r})\right)\delta_{\nu,\nu'}+\Delta_{\nu,\nu'}-\frac{e\hbar}{2m_0}\boldsymbol{\sigma}\cdot\boldsymbol{B}\delta_{\nu,\nu'}+\frac{\boldsymbol{\Pi}\cdot\boldsymbol{P}_{\nu,\nu'}}{m_0}\right]f_{\nu'}=Ef_{\nu'}, \quad (1.21)$$

where

$$\boldsymbol{P}_{\nu,\nu'}=\langle\nu|\,\boldsymbol{\Pi}\,|\nu'\rangle\,, \quad (1.22)$$

$$\Delta_{\nu,\nu'}=\langle\nu|\left(\frac{\hbar}{4m_0^2c^2}\boldsymbol{\Pi}\cdot\boldsymbol{\sigma}\times(\nabla V_0)\right)|\nu'\rangle\,.$$

Finally this Hamiltonian contains all the information about the crystal periodicity and the fields present.

Chapter 2

Persistent Charge and Spin Currents

In this chapter we define the Persistent currents based mostly on the seminal work of Büttiker [9]. We focus on currents in metal rings as an introduction but considering also temperature effects. These will be the basis for calculating the corresponding currents in chapters 5 and 7.

2.1 Persistent Charge Currents

In [20] a remarkable aspect in quantum systems is considered, the modulation of the conductance enclosed by a magnetic flux modulated with a period of the fundamental quantum flux Φ_0, the Aharonov-Bohm effect. A small metallic ring threaded with an Aharonov-Bohm flux displays a persistent current, which is a sign of the quantum coherence in the ground state.
If we consider a conductor with disorder, the decoherence of an electron is due to its interaction with its environment, the coupling to localized spins, electron-phonon and $e-e$ interactions.
The presence of a magnetic flux Φ modifies the boundary condition for the electron wave function in an isolated ring, requiring dependence of the equilibrium free energy F upon Φ, this results in an equilibrium current,

$$I(\Phi) = -\frac{\delta F(\Phi)}{\delta \Phi}. \tag{2.1}$$

Due to the time reversal symmetry, the function $F(\Phi)$ is a even function of the magnetic flux Φ and also a periodic function in the quantum flux $\Phi_0 = \frac{h}{e}$, then $I(\Phi)$ is periodic in a quantum flux. This current only makes sense in the presence of a magnetic field, even if it is constant and uniform. The quantity $F(\Phi)$ can be chosen in general depending of the variables that will

be kept constant in an experiment, the ensemble depends on the system. The following Fourier decomposition is valid,

$$F(\Phi) = \sum_{m=0}^{\infty} F_m \cos\left(\frac{2\pi m\Phi}{\Phi_0}\right) \tag{2.2}$$

$$I(\Phi) = \sum_{m=1}^{\infty} I_m \sin\left(\frac{2\pi m\Phi}{\Phi_0}\right), \tag{2.3}$$

where the relation $I_m = \frac{emF_m}{\hbar}$ holds.
It should be mentioned that a persistent current, as any charge current, generates a magnetic moment $M(\Phi) = \pi(L/2\pi)^2 I(\Phi)$ perpendicular to the ring.

2.1.1 Persistent Currents in Normal Metal Rings

Persistent currents in normal metals are already known to some extent, though are only verified in a few experiments. The magnitude of the current and its temperature dependence have been measured in experiments on single Au rings [21]. The current has also been observed in a semiconducting GaAs-AlGaAs heterostructure ring [22].
We will primarily be concerned with the current due to non-interacting electrons, the simplest possible model for the ring: a clean, one-dimensional ring.
Solving the Schrodinger equation for a single non interacting electron leads to plane waves solutions with,

$$k_n = \frac{2\pi}{L} n, \tag{2.4}$$

with L the characteristic length of the system, and n is an integer number that accounts for the quantization of the angular momentum due to the boundary conditions in the ring. After applying a magnetic field perpendicular to the ring, the Schrödinger equation is modified by an additional factor, $\mathbf{p} \to \mathbf{p} - \mathbf{eA}$, where the magnitude is $A = BL/4\pi$ when the field is constant. The magnetic flux through the ring is $\Phi = \frac{BL^2}{4\pi}$, so the wave vector changes as,

$$k_n = \frac{2\pi}{L} n + \frac{e}{\hbar} A = \frac{2\pi}{L}\left(n - \frac{\Phi}{\Phi_0}\right). \tag{2.5}$$

This translates in the energy levels of the electrons as a shifting by a factor proportional to the

magnetic flux,

$$\epsilon_n = \frac{4\pi^2\hbar^2}{2mL^2}\left(n - \frac{\Phi}{\Phi_0}\right)^2. \tag{2.6}$$

In quantum mechanics the introduction of a magnetic field coupled to the orbital degree of freedom is invariant under a gauge transformation, given by,

$$\boldsymbol{A}' \to \boldsymbol{A} - \boldsymbol{\nabla}\Lambda, \tag{2.7}$$

and in the wavefunctions through the phase,

$$\Psi' \to \mathrm{e}^{(-i\frac{e\Lambda}{\hbar})}\Psi, \tag{2.8}$$

where Λ is a smooth well behaved function of the position. Using the fact that $\boldsymbol{\nabla}\times\boldsymbol{\nabla}\Lambda = 0$, it is clear that the transformation leaves unchanged the physical field $\boldsymbol{B}$. Applying this to the wavefunction we obtain,

$$\begin{aligned}
\left(\boldsymbol{P} - e\boldsymbol{A}'\right)\Psi' &= (-i\hbar\boldsymbol{\nabla})\Psi' - \left(e\boldsymbol{A}' - e\boldsymbol{\nabla}\Lambda\right)\Psi' && (2.9)\\
&= \left(-i\hbar\mathrm{e}^{\left(-i\frac{e\Lambda}{\hbar}\right)}\boldsymbol{\nabla}\Psi - e(\boldsymbol{\nabla}\Lambda)\Psi'\right) - \left(e\boldsymbol{A} - e\boldsymbol{\nabla}\Lambda\right)\Psi' && (2.10)\\
&= \mathrm{e}^{\left(-i\frac{e\Lambda}{\hbar}\right)}\left(-i\hbar\boldsymbol{\nabla} - e\boldsymbol{A}\right)\Psi && (2.11)\\
&= \mathrm{e}^{\left(-i\frac{e\Lambda}{\hbar}\right)}\left(\boldsymbol{P} - e\boldsymbol{A}\right)\Psi. && (2.12)
\end{aligned}$$

As can be seen the transformation enters as an overall phase that has no impact on the expectation values of a given physical operator, but observables may be sensitive. Nevertheless Aharonov and Bohm[23], and Ehrenberg and Siday [24], showed that when two trajectories enclosing a magnetic flux interfere, this phase factor plays a role shifting the phase of the interference by an amount defined by the flux Φ. For the ring a gauge can be chosen such that,

$$\begin{aligned}
\Lambda &= -\frac{1}{2}a^2B\phi && (2.13)\\
&= -\Phi\frac{\theta}{2\pi}, && (2.14)
\end{aligned}$$

where a is the ring radius and ϕ the angular coordinate of the ring. Given this $\boldsymbol{\nabla}\Lambda = -\frac{\Phi}{L}\hat{\theta}$ and $\boldsymbol{A}' = 0$. Using the periodicity condition on the ring $\Psi(u) = \Psi(u+L)$, where $L = 2\pi a$ the

condition reads,

$$\Psi'(u+L) = \mathrm{e}^{2\pi i \frac{\Phi}{\Phi_0}} \Psi'(u). \tag{2.15}$$

Here $\Phi_0 = h/e$ is the fundamental quantum flux. This sets the periodicity of the wavefunctions depending on Φ and with period Φ_0, providing the allowed combinations of the functions that are characterized by the quantum number n. Since this is a general property of the Hamiltonian solutions, then all the properties of the system will carry the same periodicity, even in the presence of disorder.

A simple way to calculate the current is to consider an electron moving in the ring of circunference L. After one round it moves during a time $\Delta t = L/v$, being v the velocity of the particle. Its average current will be $i = -e/\Delta t = -ev/L$. The velocity is modulated by the magnetic field, since $\boldsymbol{v} = (P - e\boldsymbol{A})/m$. Calculating the mean value we obtain,

$$v = \Psi^\dagger \boldsymbol{v} \Psi = \frac{h}{mL}\left(n - \frac{\Phi}{\Phi_0}\right). \tag{2.16}$$

hence the current is,

$$i = -e\frac{h}{mL^2}\left(n - \frac{\Phi}{\Phi_0}\right). \tag{2.17}$$

Comparing with (2.6) we notice that the current can be calculated by,

$$i_n = -\frac{\partial \epsilon_n}{\partial \Phi}, \tag{2.18}$$

for each of the occupied states n. The total current is the sum over the occupied levels.

$$I = \sum_{occupied\ n} i_n. \tag{2.19}$$

2.1.2 Temperature Effects in the Persistent Charge Current

For many electrons, the relation is also valid, provided that there is no effective interaction between them. This assumption is specially appropiate in the case of metals since the long range interactions are suppressed by the charge screening. At some temperature T each of the

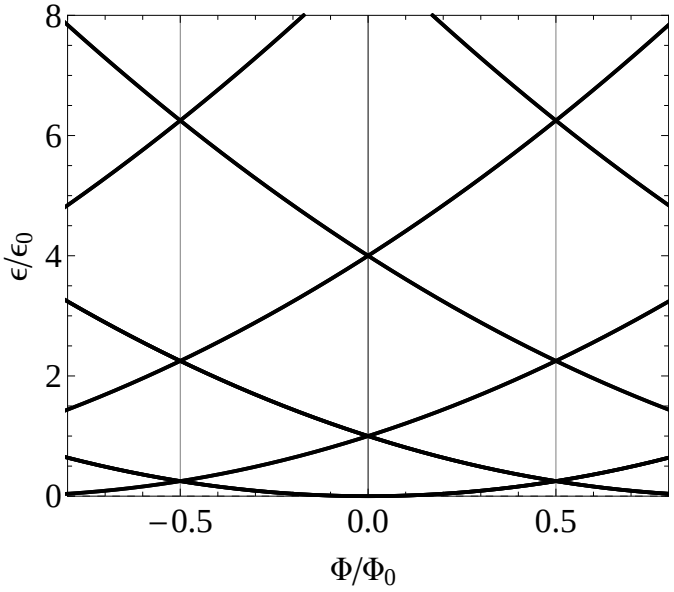

Figure 2.1: Energy (equation (2.6)) as a function of the magnetic flux in dimensionless units. $\epsilon_0 = \frac{h}{2mL^2}$

contributions to the current is weighted by the Fermi-Dirac distribution $f(\epsilon_n, \epsilon_F, T)$,

$$I = \sum_n f(\epsilon_n, \epsilon_F, T) i_n, \tag{2.20}$$

where ϵ_F is the Fermi level.

$$I = -\sum_n \left(1 + \mathrm{e}^{-\frac{(\epsilon_F - \epsilon_n)}{k_B T}}\right)^{-1} \frac{\partial \epsilon_n}{\partial \Phi}, \tag{2.21}$$

and n includes now the distinction for each spin state. When $T \to 0$ then $f(\epsilon_n, \epsilon_F, T) \to \Theta(\epsilon_F - \epsilon_n)$, the Heaviside function truncates the levels in a sum of single-level currents.
The currents are the slopes of the for each energy level in Fig.2.1. Each of the slopes of succesive leves are anti-correlated, the current of each electron level added to the ring will tend to cancel the contribution of the previous level, resulting in a current essentially dominated by the highest energy level.

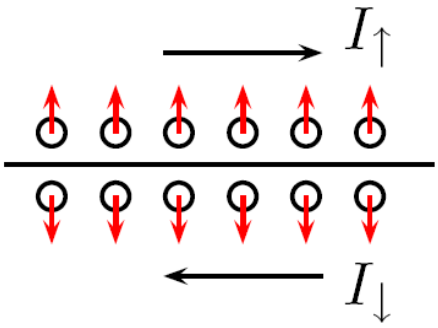

Figure 2.2: Intuitive definition of a pure Spin Current.

2.2 Persistent Spin Currents

It is well known the growing impact of spintronics in condensed matter due to its possible applications to technology. Spintronic devices are based on large changes in the resistance as a spin polarized current is pass through an interface where the polarization changes abruptly. The creation of more complex devices that include the spin degree of freedom as the fundamental, dynamical entities has been proposed, as the Datta and Das transistor [25]. Naturally a spin current is the expected quantity to be controlled. Actually this currents are constructed by means of ferromagnets that polarize the charge current, although is a simple solution, the construction of such devices at reduced scales has shown to be rather difficult. Alternative ways are being studied, such as the introduction of materials that interact with the spin directly and so the transport of spin can be manipulated.

A pure Spin Current is characterized for the absence of net charge transport. This can be quantified intuitively in a simple expression,

$$J_s = I_\uparrow - I_\downarrow, \tag{2.22}$$

the arrows representing the spin polarization of the charge currents.

A charge current flows in one direction, carrying a spin polarization. Another current flows in the reverse direction with carrying opposite spin polarization. The charge contribution to the total current vanishes. The spin polarization on the other hand will endure, manifesting as a

magnetic accumulation in both edges of the sample. Fig. 2.2.

$$J_c = I_\uparrow - I_\downarrow = 0 \tag{2.23}$$

$$J_s = I_\uparrow + I_\downarrow = 2I_\uparrow. \tag{2.24}$$

It is then ambiguous given this definition whether it is possible to measure a spin current directly or not, but through the spin accumulation (magnetization).

2.2.1 Spin Currents and Spin Hall Effect

The term Spin Hall Effect was introduced by Hirsch in 1999. It is indeed similar to the normal Hall effect, where charges of opposite signs accumulate at the sample boundaries due to the Lorentz force in a magnetic field. But there are significant differences. First, there is no need of magnetic field for spin accumulation, if a magnetic field perpendicular to the spin direction is applied, it will destroy the spin polarization. Second, the value of the spin polarization at the boundaries is limited by spin relaxation, and the polarization exists in relatively wide spin layers determined by the spin diffusion length, typically on the order of $1\mu m$. It originates from the coupling between charge and spin currents due to the SO interaction.It consists in a spin accumulation at the lateral boundaries of a current conductor, the direction of the spin are opposite at both boundaries.
The spin current can be introduced by a tensor J_i^a, where the a index is for the spin orientation and the index i is for the flow direction. If it is a pure current in the x direction, polarized in z, the only component different from zero is J_x^z. Under space inversion both spin and charge currents change sign, in contrast under time reversal inversion the charge current changes sign while spin current is symmetric. This is one of the mayor features of spin current, since it is a dissipationless current suitable for applications in new devices. A straightforward phenomena where two charge currents fulfill the conditions for spin current generation is the spin hall effect.

The standard way to define spin currents is through the equation,

$$J_i^a = \frac{1}{2} n \left\langle \sigma^a v_i + v_i \sigma^a \right\rangle, \tag{2.25}$$

which is basically the difference of the charge carriers currents with opposite spin, with n the

charge density. The spin Hall conductivity is defined

$$\sigma_{SH} = -\frac{J_i^a}{E_j}, \tag{2.26}$$

and it measures the conductivity due to a small electric field E_j applied.
It is tempting to describe spin transport in a scheme similar to the charge transport theory. Because of charge conservation, charge densities ρ_c and charge currents $\boldsymbol{J}_c$ satisfy the continuity equation $\rho_c + \boldsymbol{\nabla} J_c = 0$. For spin transport, we can consider the spin density S_i instead of ρ_c. The Definition (2.25) is the natural generalization of the charge model, nonetheless, spin-orbit coupling violates spin conservation, and the continuity equation for spin densities and currents does not hold. The spin orbit interaction can be seen in a simple picture, consisting in an interpretation as a Zeeman term, which in the case of Rashba is $-\boldsymbol{\sigma} \cdot B^{eff.}_{Rashba} = -\boldsymbol{\sigma} \cdot (\alpha p_\phi \boldsymbol{e}_\rho)$ and the precession axis of the spin rotates as the electron moves along. The equation (2.25) as definition of the spin current can be used as long as its limitations permit. Despite the fact that it cannot be directly related to spin accumulation, it is a useful model quantity to compare the effect of different spin-orbit coupling mechanisms. The continuity equation does not hold, but for instance, for some models it is possible to evaluate source terms [26], which are often termed as spin torque. Other definitions of spin currents have also been proposed. Analyzing the current of the total angular momentum $L_z + S_z$ [27] arguing that it vanishes for the Rashba Hamiltonian H_R due to the rotational invariance of H_R and that thus the presence or not of with impurities would determine angular momentum currents. A definition that is not proportional to $\langle \sigma^a v_i + v_i \sigma^a \rangle$ was proposed by Shi et al.[28] , is given as the time derivative of a "Spin displacement".

Chapter 3

Non-Abelian Formulation of the Spin Orbit Interaction

A reformulation of the spin-orbit (SO) coupling Hamiltonian in terms of non-Abelian gauge fields [29] was explicitly given in [30, 31] where the SO interaction is presented as a $SU(2)\times U(1)$ gauge theory. As the Yang-Mills gauge theory is well understood and is the underpinning of well established theory, enormous insight can be brought upon new problems. Such gauge point of view, in more general terms, has been known for some time [32, 33]. This formulation is very revealing, since the consistent gauge structure of the theory becomes obvious and the physics of spin currents, persistent currents and color diamagnetism [10] can be understood in a manner analogous to the well known $U(1)$ gauge theories. A consistent $SU(2) \times U(1)$ gauge approach was presented in reference [34, 11] where it was found that for the Pauli type Hamiltonians (including Rashba and two-dimensional reductions of the Dresselhaus Hamiltonian), Gauge Symmetry Breaking (GSB) is necessarily built into the theory and leads to the spin conductivity vanishing in constant electric fields [11]. In addition, the Yang Mills interpretation of the Rashba and Dresselhaus SO interactions renders the associated gauge fields real, with topological consequences analogous to the Aharonov Casher effect.

The Rashba and Dresselhaus SO interactions arise in materials which lack either structural or bulk inversion symmetry, respectively [35, 4]. These two kinds of interactions have recently been given a great deal of attention due to their potential role in the generation and manipulation of spin polarized currents, spin filters [36], spin accumulation [37], and spin optics [38].

3.1 Spin Orbit Interaction in Semiconductors

Spin-orbit interaction may be defined as the interaction of the spin of the electron, $\boldsymbol{\mu} = -g\frac{|e|}{2m}\boldsymbol{s}$ with the magnetic field produced by all external moving charges in the electron rest frame. Here $\boldsymbol{s} = \frac{1}{2}\hbar\boldsymbol{\sigma}$ is the spin of the electron with $\boldsymbol{\sigma}$ the Pauli matrices vector, $g \approxeq 2$ the Landé factor, m the bare mass of the electron and e the electron electric charge. In a semi-conductor, the electron rest mass and the Landé factor must be replaced by their effective counterparts, and the spin-orbit interaction can thus be considerably enhanced. Moreover, an appropriate basis in a crystalline solid is given in terms of the Bloch wave functions $\psi(\boldsymbol{r}) = u_{\boldsymbol{k}}(\boldsymbol{r})e^{\boldsymbol{k}\cdot\boldsymbol{r}}$, and the SO interaction must be calculated in this basis. Since the difficult to make this transformation the usual approach is to work with phenomenological expressions that are sensitive to the crystal symmetries. If there is bulk inversion asymmetry (BIA), the expression for the SO is the Dresselhaus term [1],

$$H_{D,3} = Ck_x(k_y^2 - k_z^2)\sigma_x + c.p. \tag{3.1}$$

where C is a constant and *c.p.* are cyclic permutations. In a two dimensional system the expectation value $\langle k_z\rangle \approx 0$ and $\langle k_z^2\rangle \approx (\pi/a)^2$, with a being the typical confinement length in the z direction, then, after neglecting cubic terms in k,

$$H_{D,2} = \beta(k_x\sigma_x - k_y\sigma_y). \tag{3.2}$$

For a space inversion asymmetry (SIA), where there is confinement potential that is not symmetric, the leading term is,

$$H_{D,2} = \alpha(\sigma_x k_y - \sigma_y k_x). \tag{3.3}$$

This is known as the Rashba SO contribution. This contribution can be tuned by an external electric field since it comes from the usual atomic expression, $\boldsymbol{\sigma}\cdot(\boldsymbol{k}\times\boldsymbol{\nabla}V)$, where V is the potential associated to the electric field, it could be the crystal field or an external field.

3.1.1 Non-Abelian gauge field approach of the Spin Orbit interaction

Consider the Pauli Hamiltonian,

$$H_P = \left(\frac{(\boldsymbol{p}-e\boldsymbol{A})^2}{2m} + V - e\phi\right)\mathbb{1}_{2\times 2} - \left(\frac{\boldsymbol{p}^4}{8m^3c^2} + \frac{e\hbar^2}{8m^2c^2}\boldsymbol{\nabla}\cdot\boldsymbol{E}\right)\mathbb{1}_{2\times 2} + \frac{e\hbar}{2m}\boldsymbol{\sigma}\cdot\boldsymbol{B} - \frac{e\hbar\boldsymbol{\sigma}\cdot(\boldsymbol{p}-e\boldsymbol{A})\times\boldsymbol{E}}{4m^2c^2}, \tag{3.4}$$

where the first term corresponds to the usual Schrödinger equation including the kinetic energy with a minimal coupling to the electromagnetic field, the potential denoted by V , that can be assumed periodic, and a scalar potential contribution. The second term describes the first relativistic correction to the kinetic energy and the Darwin term, where $\boldsymbol{E}$ is the electric field and c is the speed of light. These two terms are proportional to the 2×2 identity matrix in spin space. The third and fourth terms comprises explicitly spin-dependent terms, first the Zeeman interaction where $\boldsymbol{B}$ is the magnetic field and $\boldsymbol{\sigma}$ is the Pauli matrix vector and the second term is the spin-orbit interaction, now written with the minimal coupling to the gauge vector. We have assumed a static potential so that the curl of the electric field is absent. In order to suggest an $SU(2)\times U(1)$ form we can rewrite the Hamiltonian with $V=0$ as,

$$\begin{aligned} H &= \frac{1}{2m}\left((\boldsymbol{p}-e\boldsymbol{A})^2\mathbb{1}_{2\times 2} - 2(\boldsymbol{p}-e\boldsymbol{A})\mathbb{1}_{2\times 2}\frac{-e\hbar}{4mc^2}\boldsymbol{\sigma}\times\boldsymbol{E}\right) && (3.5)\\ &= \frac{1}{2m}\left((\boldsymbol{p}-e\boldsymbol{A})\mathbb{1}_{2\times 2} - \frac{-e\hbar}{4mc^2}\boldsymbol{\sigma}\times\boldsymbol{E}\right)^2 - \frac{e^2\hbar^2}{32m^3c^4}\|\boldsymbol{\sigma}\times\boldsymbol{E}\|^2, && (3.6)\end{aligned}$$

where we assumed that the electric field has zero divergence.
Since the SO term under this re-structured form is included as part of the kinetic momentum, this suggest that it can be treated as a gauge field whose symmetry is the one of the SO Hamiltonian in the form of $SU(2)\times U(1)$. This gauge field is non-Abelian due to the $SU(2)$ sector, and will rise to an interesting interpretation, and somehow new manifestation of the SO interaction in this context. The field $W^{\mu a}$ is defined in such a way that,

$$H = \frac{1}{2m}\left(\boldsymbol{p}-e\boldsymbol{A}-g\boldsymbol{W}^a\tau^a\right)^2 - \frac{g^2}{8m}W_i^bW_i^b + gW_0^a\tau^a,$$

where $gW_0^a\tau^a = -(e/m)\boldsymbol{\sigma}\cdot\boldsymbol{B}$ is associated with the Zeeman interaction, W_i related with the

curl of $\boldsymbol{E}$ and the $\hbar\tau^a = s^a$. One can identify the third term in the square as a new $SU(2)$ connection defined by $gW_i^a\tau^a = -(e\hbar/2mc^2)\varepsilon_{iaj}E_j\tau^a$, or explicitly,

$$g\boldsymbol{W}^1 = \frac{e\hbar}{2mc^2}\left(E_z\boldsymbol{u}_y - E_y\boldsymbol{u}_z\right), \tag{3.7}$$

$$g\boldsymbol{W}^2 = \frac{e\hbar}{2mc^2}\left(-E_z\boldsymbol{u}_x + E_x\boldsymbol{u}_z\right), \tag{3.8}$$

$$g\boldsymbol{W}^3 = \frac{e\hbar}{2mc^2}\left(E_y\boldsymbol{u}_x - E_x\boldsymbol{u}_y\right), \tag{3.9}$$

where $\boldsymbol{u}_i$ are the unit vectors in the $x-$, $y-$ and $z-$ directions and the τ^a are the symmetry generators for $SU(2)$, obeying the commutation relation $[\tau^a, \tau^b] = i\varepsilon_{abc}\tau^c$, ε_{abc} being the totally antisymmetric tensor and $g = \hbar$. The relation between the spin operator and the corresponding generators is $\hbar\tau^a = s^a$ and the spin is $s = 1/2$. Following the an usual notation for a quadri-vector $\boldsymbol{W}^a = (W_0^a/c, W_i^a)$. The Latin indices from the middle of the alphabet, ijk, denote the spatial coordinates and run over three values, and the letters *a,b,c* denote the internal space indices for the generators. We will always use the internal space indices as superindices. The purpose of writing the second term here, as a function of the $SU(2)$ connection is to evidence *gauge symmetry breaking* (GSB) in this Hamiltonian. This observation has important consequences in the physical interpretation of the resulting Yang-Mills fields and is the reason why the Yang-Mills fields themselves are observable quantities, whereas in a gauge symmetric theory they would be gauge independent [39].

3.1.2 Noether Currents and Spin Current

In the following we will generate the Noether currents canonically. The appropriate Lagrangian for the corresponding equations of motion must be written. The non-relativistic Lagrangian density, omitting identity matrices, is given by,

$$
\begin{aligned}
\mathcal{L} &= \frac{i\hbar}{2}\left(\Psi^{\dagger}\dot{\Psi} - \dot{\Psi}^{\dagger}\Psi\right) \\
&- \Psi^{\dagger}\left(\frac{-g^2}{8m_0}W_i^b W_i^b + gW_0^a\tau^a + eA_0\right)\Psi \\
&- \frac{\hbar^2}{2m_0}\left[\mathcal{D}_j\Psi\right]^{\dagger}\mathcal{D}_j\Psi - \frac{e^2}{4m_0}F_{\mu\nu}F_{\mu\nu} - \frac{g^2}{4m_0}G^a_{\mu\nu}G^a_{\mu\nu},
\end{aligned}
$$

where Ψ is a Pauli spinor, $G^a_{\mu\nu} = \partial_\mu W^a_\nu - \partial_\nu W^a_\mu - \epsilon^{abc}W^b_\nu W^c_\mu$ and $F_{\mu\nu} = \partial_\mu A_\nu - \partial_\nu A_\mu$ are the $SU(2)$ and $U(1)$ field tensors respectively.
The new term $\frac{-g^2}{8m}W_i^b W_i^b$ arises when building the covariant derivatives $\mathcal{D}_i = \partial_i - \frac{ie}{\hbar}A_i - \frac{ig}{\hbar}W_i^a\tau^a$ that define the gauge potentials. It is clear that the Lagrangian density is not invariant under the transformations,

$$\Psi \to U\Psi, \tag{3.10}$$

$$W_\mu \to UW_\mu U^{-1} - \frac{i\hbar}{g}(\partial_\mu U)U^{-1}, \tag{3.11}$$

$$\tag{3.12}$$

as can be seen from the presence of the quadratic term in W_i^a in the gauge field term wich restricts the gauge invariance to a smaller set of transformations.

The equations of motion of the non- Abelian fields can be obtained from the Euler Lagrange equations, making the variations with respect to the gauge fields,

$$\partial_\mu \frac{\partial\mathcal{L}}{\partial(\partial_\mu W^a_\nu)} = \frac{\partial\mathcal{L}}{\partial W^a_\nu}, \tag{3.13}$$

the left hand side of this equation gives,

$$\partial_\mu \frac{\partial\mathcal{L}}{\partial(\partial_\mu W^a_\nu)} = -\partial_\mu G^{\mu\nu a}, \tag{3.14}$$

and it is straightforward to introduce a conserved current.

The spin current density $\boldsymbol{\mathcal{J}}^a$ is calculated from the r.h.s. of equation (3.13),

$$\frac{\partial \mathcal{L}}{\partial W^a_\mu} = \mathcal{J}^{a\mu}. \tag{3.15}$$

This conserved current is the full spin current, that is carried by both, matter and radiation i.e. $\boldsymbol{\mathcal{J}}^a = \boldsymbol{J}^a_M + \boldsymbol{J}^a_R$. The spatial (spin current) component of the current density then follow as,

$$\begin{aligned} \mathcal{J}^a_i &= \Psi^\dagger \left(\frac{g^2}{4m} W^a_i \right) \Psi + \frac{g^2}{m} \varepsilon^{abc} W^b_\nu G^c_{\nu i} \\ &- \frac{i\hbar g}{2m} \left[(\tau^a \Psi)^\dagger \mathcal{D}_i \Psi - (\mathcal{D}_i \Psi)^\dagger (\tau^a \Psi) \right], \end{aligned} \tag{3.16}$$

and the spin polarization, which is the time component is,

$$\mathcal{J}^a_0 = \Psi^\dagger g \tau^a \Psi + \frac{g^2}{m_0} \varepsilon^{abc} W^b_j G^c_{j0} \tag{3.17}$$

Three terms can be distinguished in the spatial spin current density:

- The first term has the canonical form for a material current, $\boldsymbol{\mathcal{J}}^a_{Matter} = g/2 \Psi^\dagger (\tau^a \boldsymbol{v} + \boldsymbol{v} \tau^a) \Psi$.
- The second term comes form the gauge symmetry breaking contribution, it is dependent on both, matter and radiation.
- The third term is the canonical radiative contribution originating from the derivative with respect to the gauge potential of the non-Abelian contribution of the field tensor $G^{\mu\nu a}$. A term that is only present in this approach, since in a $U(1)$ theory there is no charge carried by the propagated degrees of freedom.

The equilibrium currents, discussed in references [10, 11], arise in relation to the radiative contribution, cubic in the non-Abelian potential. We emphasize that, the extent to which gauge symmetry is broken depends on the choice of the electric field. If only the $E_z \neq 0$, then one allows gauge transformations that leave $W^2_1 = -W^1_2$ invariant. This is analogous to the remnant Z_2 group after $U(1)$ GSB in superconductors and a similar situation in the electroweak GSB mechanism[40]. The covariant derivative in terms of ordinary derivatives plus a

gauge dependent is,

$$-\frac{i\hbar g}{2m_0}\left[(\tau^a\Psi)^\dagger\,\partial_i\Psi-(\partial_i\Psi)^\dagger\,(\tau^a\Psi)\right]-\Psi^\dagger\left(\frac{g^2}{4m_0}W_i^a\right)\Psi, \tag{3.18}$$

where we will focus our attention to the extra spin dependent term. First, since the gauge theory here is non-Abelian, the corresponding current is not gauge invariant and thus a function that is not a candidate for an physical observable [13]. An important property in the SO case is that the gauge field is determined by the physical electric field, and thus the gauge is fixed and the spin current becomes properly defined. The third term in equation (3.16), which has the structure of a gauge symmetry breaking term, would also by itself fix the gauge and it has further consequences.

The second term in 3.18 is the non-Abelian analog of the London term in superconductivity. This term exactly cancels the symmetry breaking term in (3.16) and renders *zero* matter currents proportional to the electric field (zero spin conductivity). In contrast to the superconductivity case where the London term is the only one remaining after symmetry breaking, in the non-Abelian case, the London contribution gets canceled exactly. The equilibrium currents remain in relation to the leftover radiative contribution, cubic in the non-Abelian potential plus a field independent matter contribution.

The previous discussion can be clearly seen if we use the expansion of the covariant derivative (3.18) in equation (3.16).

$$\begin{aligned}\mathcal{J}_i^a &= \Psi^\dagger\left(\frac{g^2}{4m}W_i^a\right)\Psi+\frac{g^2}{m}\varepsilon^{abc}W_\nu^bG_{\nu i}^c-\\ &- \frac{i\hbar g}{2m_0}\left[(\tau^a\Psi)^\dagger\,\partial_i\Psi-(\partial_i\Psi)^\dagger\,(\tau^a\Psi)\right]-\Psi^\dagger\left(\frac{g^2}{4m_0}W_i^a\right)\Psi.\end{aligned} \tag{3.19}$$

The current is finally written as,

$$\mathcal{J}_i^a = \frac{g^2}{m}\epsilon^{abc}W_\nu^bG^{c\nu i}-\frac{i\hbar g}{2m}\left[(\tau^a\Psi)^\dagger\,\partial_i\Psi-(\partial_i\Psi)^\dagger\,(\tau^a\Psi)\right]. \tag{3.20}$$

The components of the non-Abelian gauge field are,

$$\frac{g}{m}W_i^a\tau^a=(\beta\tau^x-\alpha\tau^y)\boldsymbol{x}+(\alpha\tau^x-\beta\tau^y)\boldsymbol{y}. \tag{3.21}$$

Given this, the spatial current is explicitly written in terms of the Rashba and Dresselahus

coupling parameters,

$$\begin{aligned}
\mathcal{J}_i^a &= -\frac{m^2}{g}\left(2(\alpha^2+\beta^2) - \frac{g^3}{m^3}\left(\frac{e\hbar}{gm}\right)^2 B^2\right)\begin{pmatrix}\beta & -\alpha\\ \alpha & -\beta\end{pmatrix} \\
&+ \frac{m^2}{g}\beta(\alpha^2+\beta^2)\begin{pmatrix}1 & 0\\ 0 & -1\end{pmatrix} \\
&+ \frac{m^2}{g}\alpha\begin{pmatrix}2\alpha\beta & -(\alpha^2+\beta^2)\\ \alpha^2+\beta^2 & -\alpha\beta\end{pmatrix} \\
&- \frac{i\hbar g}{2m}\left[(\tau^a\Psi)^\dagger\,\partial_i\Psi - (\partial_i\Psi)^\dagger\,(\tau^a\Psi)\right]. \qquad (3.22)
\end{aligned}$$

Let us write it in the absence of magnetic field and in a pure Dresselhaus media so the α parameter and B are zero.

$$\mathcal{J}_{iD}^a = -\frac{m^2}{g}\beta^3\sigma_z - \frac{i\hbar g}{2m}\left[(\tau^a\Psi)^\dagger\,\partial_i\Psi - (\partial_i\Psi)^\dagger\,(\tau^a\Psi)\right].$$

Also in a pure Rashba media where the β parameter is zero. The resulting spatial current is

$$\mathcal{J}_{iR}^a = \frac{m^2}{g}\alpha^3\epsilon_i^a - \frac{i\hbar g}{2m}\left[(\tau^a\Psi)^\dagger\,\partial_i\Psi - (\partial_i\Psi)^\dagger\,(\tau^a\Psi)\right].$$

where ϵ_i^a is a 2D antisymmetric tensor.

The radiative contribution of the current in this case is of third order in α, a result obtained by Rashba [41] using the standard (not unique) definition of spin current.
As we see the variational definition of the currents in terms of Lagrangian derivatives is an unambiguous way to define a current, since its canonical form do not depends of an ad hoc proposition. The variational principle is not enough to solve the ambiguity of the spin current definition, to be consistent we need also a symmetry broken formulation (or gauge fixed), otherwise, gauge transformations would change the matter (spin) and radiation (torque) content i.e. the matter currents are gauge covariant. A similar gauge symmetry scenario to the one presented here is materialized in superfluid condensates of neutral Bosons in the Helium 3 B phase, where one encounters a $SU(2)$ Anderson-Higgs mechanism[33].

Vanishing of the spin Hall conductivity for Rashba materials in arbitrary dimension

As we have mentioned, the presence of the gauge symmetry breaking term in the Lagrangian density exactly compensates the "diamagnetic" (also called diacolor) term in the spin current density, and therefore there cannot be any spin current proportional to the electric field [11]. This means that the spin Hall conductivity identically vanishes, and this result is true in arbitrary dimensions. In the particular case of a two-dimensional system with Rashba SO interaction, Rashba has shown, using sum rule arguments, that there is no spin Hall conductivity [41]. Our conclusion is more general in the sense that in any dimension we obtain a spin Hall conductivity which vanishes due to an exact cancellation between two terms.

Chapter 4

Mach-Zehnder Interferometer - Spin Filtering

At this point, we have reviewed briefly the relevant aspects in the literature that covers the origins of the SO coupling to its formulation in semiconductors as a $SU(2)$ gauge theory. In order to construct a closed theory in which the non Abelian reformulation of the SOI could take place, we propose to use the reformulation in a $SU(2) \times U(1)$ gauge theory to show its kindness and reveal the gauge structure of the theory for the spin currents. All persistent currents and color diamagnetism [10] can be understood in a manner analogous to the well known $U(1)$ gauge theories.

A perfect spin filter based on active Rashba spin orbit media can be constructed is several setups [6], for example, ballistic spin interferometers [36], the analysis of the persistent spin helix [42, 43], where the Yang Mills gauge point of view can be advantageous.

We will consider an electronic Mach Zehnder interferometer (MZI) in the presence of a Rashba and Dresselhaus media. We obtain spin filtering by interferometry in a quasi two dimensional system, and connect to an experimentally feasible set of tests for this proposal. Within this setup we can obtain exact conditions for spin filtering by tuning appropriate experimental parameters as the SO intensity. Such conditions for spin filtering generalize previous special situations where the spin polarization is a conserved quantity [44].

4.1 Scattering in 2DEG with Spin Orbit Interaction

Let us consider a two dimensional system of non interacting electrons in which a media is present with both Rashba and Dresselhaus spin orbit interactions. One can apply an external transverse magnetic flux Φ_B described by a $U(1)$ gauge vector potential $\boldsymbol{A}$. It can be measured and controlled using gate voltages [45, 46].

The two dimensional Hamiltonian for a single particle in a GaAs/AlGaAs electron gas that includes the SO and a magnetic field is given by,

$$H = \frac{\boldsymbol{\Pi}^2}{2m^*} + V - \alpha(\Pi_x\sigma_y - \Pi_y\sigma_x) - \beta(\Pi_x\sigma_x - \Pi_y\sigma_y) + \frac{\hbar\omega_B}{2}\sigma_z. \tag{4.1}$$

Where $\boldsymbol{\Pi} = \boldsymbol{p} - e\boldsymbol{A}$, V is a substrate symmetric lattice potential that is assumed periodic, $\boldsymbol{\sigma}$ are the Pauli matrices, α and β are Rashba and Dresselhaus coupling strength parameters, characterized by the material with units of $[energy]/[momentum]$. The last term is the Zeeman energy. According to measured parameters in ref. [45] the SO energy for an GaAs/AlGaAs electron gas is 5 orders of magnitude greater than the Zeeman energy for the proposed field strengths, so we will neglect the Zeeman interaction as a generator of the precession in the wavefunctions but as a strong global phase contribution. Nevertheless, we will see that there are spin filtering scenarios for the device even for zero external magnetic field.

Following Chapter 3, we can introduce a spin dependent (non-Abelian) gauge field $\boldsymbol{W}$ whose components are given by,

$$\frac{g}{m^*}\boldsymbol{W} = (\beta\tau^x - \alpha\tau^y)\boldsymbol{x} + (\alpha\tau^x - \beta\tau^y)\boldsymbol{y}, \tag{4.2}$$

with $\tau_a = \sigma_a/2$ and $g = \hbar$ is the $SU(2)$ coupling constant.

We can rewrite the Hamiltonian in terms of the $SU(2)$ field,

$$H = \frac{(\boldsymbol{p} - e\boldsymbol{A} - g\boldsymbol{W}^a\tau_a)^2}{2m^*} + eA_0 - \frac{g^2\boldsymbol{W}^a\cdot\boldsymbol{W}^a}{8m^*}. \tag{4.3}$$

The first term describes the total kinetic energy including the contribution from the vector potential due to an external magnetic field and the $SU(2)$ gauge field. The second term is the background lattice potential whereas the third term represents a gauge symmetry breaking contribution similar to the field originally discussed in references [34, 11, 13] responsible for rendering the spin currents physical.

4.2 Electronic Mach-Zehnder spin interferometer

A Mach Zehnder Interferometer (MZI) allows us to address the problem of spin filtering in a gauge independent manner. The setup for an MZI is sketched in Fig. 4.1. We are interested in determining the resulting amplitude Ψ_{D_i} at detector D_i, with $i = 1, 2$ and to find the conditions for perfect spin filtering at either detector. There is an relevant issue that must be discussed regarding spin 1/2 filtering. Let us assume that a state at the input is a pure state spinor, of spin 1/2, then the electron is polarized on some indeterminate axis, in principle random, coming from the Fermi sea of the input conductor. If one could find this axis for every electron that comes from the input then one would have a perfect spin filter for each electron, however the resulting current is unpolarized. We thus define the spin filter as one acting on any entering (pure state) polarization and returning a polarized state along a definite axis. This approach will serve to build a polarized spin current.

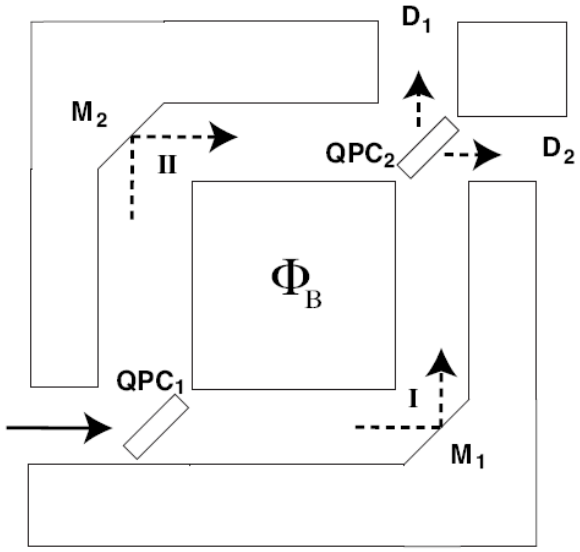

Figure 4.1: Sketch of the electronic Mach Zehnder interferometer setup. The arms of the square are made of active SO Rashba and Dresselhaus media. The beam splitters are implemented through two Quantum Point Contacts (QPCs). There is a magnetic flux Φ_B through the square.

Single electrons are extracted from the Fermi sea as pure states $\Psi_0 = \binom{\psi_0^+}{\psi_0^-}$ The electrons then go through a beam splitter that can be implemented by a combination of Quantum Point Contacts[47], we label the first as QPC_1 and can describe it by a 4×4 scattering matrix S_1 that

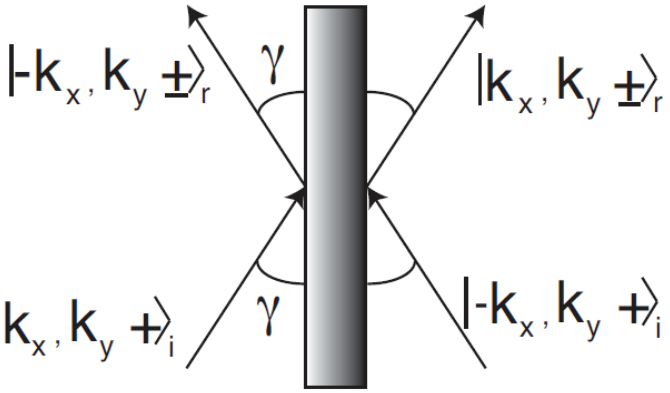

Figure 4.2: Detector D_2 output while D_1 filters out the up spin component (spin down polarization).

mixes spin orientations on perpendicular reflection but is diagonal for direct transmission[48]. The change in the direction of the electrons $\boldsymbol{k}$ vector within the SO active media mixes the spin orientations at all reflections, even at the mirrors reflections, this occurs because of the change in the orientation of the implied wavevectors-dependent magnetic field.

As we consider both Rashba and Dresselhaus interactions, we need to derive general reflection conditions at the beam splitters and mirrors. Yamamoto does this [48] for Rashba, assuming that small enough spin-orbit strength would yield only a small divergence of the reflected spin states in a $\boldsymbol{k}$ dependent basis. Surprisingly, when only the Rashba interaction is involved, the reflection matrix depends only on the incident angle and the reflection coefficient. On the other hand, if both Dresselhaus and Rashba are included, this is no longer true, and except for special angles of incidence, the reflection matrix depends on both Rashba and Dresselhaus strengths. We will take the limit of $\pi/4$ reflections, that leads to simple, spin-orbit independent matrix elements. The general reflection matrices can be derived from the Hamiltonian in equation (4.3). We can solve exactly for the eigenvalues and eigenfunctions, ignoring the Zeeman term and obtain

$$\varepsilon_{\pm} = \frac{\hbar^2 k^2}{2m^*} \pm \sqrt{k^2(\alpha^2 + \beta^2) + 4\alpha\beta k_x k_y}, \tag{4.4}$$

with eigenfunctions given by

$$|\mathbf{k}\ \pm\rangle_i = \frac{1}{\sqrt{2}} \begin{pmatrix} 1 \\ \mp F(k_x, k_y) \end{pmatrix} \quad , \quad F(k_x, k_y) = \frac{k_x(\beta - i\alpha) + k_y(\alpha - i\beta)}{\sqrt{k^2(\alpha^2 + \beta^2) + 4\alpha\beta k_x k_y}}, \tag{4.5}$$

where $\mathbf{k} = (k_x, k_y)$, $\pm$ stand for the two eigenvalues and the subindex i stands for incident wave. The convention we take, according to the figure, is that k_x and $\mathrm{k_y}$ are positive components for the incident electron. Referred to those components, one can obtain the reflected basis components by changing $k_x \to -k_x$ and $k_y \to k_y$ as the momentum in the y direction is conserved. To obtain the projections in terms of the reflected basis we write

$$|\mathbf{k}\ \pm\rangle_i = a_\pm |\mathbf{k}\ +\rangle_r + b_\pm |\mathbf{k}\ -\rangle_r, \tag{4.6}$$

where the subindex on the right indicates the reflected complete basis set. One can then compute the superposition coefficients $a_\pm$ and $b_\pm$ by performing the appropriate overlaps between incoming and outgoing wavefunctions

$$\begin{aligned} a_\pm &= {}_r\langle k + |k\pm\rangle_i = 1/2\left[1 \pm F^*(-k_x, k_y)F(k_x, k_y)\right], \\ b_\pm &= {}_r\langle k - |k\pm\rangle_i = 1/2\left[1 \mp F^*(-k_x, k_y)F(k_x, k_y)\right]. \end{aligned} \tag{4.7}$$

Each of the outgoing amplitudes gets multiplied by the scalar reflection coefficient r in the case of the beam splitter and $r = 1$ for perfect mirrors. The previous coefficients govern the QPC_1, the upper reflection of QPC_2 and M_1 in figure 5.1, while exchanges of $k_x \to -k_x$ would generate the corresponding matrix for the M_2 and the bottom reflection of QPC_2.
The wavector components can be expressed as $\mathbf{k} = (k\sin\gamma, k\cos\gamma)$ for a generic incident angle as seen in the figure. For the case of $\gamma = \pi/4$, the reflection matrices are particularly simple and one obtains equation (4.10), where the transmission matrix is trivially diagonal since the electron beam does not change direction.
A coordinate independent way to state the general result is by identifying $F(k_x, k_y) = \exp i\phi_i$ and $F(-k_x, k_y) = \exp i\phi_r$ then one can write the full reflection/transmission matrix as

$$\begin{pmatrix} r\cos[(\phi_r - \phi_i)/2] & ir\sin[(\phi_r - \phi_i)/2] & t & 0 \\ ir\sin[(\phi_r - \phi_i)/2] & r\cos[(\phi_r - \phi_i)/2] & 0 & t \\ t & 0 & r\cos[(\phi_r - \phi_i)/2] & -ir\sin[(\phi_r - \phi_i)/2] \\ 0 & t & -ir\sin[(\phi_r - \phi_i)/2] & r\cos[(\phi_r - \phi_i)/2] \end{pmatrix}. \tag{4.8}$$

The resulting beams follow path I (II) that consists of a first horizontal L_I (vertical L_{II}) arm made of Rashba-Dresselhaus medium whose length is L_I (L_{II}). The electrons are then specularly reflected from an ideal mirror M_1 (M_2), that also mixes spin directions, followed by a vertical L'_I (horizontal L'_{II}) arm of length L_I (L_{II}) of the same material. The mirrors can be implemented as a simplified version of the beam splitters of reference [47]. Then the electrons pass through a second QPC (QPC_2) described by the corresponding S-Matrix S_2. Finally, two electron beams are collected at detector D_i $(i = 1, 2)$, and we have $\Psi_{D_i} = \Psi_{I,i} + \Psi_{II,i}$, where, $\Psi_{I,i}$ $(\Psi_{II,i})$ is the corresponding transferred spinor through the i*th*-arm. These amplitudes can be written in terms of the injected spinor Ψ_0 as $\Psi_{D_i} = U_{D_i}\Psi_0$, where the 2×2 matrices U_{D_i} (generalized comparator operators [39]) are given by

$$\begin{aligned}
U_{D_1} = (t_2)\exp\Big[\frac{i}{\hbar}\int_{\mathcal{L'}_I} d\mathbf{l}\cdot(\mathbf{p}+e\mathbf{A}+g\boldsymbol{W}^a\tau^a)\Big](r_l)\exp\Big[\frac{i}{\hbar}\int_{\mathcal{L}_I} d\mathbf{l}\cdot(\mathbf{p}+e\mathbf{A}+g\boldsymbol{W}^a\tau^a)\Big](t_1) + \\
(r_{2l})\exp\Big[\frac{i}{\hbar}\int_{\mathcal{L'}_{II}} d\mathbf{l}\cdot(\mathbf{p}+e\mathbf{A}+g\boldsymbol{W}^a\tau^a)\Big](r_r)\exp\Big[\frac{i}{\hbar}\int_{\mathcal{L}_{II}} d\mathbf{l}\cdot(\mathbf{p}+e\mathbf{A}+g\boldsymbol{W}^a\tau^a)\Big](r_{1l}), \\
U_{D_2} = (r_{2r})\exp\Big[\frac{i}{\hbar}\int_{\mathcal{L'}_I} d\mathbf{l}\cdot(\mathbf{p}+e\mathbf{A}+g\boldsymbol{W}^a\tau^a)\Big](r_l)\exp\Big[\frac{i}{\hbar}\int_{\mathcal{L}_I} d\mathbf{l}\cdot(\mathbf{p}+e\mathbf{A}+g\boldsymbol{W}^a\tau^a)\Big](t_1) + \\
(t_2)\exp\Big[\frac{i}{\hbar}\int_{\mathcal{L'}_{II}} d\mathbf{l}\cdot(\mathbf{p}+e\mathbf{A}+g\boldsymbol{W}^a\tau^a)\Big](r_r)\exp\Big[\frac{i}{\hbar}\int_{\mathcal{L}_{II}} d\mathbf{l}\cdot(\mathbf{p}+e\mathbf{A}+g\boldsymbol{W}^a\tau^a)\Big](r_{1l}).
\end{aligned} \tag{4.9}$$

Such operators applied to the initial state do not change the energy expectation value. The transmission and reflection matrices regarding both Rashba and Dresselhaus interactions, for $\pi/4$ incidence angle, are given by

$$(t_j) = \begin{pmatrix} t_j & 0 \\ 0 & t_j \end{pmatrix} \;\; ; \;\; (r_{j[l,r]}) = \frac{\sqrt{2}}{2}\begin{pmatrix} r_j & \pm ir_j \\ \pm ir_j & r_j \end{pmatrix}, \tag{4.10}$$

where the subscripts j correspond to the beam splitter index (see figure 4.1) and r, l (corresponding to $+, -$ in the non diagonal matrix elements, respectively) encode whether the electron current is reflected counter-clockwise (l) or clockwise (r). r_j and t_j are the reflection and transmission coefficients for the $j-$th beam splitter, while for the mirrors, the reflection coefficients are equal to 1. Note that U_{D_i} is not a unitary operator. The normalization condition $|\Psi_{D_1}|^2+|\Psi_{D_2}|^2 = 1$ for the total probability at the detectors requires that $U^\dagger_{D_1}U_{D_1}+U^\dagger_{D_2}U_{D_2} = \mathbb{1}$, the unit matrix. This simply means that the amplitudes received at the detectors do not in-

terfere. The arms of the interferometer can be built from gate defined quasi one dimensional paths implemented on a 2DEG, where all transport is kept within one of the available transverse modes. The scattering length is assumed to be long enough, so that phase relations can be accurately described by the path lengths and the spin-orbit strengths as in the Datta Das [25] switch arrangement.

4.3 Spin diagonal mirrors and beam splitters

In this section we consider a simplified version of the filtering device where beam splitters and mirrors are considered diagonal matrices or scalars. Although this approximation does not contemplate the matrix nature of the reflections we will obtain a simple scenario for the filtering properties of the device. The full problem will be treated below where essentially the same qualitative results are obtained.

If the electric field $\mathbf{E}$ is uniform and static, the operators $\mathbf{p} - e\mathbf{A}$ and $g\boldsymbol{W}^a\tau^a$ commute. Thus, we can separate the *orbital* from the *internal* translation operators. For simplicity we will assume a square interferometer, thus $L_I = L_{II} = L$. Otherwise there are no restrictions or approximations related to the dimensions of the arms of the interferometer. As in Chen and Chang [43] we will make the discussion general by treating both the Rashba and Dresselhaus spin-orbit coupling on equal footing.

Concerning the *orbital* contribution, it is easy to see that this will consist of a global phase $\exp[\mathbf{p}\cdot(\mathbf{L_1}+\mathbf{L_2})]$ which we can drop, and a relative $U(1)$ phase φ_B which arises from the noncommutation of $\mathbf{p}$ and $\mathbf{A}$. Using the definition for the magnetic flux $\Phi_B = BL^2$ and that for the flux quantum $\phi_0 = h/e$, the nontrivial *orbital* phase is written as $2\pi\varphi_B = 2\pi\Phi_B/\phi_0$. On the other hand, the internal part gives rise to the $SU(2)$ spin-dependent phase contribution. In order to simplify the resulting expressions, we introduce the adimensional variable

$$\Lambda = (m^* L/\hbar)\sqrt{\alpha^2+\beta^2}, \tag{4.11}$$

that will be the crucial control parameter governing the SO interaction. Furthermore, we introduce the definitions $\theta \equiv \tan^{-1}(\beta/\alpha)$ along with the matrices $\tilde{\sigma}_1 \equiv \cos\theta\sigma^x - \sin\theta\sigma^y$ and $\tilde{\sigma}_2 \equiv \sin\theta\sigma_x - \cos\theta\sigma_y$, such that $(\tilde{\sigma}^i)^2 = \mathbb{1}$, with $\mathbb{1}$ the identity matrix in spin space. After the

previous considerations we can rewrite equation (4.9) in the form

$$\begin{aligned} U_{D_1} &= (t_2)\exp(-i\Lambda\tilde{\sigma}_1)(r_l)\exp(-i\Lambda\tilde{\sigma}_2)(t_1) + \\ &\quad \exp(2\pi i\varphi_B)(r_{2r})\exp(-i\Lambda\tilde{\sigma}_2)(r_r)\exp(-i\Lambda\tilde{\sigma}_1)(r_{1l}), \\ U_{D_2} &= (r_{2r})\exp(-i\Lambda\tilde{\sigma}_1)(r_l)\exp(-i\Lambda\tilde{\sigma}_2)(t_1) + \\ &\quad \exp(2i\pi\varphi_B)(t_2)\exp(-i\Lambda\tilde{\sigma}_2)(r_r)\exp(-i\Lambda\tilde{\sigma}_1)(r_{1l}). \end{aligned}$$

Due to the symmetry of these expressions (U_{D_2} is obtained from U_{D_1} by the substitutions $r_2 \leftrightarrow t_2$) we can focus on the first process, and obtain the second by making the necessary substitutions. Using the identity $\exp(\pm i\gamma\sigma_n) = \cos\gamma\mathbb{1} \pm i\sigma_n \sin\gamma$, valid also for our redefined $\tilde{\sigma}$, the matrix U_{D_1} takes the form

$$\begin{aligned} U_{D_1} &= t_1t_2[\cos^2\Lambda\mathbb{1} - i\sin\Lambda\cos\Lambda(\tilde{\sigma}_1+\tilde{\sigma}_2) - \tilde{\sigma}_1\tilde{\sigma}_2\sin^2\Lambda] + \\ &\quad r_1r_2e^{2i\pi\varphi_B}[\cos^2\Lambda\mathbb{1} - i\sin\Lambda\cos\Lambda(\tilde{\sigma}_1+\tilde{\sigma}_2) - \tilde{\sigma}_2\tilde{\sigma}_1\sin^2\Lambda]. \end{aligned}$$

Now, we can easily determine that $\tilde{\sigma}_1\tilde{\sigma}_2 = \sin 2\theta\mathbb{1} - i\sigma_z\cos 2\theta$ thus $\tilde{\sigma}_2\tilde{\sigma}_1 = \sin 2\theta\mathbb{1} + i\sigma_z\cos 2\theta$ and $\tilde{\sigma}_1 + \tilde{\sigma}_2 = (\cos\theta + \sin\theta)(\sigma_x - \sigma_y)$. Substituting these results and rearranging the obtained expressions leads to

$$U_{D_1} = \mathcal{A}_+[\cos^2\Lambda - \sin^2\Lambda\sin 2\theta]\mathbb{1} + i\sin\Lambda\,\mathbb{M},$$

where we have introduced the traceless matrix $\mathbb{M} = \mathcal{A}_-\sin\Lambda\cos 2\theta\sigma_z - \mathcal{A}_+\cos\Lambda(\cos\theta + \sin\theta)(\sigma_x - \sigma_y)$ and $\mathcal{A}_\pm = t_1t_2 \pm r_1r_2e^{2i\pi\varphi_B}$. The traceless condition simplifies the diagonalization of $\mathbb{M}$, and the eigenvalues for U_{D_1} are easily found to be

$$\lambda_\pm^{D_1} = \mathcal{A}_+[\cos^2\Lambda - \sin^2\Lambda\sin 2\theta] \mp i\sin\Lambda\sqrt{\mathcal{A}_-^2\sin^2\Lambda\cos^2 2\theta + 2\mathcal{A}_+^2\cos^2\Lambda(1+\sin 2\theta)}. \tag{4.12}$$

If we now define $\mathcal{B}_\pm = t_1r_2 \pm r_1t_2e^{2i\pi\varphi_B}$, the eigenvalues of the matrix U_{D_2} are obtained from the previous result by making the substitution $\mathcal{A}_\pm \to \mathcal{B}_\pm$

$$\lambda_\pm^{D_2} = \mathcal{B}_+[\cos^2\Lambda - \sin^2\Lambda\sin 2\theta] \mp i\sin\Lambda\sqrt{\mathcal{B}_-^2\sin^2\Lambda\cos^2 2\theta + 2\mathcal{B}_+^2\cos^2\Lambda(1+\sin 2\theta)}. \tag{4.13}$$

In order to get more insight into the nature of the conditions for perfect spin filtering we will

specialize the previous expression to symmetric beam splitters i.e. $r_1 = r_2 = r$, and $t_1 = t_2 = t$. Within this case, we have $\mathcal{A}_\pm = t^2 \pm r^2 e^{2i\pi\varphi_B}$. Since we are interested in filtering one spin component, say the up component, we now proceed to determine the vanishing conditions of the corresponding eigenvalue $\lambda_+^{D_1}$.

From expressions (4.12, 4.13), these vanishing conditions can be found by either having $\cos\Lambda = 0$ or $\cos\Lambda \neq 0$ (see also equation (4.11)). Although the former condition is mathematically only a particular case of the general solution, we distinguish it because the corresponding U_{D_1} becomes diagonal with respect to the original quantization axis, so we can speak of filtering along a *non-tilted* axis. Such a solution is also the simplest from the detection point of view since it involves the choice of a single quantization axis for the whole setup. The second condition ($\cos\Lambda \neq 0$) corresponds to finding a new axis where the up spin is filtered and we call such axis the *tilted* quantization axis. Note that both these filtering conditions (non-tilted and tilted) are *independent of the polarization axis and the energy of the incoming state*. We will comment further on this below.

4.3.1 Non-tilted filtering

Let us first analyze the *non-tilted* situation. In this case the filtering condition requiring $\lambda_+^{D_1} = 0$ for all incoming energies (see equation (4.12)), leads to the relation

$$\tan 2\theta = -\frac{i(t^2 - r^2 e^{2i\pi\varphi_B})}{(t^2 + r^2 e^{2i\pi\varphi_B})}.$$

Two $50\% - 50\%$ beam splitters for which $r = i/\sqrt{2}$, $t = 1/\sqrt{2}$, will then lead to the relation $\sin\pi\varphi_B \sin 2\theta = \cos\pi\varphi_B \cos 2\theta$, equivalent to the simple expression $\cos(\pi\varphi_B + 2\theta) = 0$, satisfied by the condition

$$\pi\varphi_B + 2\theta = (2n+1)\frac{\pi}{2}, \tag{4.14}$$

where n is an integer. Figure 4.3 depicts the relation between the spin-orbit parameters and the magnetic flux, for $n = 0$, necessary for perfect filtering of the up component in the original quantization axis. The spin-orbit parameters are in a reasonable range, as depicted in the figure, since for a GaAs heterostructure $\hbar\alpha \sim 3.9 \times 10^{-12}$eVm[25], $\hbar\beta \sim 2.4 \times 10^{-12}$eVm and $\hbar^2/m^*L \sim 1.7 \times 10^{-12}$eVm, assuming the arm of the interferometer $\sim 1\mu m$ and an effective mass of $m^* = 0.046 m_0$. These parameters yield $|\alpha|, |\beta| < 6$ in units of $\hbar/(m^*L)$. Note that our definition of α, β differs by a factor $\hbar$ to the standard definition (see equation (4.1)). In

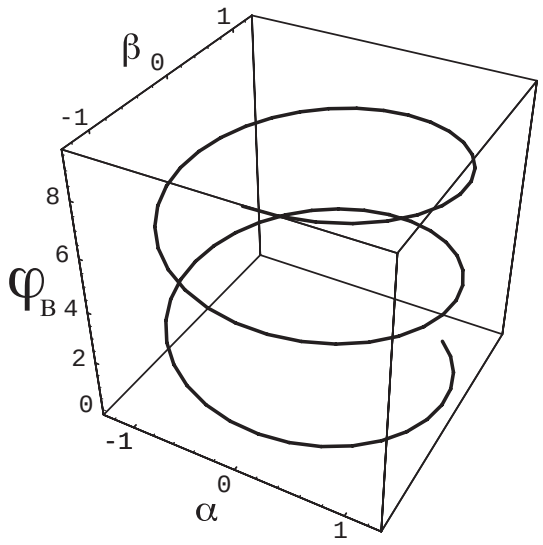

Figure 4.3: Perfect filtering for the non-tilted axis (original incoming basis). The plot shows the relation between α, β in units of $\hbar/(m^*L)$, and φ_B that yields perfect polarization of the spin from an unpolarized input. The figure corresponds the values $n, l = 0$ according to equation (4.15).

reference[45] it is shown that gate control can vary α and β parameters by a factor of 6 by applying gate voltages in the hundreds of mV.

The solutions are on a helix, as can be shown from the previous relations where

$$\begin{aligned} \alpha &= \frac{\hbar}{m^*L}\sqrt{(2l+1)\pi/2}\cos[\pi/4(2n+1-2\varphi_B)], \\ \beta &= \frac{\hbar}{m^*L}\sqrt{(2l+1)\pi/2}\sin[\pi/4(2n+1-2\varphi_B)]. \end{aligned} \tag{4.15}$$

The integer n was defined in equation (4.14) while the second integer l is defined by the condition $\cos\Lambda = 0$.

The previous conditions, depicted in figure 4.3, do not tell us about the intensity of the signal received in detector D_1 i.e. the efficiency of the filter given an incident intensity. For this, one has to look back at the eigenvalues. While $\lambda_+^{D_1} = 0$ the amplitude of the outgoing polarized spinor at detector D_1 is given by

$$\Psi_{D_1} = \begin{pmatrix} 0 \\ \lambda_-^{D_1}\psi_0^- \end{pmatrix} = \begin{pmatrix} 0 \\ ie^{i\pi\varphi_B}\cos(\pi\varphi_B - 2\theta)\psi_0^- \end{pmatrix}, \tag{4.16}$$

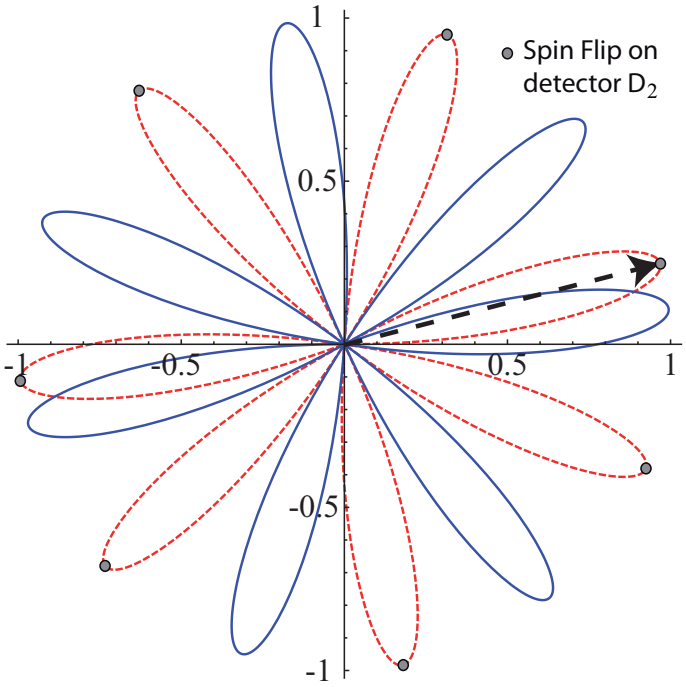

Figure 4.4: Filtering probability for the non-tilted solution of detector D_1 for $n = 0$, $l = 0$ solid (blue) curve and $n = 1$, $l = 0$ dashed (red) line. The radius vector depicted shows the filtered probability for the output spinor for one whole period in the parameters α, β as given in the figure 4.3. The position of the dashed vector corresponds to $\varphi_B = 0.25$. The grey points represent "spin flipping" or opposite filtering solutions for detector D_2.

whose modulus squared is $\cos^2(\pi\varphi_B - 2\theta)|\psi_0^-|^2$. Figure 4.4 shows a polar plot for the amplitude of the filtered signal (radius vector) as a function of the parameter designating the field flux φ_B and the α, β combination given by equation (4.15) for $n = 0, 1$ and $l = 0$. The figure shows that while filtering occurs for all the fluxes (given the appropriate values of α, β) the amplitude can be zero, or very small, for some flux values i.e. in this case, the detector D_2 gets most of the total amplitude. On the other hand, for some values of the flux, filtering can be very strong since the probability for a polarized spin can approach unity. The behavior of the second detector D_2, while the first detector sees a filtered signal, can be obtained through the eigenvalues of that detector having substituted the condition $\lambda_+^{D_1} = 0$, namely

$$\begin{aligned} \lambda_+^{D_2} &= -ie^{i\pi\varphi_B}, \\ \lambda_-^{D_2} &= ie^{i\pi\varphi_B}\sin(\pi\varphi_B - 2\theta). \end{aligned} \tag{4.17}$$

It is obvious that the second detector D_2 does not filter concomitantly with the D_1 in general. Furthermore, one can only find conditions for the second component to be zero (opposite filtering to detector D_1) since the first component has modulus one. This takes us to the non-tilting *spin flipped* or opposite filtering solution at detector D_2, only occurring while detector D_1 is filtering with maximal efficiency i.e. maximal polar radii in figure 4.4.
The filtering amplitude is proportional to the projection of the incoming spinor (which has arbitrary weights onto the chosen quantization axis) to the surviving component at the output (see equation (4.16)). This means that for each arbitrary incident spinor from the Fermi sea one gets a filtering probability that depends on this projection. The resulting polarized current will thus have a random noise associated with this effect besides the contribution from shot noise.
It is important to note that this solution does not appear in Abelian approximation (only exact in the case $\alpha^2 = \beta^2$ and in one dimension) to the translation operator, where the $SU(2)$ gauge vector operator has the same algebra as the $U(1)$ gauge vector. The previous approximation was implemented in reference [43] by neglecting the commutator between components of the $SU(2)$ gauge vector within a finite difference scheme. In this sense, the non-tilted case is an intrinsically non-Abelian scenario for spin filtering.

4.3.2 Tilted filtering axis

The tilted axis filtering scenario was discussed within the tight-binding model by Hatano, Shirasaki and Nakamura[49] when the Rashba coupling is present. In their approach, the interferometer involves an incoming lead and one outgoing lead, in contrast to our Mach-Zehnder configuration. The non-Abelian treatment is exact within their model, and requires a tilted outgoing axis to realize perfect spin filtering.
For the Mach-Zehnder configuration, addressed here, the *tilted* axis solution (i.e. $\cos\Lambda \neq 0$), requires $\lambda_+^{D_1} = 0$, which implies

$$\mathcal{A}_+[\cos^2\Lambda - \sin^2\Lambda \sin 2\theta] = i \sin\Lambda \sqrt{\mathcal{A}_-^2 \sin^2\Lambda \cos^2 2\theta + 2\mathcal{A}_+^2 \cos^2\Lambda(1+\sin 2\theta)}.$$

Squaring both sides and after some algebra one finds

$$\mathcal{A}_+^2 = \sin^4\Lambda \cos^2 2\theta (\mathcal{A}_+^2 - \mathcal{A}_-^2). \tag{4.18}$$

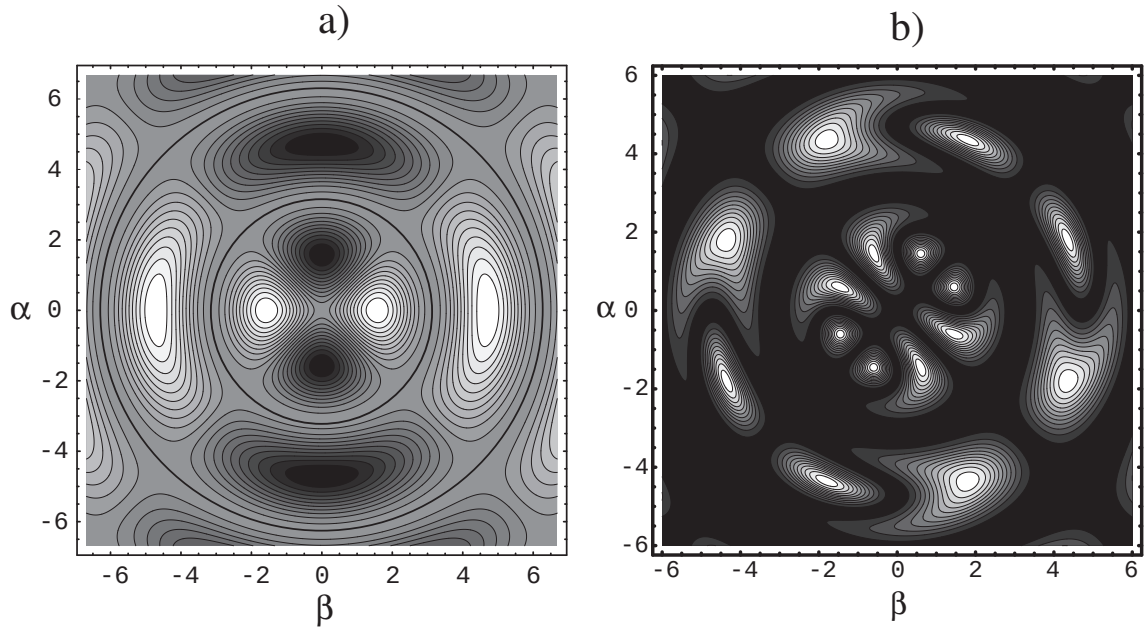

Figure 4.5: a) Perfect filtering by interference for the tilted axis. The contourplot shows the relation between α, β in units of $\hbar/(m^*L)$, and $\sin \pi\varphi_B$ given in equation 4.19, the darker regions indicate larger values for the magnetic flux needed to yield perfect filtering, from an unpolarized input. Highlighted circles depict the zero flux solutions that yield perfect filtering. b) Perfect filtering probability for the tilted axis. The plot shows the relation between α, β in units of $\hbar/(m^*L)$, and the filtered intensity in a contourplot. The lighter regions indicate larger values for the intensity of filtering for the relation between parameters depicted in figure 4.5a. Note that the circles evident from figure 4.5a correspond to zero output amplitude.

Using the definitions for $\mathcal{A}_\pm$, and taking the square root, we reduce equation (4.18) to

$$t^2 + r^2 e^{2i\pi\varphi_B} = 2rte^{i\pi\varphi_B} \sin^2 \Lambda \cos 2\theta.$$

Employing the $50\% - 50\%$ mirror condition, we get after substitution

$$\sin \pi\varphi_B = \sin^2 \Lambda \cos 2\theta. \tag{4.19}$$

This is the relation between the spin-orbit parameters and the magnetic flux that leads to perfect filtering in the tilted axis. The solution is depicted in a contourplot in figure 4.5a where the value of $\sin \pi\varphi_B$ is represented in shades of gray as a function of α and β. Each contour

corresponds to a constant magnetic flux value and runs over the perfect filtering values of α and β. The circular contour, depicted in the figure, corresponds to a $\varphi_B = 0$ solution to equation (4.19) that leads to $(m^*L/\hbar)\sqrt{\alpha^2+\beta^2} = p\pi$, for p integer. The figure depicts the solution for $p = 1, 2$, i.e. circles in units of $\hbar/(m^*L)$.
In order to see if the filter is actually working, we must address the filtered amplitudes by looking to the second eigenvalue at detector D_1. For the filtering condition

$$\lambda_-^{D_1} = -2ie^{i\pi\varphi_B} \sin\pi\varphi_B \left[\cos^2\Lambda - \sin^2\Lambda \sin 2\theta\right]. \tag{4.20}$$

Substituting equation (4.19) in this expression and computing the modulus squared of the eigenvalue, we determine the strength of the filtered output, as was done in equation (4.16). We have depicted the analytical solution for a range of values of α, β in the contour plot of figure 4.5b. The darkest shade corresponds to zero amplitude, and as the shade lightens the probability is higher for the filtered output. We note that the filtering solutions for the circular contours in figure 4.5a and the lines $\alpha = \pm\beta$ have zero amplitude. Such zero amplitude solutions correspond to those of "localized solutions" of Cheng and Chang [43] where there is no filtered output. Behavior of detector D_2, while D_1 is filtering out the spin up component (spin down polarization), is shown in figure 4.6. Regions with plus (minus) signs depict up (down) spin phases for detector D_2. Note that the two regions are mutually exclusive so that while pure spin down is being detected in D_1 one can have either spin up or spin down in D_2 depending on the range of α, β. The white regions correspond to no output at D_2. Comparing with figure 4.5b we see that no-output region are not identical for both detectors, these being larger for D_1, i.e. one can have zero output at D_1 while having non-zero output at D_2. As discussed before, the outputs depicted in figure 4.6 are also modulated by the magnitude of the corresponding component at the input, so the probability of the output exhibits noise coming from the random input spin orientation.

4.4 Non diagonal mirror and beam splitter reflections

Including the non diagonal matrix character of reflections at mirrors and beam splitters shifts the operation parameters of the spin filter but yields essentially the same qualitative results. The conditions must now be derived numerically. We start from equation (4.9) with the transmission and reflection matrices in equation (4.10). For the particular choice of $\pi/4$ incidence

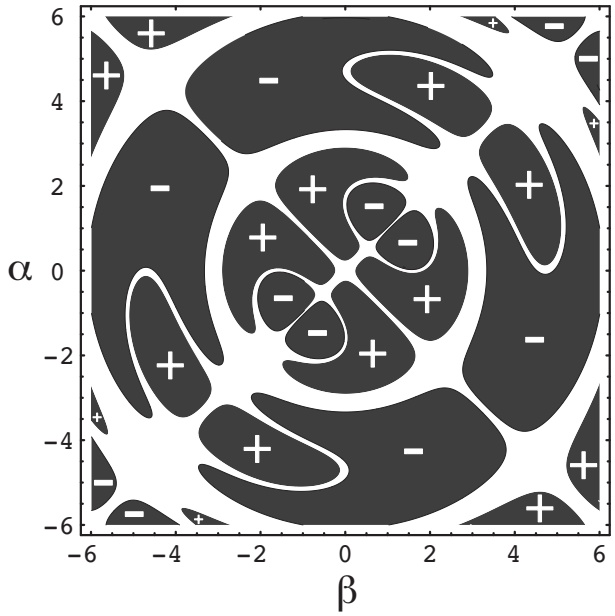

Figure 4.6: Detector D_2 output while D_1 filters out the up spin component (spin down polarization). The plus (minus) zones represent the regions where only the up spin (down) survives at the D_2 detector. Note that either one or the other is filtered. The white regions represent no output in the detector and correspond to the localized phase. On can have either up or down spin filtering in D_2 while up spin is filtered out in D_1.

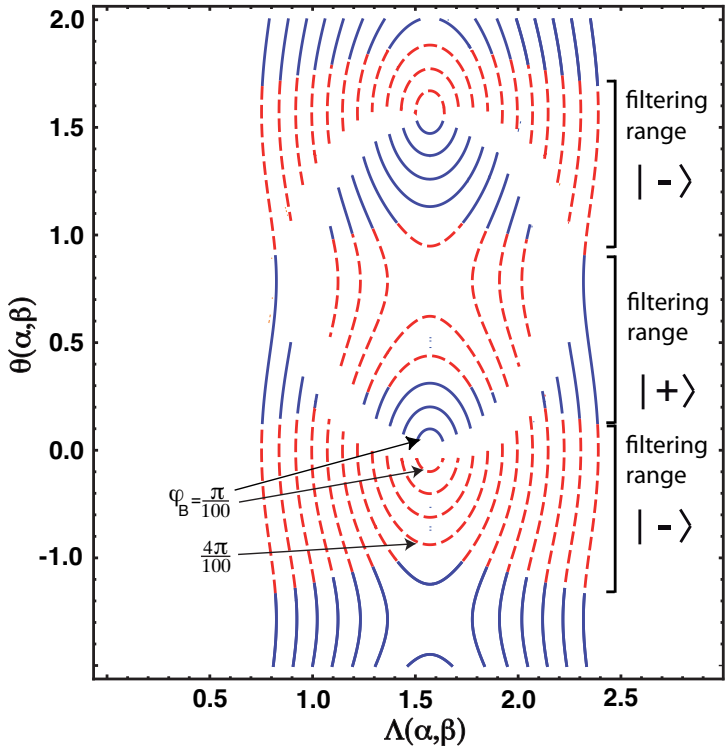

Figure 4.7: The zeroes of the first (dashed line or red online) and second (solid line, blue online) eigenvalues of U_{D_2}. When the first eigenvalue vanishes (and the second is non-zero), for specific combinations of α, β and φ_B the interferometer produces a perfectly polarized output in the $|-\rangle$ state. Only a particular discrete set of solutions for φ_B is depicted.

on the mirrors, the simple non-tilting scenario described above is not possible. The extra parameter given by the angle of incidence on the mirrors/beam splitters lends itself to making this regime accessible, but we will not pursue it here. The more general scenario of a tilted axis yields a whole range of possible filtering solutions.

Diagonalizing U_{D_2} in equation (4.9) we find two eigenvalues. Setting the first eigenvalue to zero implies that in this rotated space the spinor is fully polarized (one of the entries of the output spinor is zero) as described in equation (4.16). Setting this eigenvalue to zero means setting its real and imaginary parts to zero. Such zeroes are depicted in figure 4.7 by the dashed lines (red online) for different values of the magnetic field and specific combinations $\Lambda(\alpha, \beta)$, defined in equation (4.11), and $\theta = \tan^{-1}(\beta/\alpha)$. In order for filtering to be performed such zeroes must be accompanied by non-zero values of the second eigenvalue in the same detector. The zeroes of the second eigenvalue are depicted in figure 4.7 by the solid lines (blue online) which are non-overlapping with the dashed lines for the first eigenvalue. Thus the figure shows alternative filtering conditions for either spin up or spin down in the tilted basis.

The circular empty region in the middle of the plot corresponds to non-polarized output in the tilted axis. Such a region contains some pointlike solutions that are of less interest experimentally since they would be difficult to tune. We recall that the previous discussion in section 4.3.2 is equally valid in this case, all incoming electrons at the input are polarized at the output no matter their energy as long as particular parameters ranges in the α, β, Φ_B space are met.

In order to see the magnitude of the spin polarization for a particular value of the external magnetic field we draw a contour map of the magnitude of the second eigenvalue while the first one is zero. The background value at the dashed curves in figure 4.8, show the intensity of the pure down spin polarization at detector D_2 when at $\varphi_B = 5\pi/100$. The highest values of output achieved corresponds to the lighter shades on the contourmap.

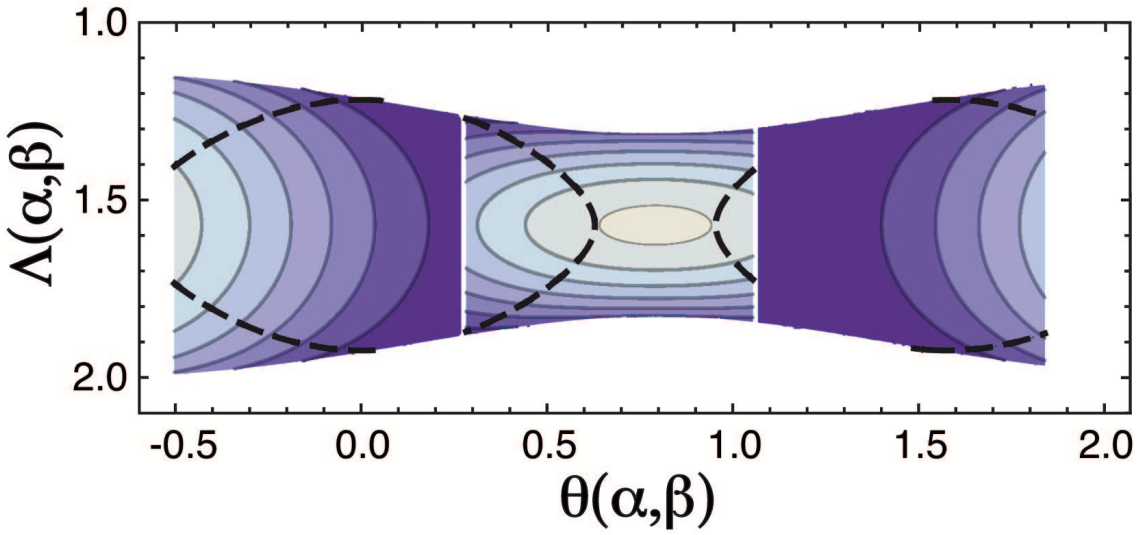

Figure 4.8: The dashed curves represent zeroes of the first eigenvalue for $\varphi_B = 5\pi/100$ upon a contourplot for the modulus of the second eigenvalue. The lighter shades represent higher values of the output polarization. One can extract the SO strengths from the plot by solving a simple system of equations for each value read off on the dashed curves.

Chapter 5

Mesoscopic Ring Coupled to a Reservoir - Spin Effects

It is of special interest that SO may be used to implement control of the spin degree of freedom, since it weakly couple to decoherence effects compared to the electric charge, moreover the topological effects, such as Aharonov-Bohm, Aharanov-Casher [23, 50] and Hall effects works as a protection mechanism for charge and spin currents, reducing the electronic dispersion and even emulating superconductivity. In chapter we determine the persistent spin and charge currents in semiconducting materials in a non-simply-connected geometry. In particular, a mesoscopic ring is considered made of an active two dimensional electron gas (2DEG) with RSO interaction and a crossing magnetic field in an Aharonov-Bohm configuration. Decoherence is introduced in the ring by coupling it with a electron reservoir that depends on the polarized spin states at zero and finite temperatures.

5.1 The decoupled SO active ring

We consider a 2DEG in the shape of a ring in polar coordinates. The expression for the Rashba Spin Orbit (RSO) potential in cartesian coordinates is,

$$\tilde{V}_R = \alpha(\sigma_x \Pi_y - \sigma_y \Pi_x), \tag{5.1}$$

where α is the coupling strength, tunable by an external electric field, σ_i denotes the Pauli matrices and $\Pi_i = p_i - eA_i$ where A_i are the components of the vector potential associated with an external magnetic field in the $\hat{z}$ direction. The potential is evidently Hermitian.
A straight-forward coordinate change $(x, y) \to (\rho, \phi)$ results in a non-hermitian form that must be symmetrized appropriately. The correct hermitian RSO potential in polar coordinates is given by the usual coordinate transformation plus a basis rotation of the spinor [51],

$$V_R = e^{i\sigma_z \frac{\varphi}{2}} \tilde{V}_R e^{-i\sigma_z \frac{\varphi}{2}} = -\hbar\omega_{SO}\sigma_\rho \left(i\partial_\varphi + \frac{\Phi}{\Phi_0} \right) - i\hbar\frac{\omega_{SO}}{2}\sigma_\varphi, \tag{5.2}$$

where $\omega_{SO} = \frac{\alpha\hbar}{a}$, a is the ring radius and $\Phi_0 = 2\pi\hbar/e$ is the quantum of flux. The rotated Pauli matrices are defined as $\sigma_\varphi = -\sigma_x \sin\varphi + \sigma_y \cos\varphi$ and $\sigma_\rho = \sigma_x \cos\varphi + \sigma_y \sin\varphi$. Adding the kinetic energy operator reads the Hamiltonian

$$H = \hbar\Omega \left(i\frac{\partial}{\partial\varphi} + \frac{\Phi}{\Phi_0} \right)^2 - \hbar\omega_{SO}\sigma_\rho \left(i\frac{\partial}{\partial\varphi} + \frac{\Phi}{\Phi_0} \right) - i\frac{\hbar\omega_{SO}}{2}\sigma_\varphi, \tag{5.3}$$

with $\Omega = \hbar/2ma^2$. Carefully completing squares taking into account operator ordering and the angular dependencies of σ_φ and σ_ρ, one arrives at the compact form,

$$H = \hbar\Omega \left(-i\frac{\partial}{\partial\varphi} - \frac{\Phi}{\Phi_0} + \frac{\omega_{SO}}{2\Omega}\sigma_\rho \right)^2 - \frac{\hbar\omega_{SO}^2}{4\Omega}. \tag{5.4}$$

In order to obtain the eigenvalues we can focus only on the quadratic term, and restore the additive scalar term to the resulting eigenvalue. We can then solve the simpler eigenvalue equation

$$\left(-i\frac{\partial}{\partial\varphi} - \frac{\Phi}{\Phi_0} + \frac{\omega_{SO}}{2\Omega}\sigma_\rho \right) \psi = \sqrt{\frac{E}{\hbar\Omega}}\psi, \tag{5.5}$$

clearly ψ, a spinor, is also eigenfunction of the square of the previous operator with the square of the eigenvalue. The proposed form for the eigenspinor is

$$\psi_j^\mu(\varphi) = e^{in_j^\mu\varphi}\chi^\mu(\varphi) = e^{in_j^\mu\varphi} \begin{pmatrix} A^\mu \\ e^{i\varphi}B^\mu \end{pmatrix} \tag{5.6}$$

where j labels right and left propagating plane waves ($j = 1$ clockwise and $j = 2$ counterclockwise), μ is the spin label and $n_j^\mu \in \mathbb{Z}$ ($\mu = 1$ spin up and $\mu = 2$ spin down). Solving the matrix

equation, the eigenvalues are found to be,

$$E^{\mu}_{n,j} = \hbar\Omega\left((-1)^j n + \frac{1}{2\pi}\Phi_{AB} - \frac{1}{2\pi}\Phi^{(\mu)}_{AC}\right)^2 - \frac{\hbar\omega^2_{SO}}{4\Omega} \tag{5.7}$$

were $\Phi_{AB} = \Phi/\Phi_0$ (AB for Aharonov-Bohm phase) and $\Phi_{AC} = \pi(1 + (-1)^{\mu}\sqrt{1 + (\omega_{SO}/\Omega)^2})$ (AC for Aharonov-Casher phase). The eigenfunction coefficients satisfy the relation

$$\frac{\Omega}{\omega_{SO}}\left(1 + (-1)^{\mu}\frac{1}{\cos\theta}\right)A^{\mu} = B^{\mu}, \tag{5.8}$$

with $\cos\theta = 1/\sqrt{1 + (\omega_{SO}/\Omega)^2}$. One can then choose $A^{(1)} = B^{(2)} = \cos\frac{\theta}{2}$ and $-A^{(2)} = B^{(1)} = \sin\frac{\theta}{2}$. We thus arrive at the eigenfunctions The magnetic flux breaks the the Time Reversal Symmetry (TRS) associated with the simultaneous change of j and μ.

$$\begin{aligned}
\psi^1_j(\varphi) &= e^{in^1_j\varphi}\begin{pmatrix}\cos\frac{\theta}{2}\\ e^{i\varphi}\sin\frac{\theta}{2}\end{pmatrix},\\
\psi^2_j(\varphi) &= e^{in^2_j\varphi}\begin{pmatrix}\sin\frac{\theta}{2}\\ -e^{i\varphi}\cos\frac{\theta}{2}\end{pmatrix},
\end{aligned} \tag{5.9}$$

where $\frac{\theta}{2} = \tan^{-1}(\Omega/\omega_{SO} - \sqrt{(\Omega/\omega_{SO})^2 + 1)})$. Figure 5.1 shows the spectrum for $\omega_{SO} = 0.75\Omega$. The spin-orbit interaction alone preserves time reversal symmetry, so in the absence of a magnetic field $E^{\uparrow}_{n,+} = E^{\downarrow}_{n,-}$ i.e. two fold degeneracies. At half integer flux quanta this degeneracy is repeated. For other values of the flux the degeneracy is broken. For zero SO coupling and in the absence of a Zeeman term there is a peculiar two fold degeneracy for each level due to the closing of the wave function for half integer spin. Thus $E^{\uparrow}_{n,-} = E^{\downarrow}_{n+1,-}$ and $E^{\downarrow}_{n,+} = E^{\uparrow}_{n+1,+}$ for all fluxes. At zero and half integer flux quanta we have four-fold degeneracy in the absence of SO coupling. Such degeneracies are important when computing the corresponding charge and spin currents.

Wavefunctions in (5.9), form a complete four function basis to represent couplings of the system with an external voltage probe.

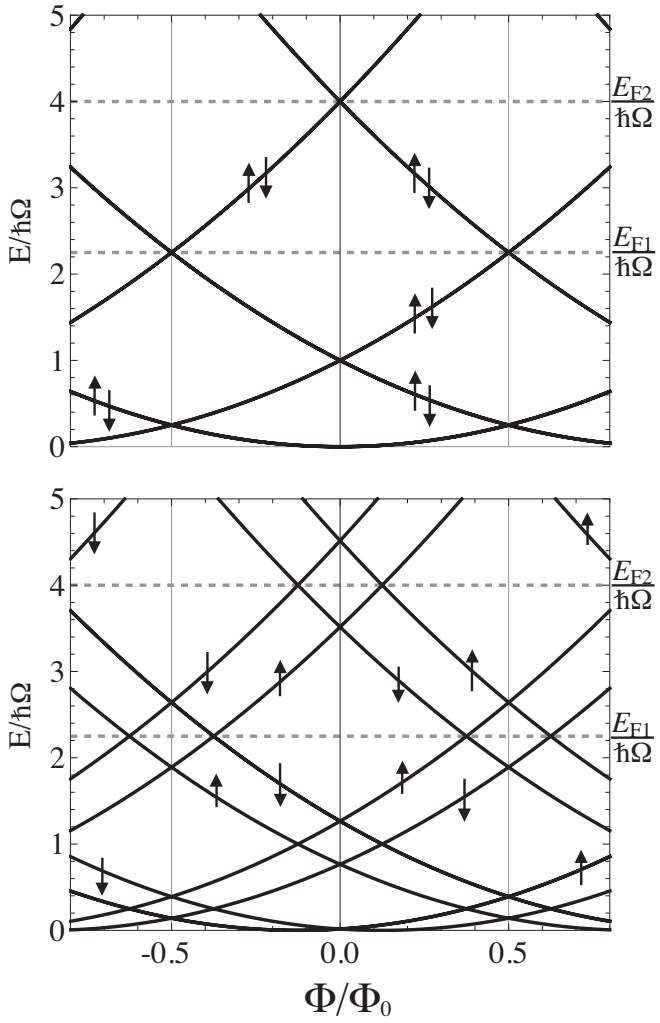

Figure 5.1: Energy states of the decoupled ring. ($\omega_{SO}/\Omega = 0.75$). The energy is expressed in units $E_0 = \hbar\Omega$. The two dashed lines represent fermi levels considered to compute the charge and spin currents below.

5.2 Decoherence with Spin Orbit coupling

In reference [9] Buttiker introduced an ingenious way to couple a simple quantum system (a ring) to reservoir that behaved like a voltage probe (zero current condition to reservoir). The approach here is similar; as the coupling to the reservoir is not defined in Hamiltonian terms and leads to dephasing, we have a Hamiltonian solution to the uncoupled problem and a scattering approach for the coupling to the reservoir. The two problems meet when using the complete basis of the uncoupled problem with the coefficients of these basis components determined by matching boundary conditions.

Coupling to the reservoir is introduced in a ring through an ideal lead that acts as a voltage probe (no net current threads the lead). The reservoir emits electrons with a Fermi distribution and absorbs electrons of any energy. Dephasing occurs due to the absence of a phase relation between injected and emitted electrons at a particular energy.

The coupling between the lead and the ring is described by the dispersion matrix S which relates the incoming and outgoing amplitudes $\vec{\alpha}' = S\vec{\alpha}$. The current conservation implies that S is unitary, the matrix is 3×3 one for each spin label μ, as the coupling to the reservoir is spin symmetric. Each entry corresponds to transmission (t) and reflections (r) from the lead to the ring, and from the ring to the lead. In general the matrix S will dependent on five independent parameters, considering S to be symmetric with respect to the two branches of the ring, the number of independent parameters reduces to three.

$$S = \begin{pmatrix} r_{33} & t_{32} & t_{31} \\ t_{23} & r_{22} & t_{21} \\ t_{13} & t_{12} & r_{11} \end{pmatrix} = \begin{pmatrix} -(a+b) & \sqrt{\varepsilon} & \sqrt{\varepsilon} \\ \sqrt{\varepsilon} & a & b \\ \sqrt{\varepsilon} & b & a \end{pmatrix}, \tag{5.10}$$

where $a = (\sqrt{1-2\varepsilon}-1)/2$, $b = (\sqrt{1-2\varepsilon}+1)/2$ and ε is the coupling parameter with the reservoir, which varies between 0 and 1/2 for the uncoupled and fully coupled limits respectively[52]. The symmetry of the terms in the S matrix depends on which fields are present, as we will see below.

The lead coupling the ring to the reservoir needs two equivalent spin channels and thus can be expanded as

$$\psi_{lead}(x) = \sum_{\mu=1,2} \phi_{lead}(x)\chi^{(\mu)}(0) \qquad x \in (-\infty, 0] \ . \tag{5.11}$$

where x is the coordinate along the lead and $x = 0$ is defined as the coordinate at which the

lead connects to the ring, while the reservoir is at $x = -\infty$, and χ^μ is a two component spinor eigenstate of the σ_z. As the lead is not spin-orbit active the energies are $E = \hbar^2 k^2/2m$ The coefficients of the expansion in (5.11) are given by,

$$\phi_{lead}(x) = \sqrt{\mathcal{N}}\left(e^{ikx} + C_3 e^{-ikx}\right). \tag{5.12}$$

The normalization pre-factor is determined following Buttikers argument: in an energy interval $E, E + dE$, the differential of current injected into the lead is $dI = ev(dN/dE)f(E)dE$, where $f(E)$ is the Fermi distribution, $dN/dE = 1/2\pi\hbar v$ is the density of states of a perfect lead, and $v = \hbar k/m$. The wave function for the lead contemplates the correct current if $\mathcal{N} = f(E)dE/2\pi\hbar v$.

For the ring wave function, it is now a mixture of the four basis functions of the uncoupled case, so that we may accommodate for the new boundary conditions, we define

$$\Psi(\varphi) = C_1^1\psi_1^1(\varphi) + C_1^2\psi_1^2(\varphi) + C_2^1\psi_2^1(\varphi) + C_2^2\psi_2^2(\varphi) \tag{5.13}$$

The coefficients are to be fixed by imposing equality of the wave functions at $x = 0$ for $\varphi = 0$ and 2π. The dispersion problem is written as $\vec{\alpha}'^{(\mu)} = S\vec{\alpha}^{(\mu)}$, the coefficients $\vec{\alpha}^{(\mu)} = (\alpha^{(\mu)}, \beta^{(\mu)}, \gamma^{(\mu)})$ and $\vec{\alpha}'^{(\mu)} = (\alpha'^{(\mu)}, \beta'^{(\mu)}, \gamma'^{(\mu)})$ are found evaluating (5.12) at the junction at $x = 0$ for $\alpha^{(\mu)}$ and $\alpha'^{(\mu)}$, and evaluating ψ_2^μ in $\varphi = 0, 2\pi$ for the $\beta'^{(\mu)}$ and $\gamma^{(\mu)}$ respectively. The coefficients $\beta^{(\mu)}$ and $\gamma'^{(\mu)}$ evaluating ψ_1^μ in $\varphi = 0, 2\pi$ respectively. The set of equations can be cast, for each spin subspace as

$$\begin{pmatrix} \sqrt{\mathcal{N}}C_3^\mu \\ C_1^\mu \\ C_2^\mu \end{pmatrix} = \begin{pmatrix} -(a+b) & \sqrt{\varepsilon} & \sqrt{\varepsilon}e^{2\pi i n_1^\mu} \\ \sqrt{\varepsilon} & a & be^{2\pi i n_1^\mu} \\ \sqrt{\varepsilon}e^{-2\pi i n_2^\mu} & be^{-2\pi i n_2^\mu} & ae^{-2\pi i(n_1^\mu - n_2^\mu)} \end{pmatrix} \begin{pmatrix} \sqrt{\mathcal{N}} \\ C_2^\mu \\ C_1^\mu \end{pmatrix}. \tag{5.14}$$

where we have absorbed the phase factors into a redefined S matrix that manifestly displays the symmetry of the system: Note that we can invert for the quantum number as a function of the energy and fields

$$n_j^\mu = (-1)^j\sqrt{\frac{E}{\hbar\Omega}} + \frac{\Phi}{\Phi_0} - \frac{1}{2}\left(1 + (-1)^\mu\sqrt{1 + \left(\frac{\omega_{SO}}{\Omega}\right)^2}\right). \tag{5.15}$$

Referring to (5.10) one can readily check that, in the absence of magnetic or SO fields, $t_{jk} = t_{kj} = \sqrt{\varepsilon}e^{2\pi i n_1^\mu} = \sqrt{\varepsilon}e^{-2\pi i n_2^\mu}$ i.e. S is an orthogonal (symmetric) matrix, time reversal invariant. When the magnetic field is on but there is no SO coupling, then $t_{jk} \neq t_{kj}$ so $n_1^\mu \neq n_2^\mu$ and time reversal symmetry is broken. When the magnetic field is turned off and the SO coupling is present, time reversal symmetry is restored, and there is the additional symmetry for changing j and μ labels simultaneously. Thus the larger 6×6 matrix $S \otimes \mathbb{1}_s$ matrix is symplectic and embodies Kramer's degeneracy.

Solving the system of equations one can obtain each of the amplitudes

$$\begin{aligned} C_1^\mu &= \frac{\sqrt{\epsilon\mathcal{N}}\left(1-e^{2\pi i n_2^\mu}\right)}{\left(1-be^{2\pi i n_1^\mu}\right)\left(b-be^{2\pi i n_2^\mu}\right)+a^2\left(1-be^{2\pi i n_1^\mu}\right)}, \\ C_2^\mu &= \frac{\sqrt{\epsilon\mathcal{N}}\left(e^{2\pi i n_1^\mu}-1\right)}{\left(1-be^{2\pi i n_1^\mu}\right)\left(b-be^{2\pi i n_2^\mu}\right)+a^2\left(1-be^{2\pi i n_1^\mu}\right)}, \\ C_3^\mu &= \frac{\epsilon\left(e^{2\pi i n_1^\mu}-1+\left(1-e^{2\pi i n_2^\mu}\right)e^{2\pi i n_1^\mu}\right)}{\left(1-be^{2\pi i n_1^\mu}\right)\left(b-be^{2\pi i n_2^\mu}\right)+a^2\left(1-be^{2\pi i n_1^\mu}\right)} \\ &- (a+b). \end{aligned} \tag{5.16}$$

For the charge density the modulus squared of the coefficients acquire a particularly simple form in terms of the coupling parameters,

$$|C_1^\mu|^2 = \frac{2\varepsilon\mathcal{N}}{g^{(\mu)}}\left(1-\cos\left(2\pi n_2^\mu\right)\right), \tag{5.17}$$

$$|C_2^\mu|^2 = \frac{2\varepsilon\mathcal{N}}{g^{(\mu)}}\left(1-\cos\left(2\pi n_1^\mu\right)\right), \tag{5.18}$$

$$|C_3^\mu|^2 = 1, \tag{5.19}$$

where

$$\begin{aligned} g^{(\mu)} &= 3+\sqrt{1-2\varepsilon}-3\varepsilon-2\left(1+\sqrt{1-2\varepsilon}-\varepsilon\right)\cos\left(2\pi n_1^\mu\right)+2\sqrt{1-2\varepsilon}\cos\left(2\pi\left(n_1^\mu-n_2^\mu\right)\right)+ \\ &- 2\cos\left(2\pi n_2^\mu\right)+\cos\left(2\pi\left(n_1^\mu+n_2^\mu\right)\right)+\left(\sqrt{1-2\varepsilon}-\varepsilon\right)\left(-2\cos\left(2\pi n_2^\mu\right)+\cos\left(2\pi\left(n_1^\mu+n_2^\mu\right)\right)\right). \end{aligned} \tag{5.20}$$

Note the very important character of the model expressed in (5.19); the lead amplitude has modulus one, thus two opposite propagating waves superpose to give a constant amplitude, which means there is no net current (voltage probe condition) to or from the reservoir.
For the density of states (DOS) we know that the number of electron in the energy interval dE is given by $dN = |C_1^1|^2 + |C_1^2|^2 + |C_2^1|^2 + |C_2^2|^2$. As each amplitude modulus is proportional to the energy interval dE and using the chain rule $dN/dk = (dN/dE)(dE/dk) = (dN/dE)\hbar^2 k/m$. The number of electrons per unit energy range is given by

$$\frac{dN}{dE} = \sum_{i,\mu} \frac{\varepsilon f(E)}{\pi\hbar v} \frac{(1-\cos 2\pi n_i^\mu)}{g^{(\mu)}}, \tag{5.21}$$

Then the DOS is given by,

$$\frac{dN}{dk} = \frac{2\varepsilon}{\pi}\left(\frac{\sin^2(2\pi n_1^1) + \sin^2(2\pi n_2^1)}{g^{(1)}} + \frac{\sin^2(2\pi n_1^2) + \sin^2(2\pi n_2^2)}{g^{(2)}}\right). \tag{5.22}$$

The explicit relation between DOS and energy comes from substituting the expressions for $n_j^\mu = (-1)^j\sqrt{E/\hbar\Omega} + \Phi/\Phi_0 - 1/2\left(1 + (-1)^\mu\sqrt{1+(\omega_{SO}/\Omega)^2}\right)$ from the uncoupled problem. These expressions now define this quantum number which becomes a continuous function of the energy and flux and SO coupling, no longer restricted to be integer or half integer, as the problem is coupled.
The limit of zero fields (neither SO nor magnetic field) with coupling to the reservoir recovers Buttiker's result[9],

$$\frac{dN}{dk} = \frac{4\varepsilon\cos^2\left(2\pi\sqrt{\frac{E}{\hbar\Omega}}\right)}{\pi\left(-1+\varepsilon+\sqrt{1-2\varepsilon}\cos\left(2\pi\sqrt{\frac{E}{\hbar\Omega}}\right)\right)}.$$

Fig. 5.2 shows the DOS for $\varepsilon \neq 0$. The levels increasingly broaden around the quantized energies of the decoupled ring ($\varepsilon = 0$) as ε increases. The uncoupled quantized values correspond to the poles of the density of states at zero coupling, which obey the relation $E = m^2\hbar\Omega$, with m an integer (values $m^2 = 0, 1, 4, 9$ in figure). When coupling is turned on, the levels are shifted to lower energies as the levels broaden, as expected in general for complex self energy corrections. Deeper levels are less coupled to the reservoir than the shallower counterparts since there is partial transmission to the reservoir lead.
Making a correspondence between level broadening and electron lifetime, by fitting the resonance to a Lorentzian form leads to Figure 5.3. A power law decay of the lifetime with the

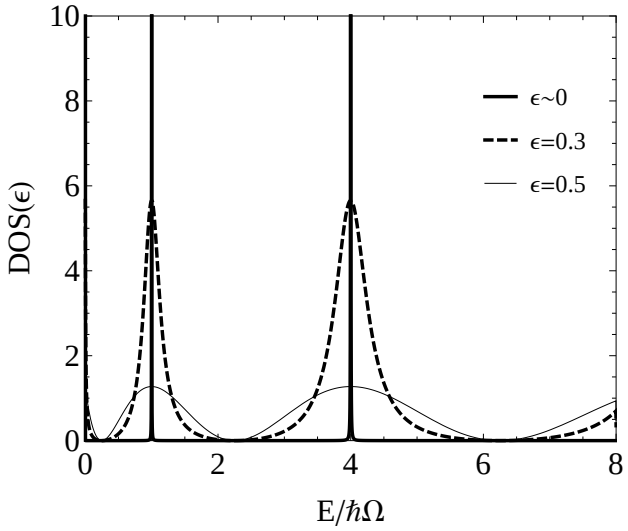

Figure 5.2: Density of states on the ring as a function of the energy for two values of the coupling parameter of the reservoir. ($\omega_{SO}/\Omega = 0$, $\Phi/\Phi_0 = 0$). The energy is expressed in units $E_0 = \hbar\Omega$ and the Fermi level is $E_F = 8E_0$.

reservoir coupling is observed for the smaller couplings.

The magnetic field shift the states and the SO coupling breaks the twofold degeneracy as was discussed. Fig. 5.4, depicts both the effect of the field and the SO. In panel a) each peak is doubly degenerate, while this degeneracy is broken with SO as depicted in panel b). Nevertheless this degeneracy can appear to exist when the coupling to the reservoir is sufficiently large (see panel b) for $\varepsilon = 0.5$).

5.3 Persistent charge currents

At zero temperature, the charge persistent currents in a decoupled ring can be calculated by the linear response relation [53, 51] $J_q = -\sum_i \frac{dE_i}{d\Phi}$ where i encloses the occupied states. The leading contribution to the current, due to cancellation of current contributions from state with opposite slopes, are the states close to the Fermi level. The linear response relation is not useful for the case we have coupling to the reservoir, since the energy broaden into a continuum of levels. On the other hand we have derived the exact wave functions from which the current

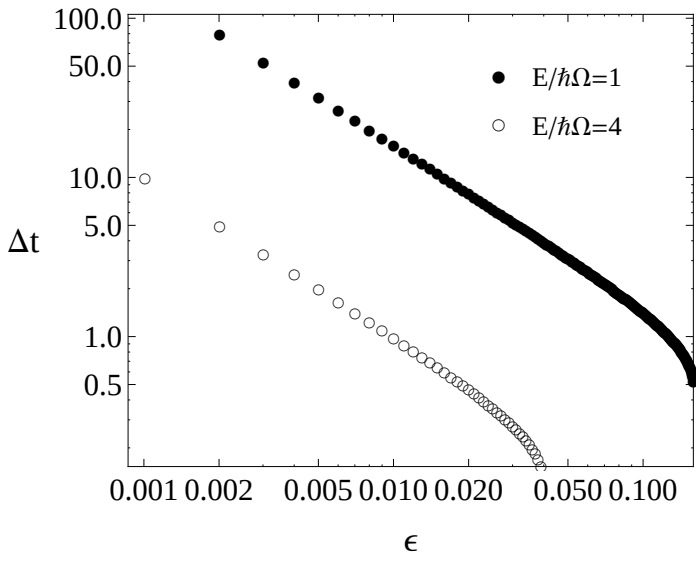

Figure 5.3: Lifetime of the electrons in the ring as a function of ε. The energies correspond to the quantized values of the decoupled states. The time is given in atomic units $1a.u \approx 2.4 \times 10^{-17} s$.

may be determined by the expectation value of the charge current operator $\Psi^{\dagger} e v_{\varphi} \Psi$ where

$$v_{\varphi} = a\dot{\varphi} = (a/i\hbar)[\varphi, H] = -2a\Omega \left(-i\frac{\partial}{\partial\varphi} - \frac{\Phi}{\Phi_0} + \frac{\omega_{SO}}{2\Omega}\sigma_{\rho} \right), \tag{5.23}$$

and integrating over all occupied states up to the Fermi level including the electron occupation numbers.

$$J_q = -\frac{2\varepsilon\hbar\Omega}{\Phi_0} \sum_{m,\mu} \int \frac{dE}{\hbar\Omega} \frac{f(E)}{\sqrt{\frac{E}{\hbar\Omega}}\, g^{\mu}} \sin^2(\pi n_m^{\mu}) \left[n_{\overline{m}}^{\mu} - \frac{\Phi}{\Phi_0} + \delta^{\mu} \right], \tag{5.24}$$

with

$$\delta^1 = \sin^2\frac{\theta}{2} + \frac{\omega_{SO}}{2\Omega}\sin\theta; \qquad \delta^2 = \cos^2\frac{\theta}{2} - \frac{\omega_{SO}}{2\Omega}\sin\theta, \tag{5.25}$$

where $\overline{m}$ is the complement value of m and a natural current scale $J_0 = \hbar\Omega/\Phi_0$ is identified. Note that $\varepsilon = 0$ does not imply zero current (in fact it is largest at zero coupling) as g^{μ} also depends on the coupling with a nontrivial limit behavior. We will separate the discussion into two cases: I) The Fermi level fixes $N = 6$ electrons, (see Fig 5.5 top panel)) and II) $N = 8$, (see Fig 5.5 bottom panel)). In the absence of RSO interaction for the first case, there are

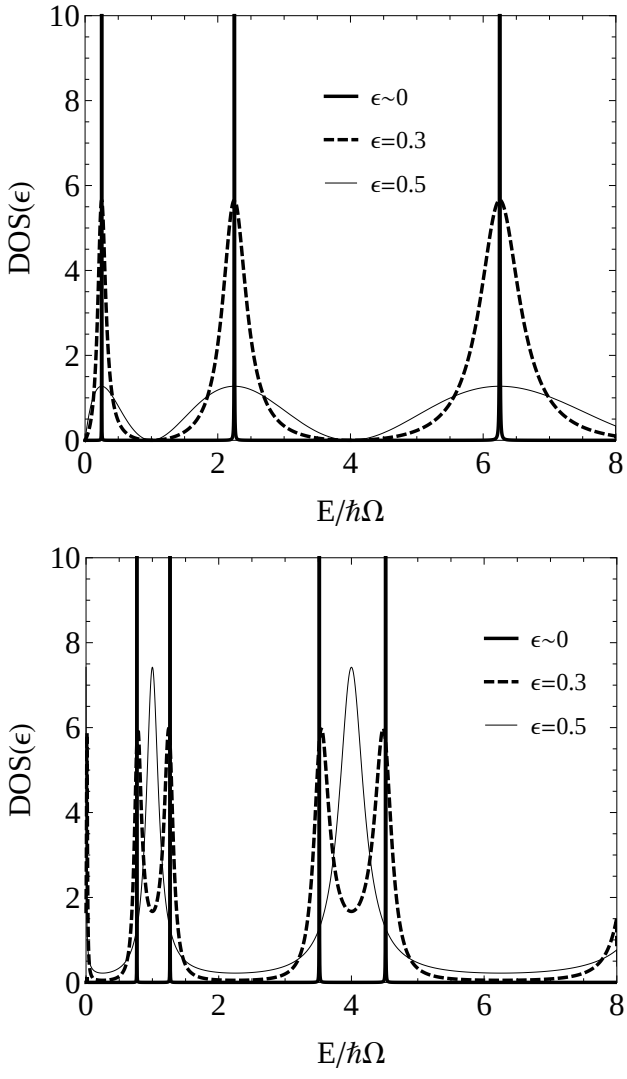

Figure 5.4: Density of states of the ring as a function of the energy for two values of ε and $T = 0$. The value of the parameters are a) $\omega_{SO}/\Omega = 0$, $\Phi/\Phi_0 = 0.5$ and b) $\omega_{SO}/\Omega = 0.75$, $\Phi/\Phi_0 = 0$.

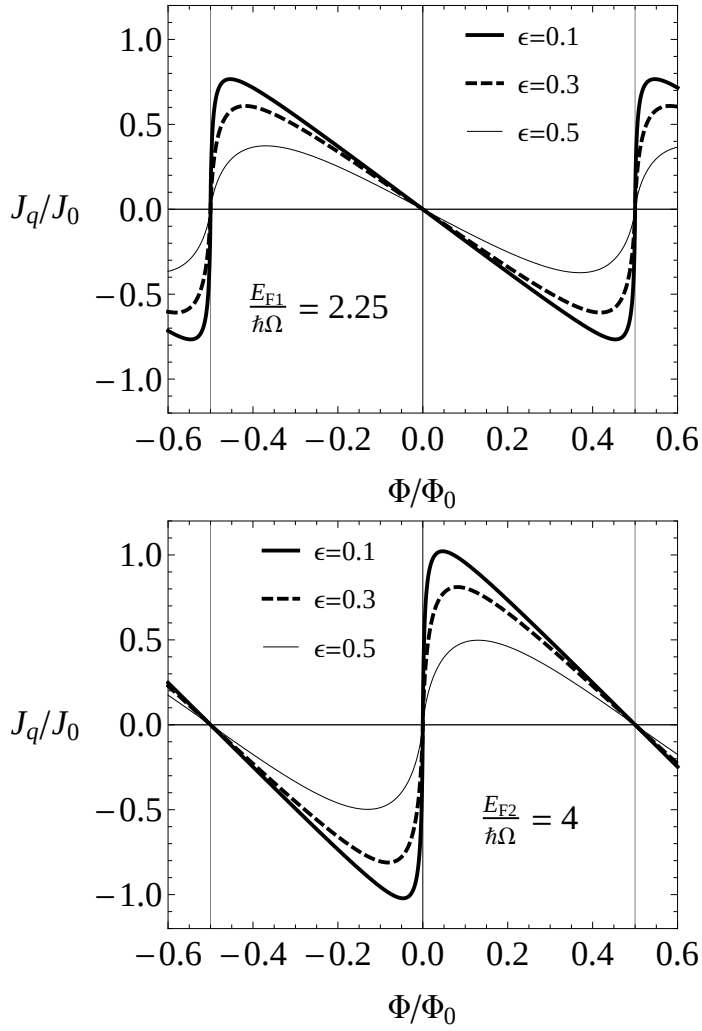

Figure 5.5: Charge persistent current as a function of the magnetic flux for three values of the reservoir coupling parameter. The number of electrons is 6 (top) and 8 (bottom) corresponding to a Fermi energy of $E_{F_1} =$ and $E_{F_2} =$. The RSO interaction is off and the persistent current is given in units $J_0 = \hbar\Omega/\Phi_0$.

two electrons, one with spin up and the other with spin down at each energy. At the Fermi level, two bands which describe electrons with different propagation numbers j cross each other at half integer steps in Φ_0 (see Fig.5.1). This results in a jump in the sign of the current at these values. In the second case the levels cross at zero or integer flux quanta, and the sign jump occurs at those points. These are the behaviours expected also for small couplings to the reservoir. Fig.5.5 shows the charge currents without the SO coupling as a function of the magnetic field. The reduction in amplitude of the current as a function of the coupling strength is evident as decoherence increases. For Fermi level E_{f_1} the persistent current is minimal for the smallest fluxes and gradually grows, while for E_{f_2} the current is maximal at the smallest fluxes and decreases thereof. After including RSO, the crossing between bands at the Fermi level shift to $\Phi/\Phi_0 = m/2 + (1 \pm \sqrt{1 + (\omega_{SO}\Omega)^2})/2$, with $m \in \mathbb{Z}$ for the case I) and $\Phi/\Phi_0 = m/2 + \pm\sqrt{1 + (\omega_{SO}\Omega)^2}/2$ for case II) displacing the current jumps and introducing two more for each of the Fermi level scenarios, See Fig 5.6.

The degradation of current with temperature has a distinctive character as compared to the coupling to the reservoir, as can be seen in Fig.5.7. The temperature effect will be small when the current emanates from a level appreciably below the Fermi level, so that few electrons are actually promoted to counter current states. On the other hand, for fluxes where the current are from levels close to the Fermi level, the currents quickly degrade. So this is a mechanism that is energy dispersion dependent. Such mechanism is also observed in other scenarios, for instance graphene rings which will be the subject of chapter 7. Figure 5.8 shows the dependence of charge current on temperature, for different ring-reservoir couplings. For certain ranges of the magnetic flux, the persistent current can be degraded completely. We estimate the magnitude of the thermal effects by using the temperature scale $T_0 = \hbar\Omega/k_B$, As Ω depends on the size of the ring, $T/T_0 = 0.5$ in the Figures, correspond to temperatures between 526 mK and 59 mK for ring sizes between 100 nm and 300 nm and an effective mass of $m^* = 0.042m_e$. This implies that the gap for persistent current degradation is of the order of 40μeV for the smallest of the rings. Improving this gap with either effective mass of ring radius and flux point of operation, might improve the thermal robustness of high sensitivity cantilevers for noise and electron thermometry.

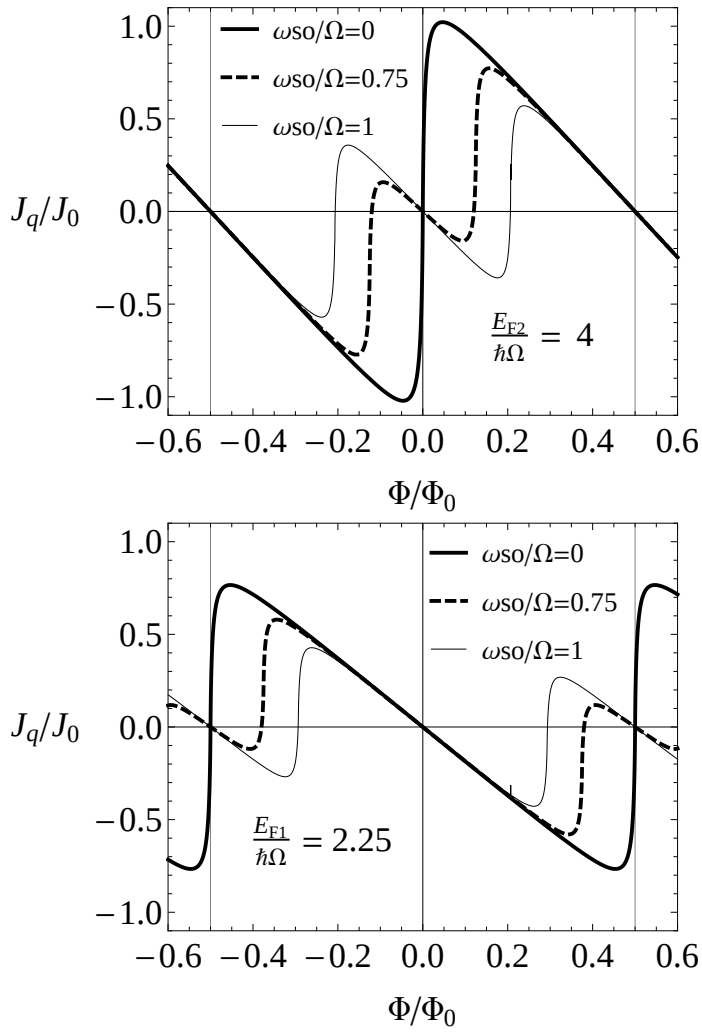

Figure 5.6: Charge persistent current as a function of the magnetic flux for different RSO values. The coupling is $\varepsilon = 0.1$ with the reservoir. The number of electrons is 6 (top) and 8 (bottom) corresponding to a Fermi energy of $E_{F_1} = 2.25$ and $E_{F_2} = 4$

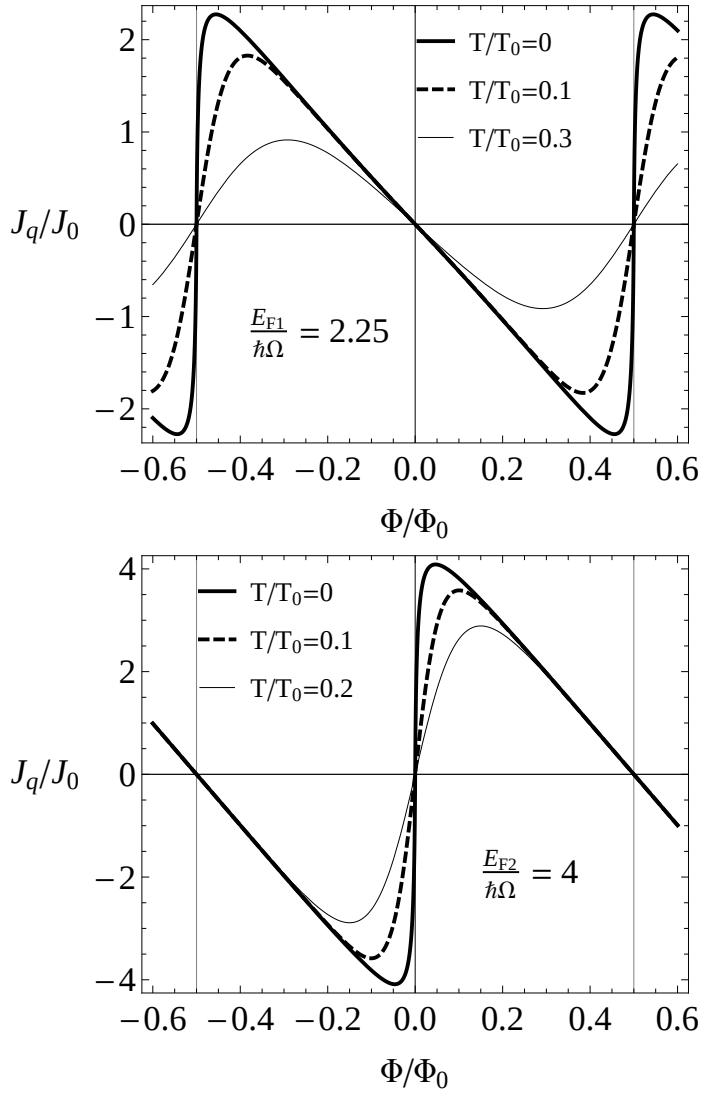

Figure 5.7: Charge persistent current as a function of the magnetic flux for different temperatures with $\varepsilon = 0.1$. The number of electrons is 6 (bottom) and 8 (top).

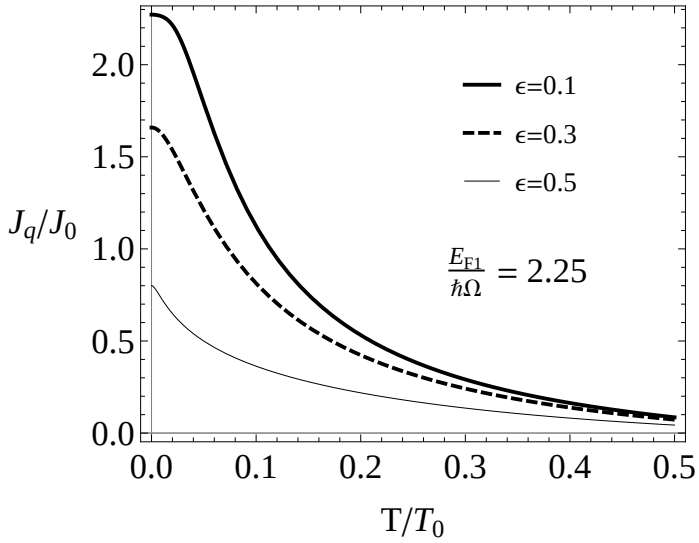

Figure 5.8: Temperature dependence of the charge current for 6 electrons. The maximal degradation is obtained with a combination of the coupling with the reservoir and increased temperature.

5.4 Persistent Spin currents

The standard calculation is through the anticommutator of the velocity with the spin operator [54, 51, 53],

$$\vec{J}_s = \frac{\hbar}{4}\Psi^\dagger\{\vec{\sigma}, \vec{v}\}\Psi.$$

Appealing to the coupled ring wave function derived above and the velocity operator in Eq. (5.23) one can derive the spin current as

$$J_s^z = -\varepsilon\hbar\Omega\sum_{m,\mu}\int\frac{dE}{\hbar\Omega}\frac{f(E)}{\pi\sqrt{\frac{E}{\hbar\Omega}}\,g^\mu}\sin^2(\pi n_m^\mu)\left[\left(n_{\overline{m}}^\mu - \frac{\Phi}{\Phi_0}\right)\beta^\mu + \gamma^\mu\right], \tag{5.26}$$

with

$$\begin{aligned}\gamma^1 &= \sin^2\frac{\theta}{2}, \qquad \gamma^2 = -\cos^2\frac{\theta}{2},\\ \beta^1 &= \cos\theta, \qquad \beta^2 = 1.\end{aligned}$$

In Figure 5.9 is drawn the spin persistent current as a function of the magnetic flux for the two Fermi levels considered in Fig.5.1. Spin currents are only possible in the presence of

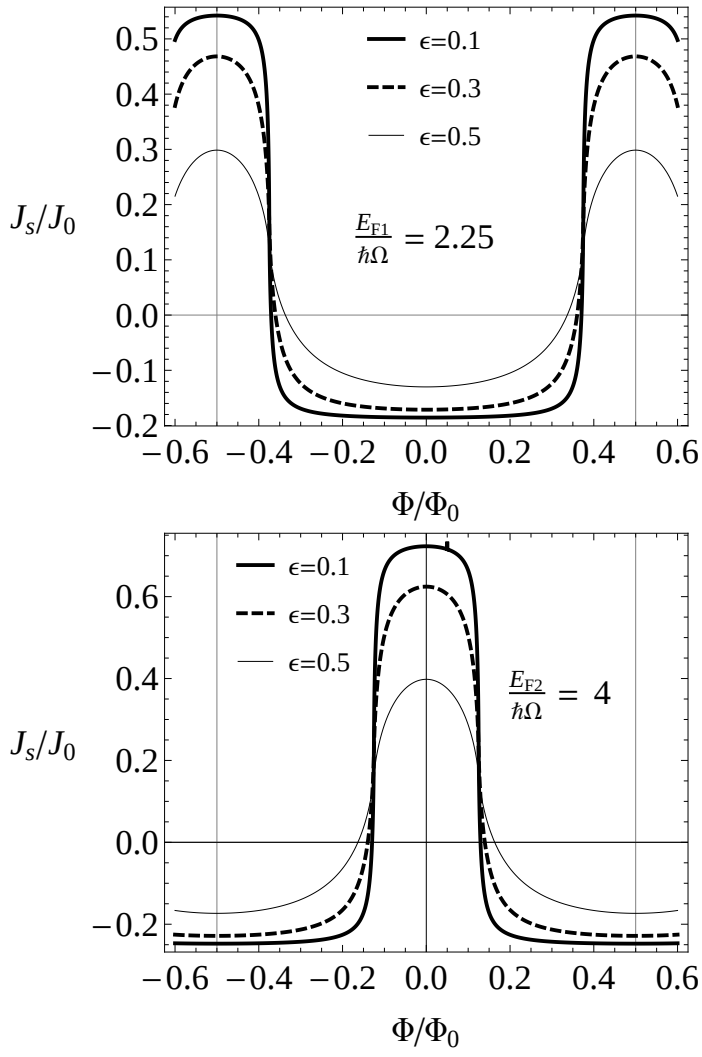

Figure 5.9: Spin persistent current as a function of the magnetic flux for three values of ε. The number of electrons is 6 (top) and 8 (bottom). The RSO is $\omega_{SO}/\Omega = 0.75$. The corrent is given in untis of $J_0 = \hbar v_f/4\pi a$.

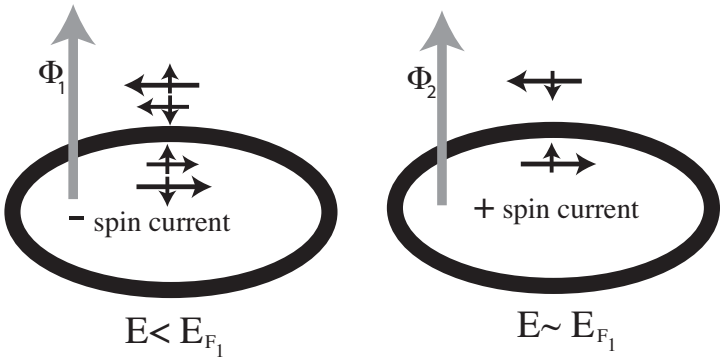

Figure 5.10: The figure depicts, qualitatively, the contributions to the spin current as the flux changes until the Fermi level is reached. On the left, the currents in each direction are highly compensated in spin (each current direction contains both spin directions). On the right, the flux is such that the energy is close to the Fermi level E_{F_1}, and the spin current is large and switches direction.

SO coupling, since spin degeneracy matches up identical contributions in charge current from opposite spins (see Fig.5.1 top panel). In the presence of the SO coupling there is a breaking of spin degeneracy with preservation of the time reversal symmetry, the necessary ingredients for their presence. As for charge currents, spin currents from deep levels in the Fermi sea, also tend to cancel but in a more complicated fashion. Figure 5.10 shows the combinations of charge currents with their corresponding spin orientations for the first Fermi level scenario: Deep in the Fermi sea charge currents are also paired up in spin but with small differences in electron velocities due to broken degeneracy. So we can see a small spin current accrued coming from theses levels. As one goes higher in magnetic field the positive current levels slow down, making less of a contribution, while the level with negative charge currents speed up, making the bulk of the current. The dispersion being quadratic makes for precise compensation, so that the full spin current is constant.

When the flux is large enough for the levels to cross the Fermi level, there is an abrupt disappearance of the negative spin up current and a new contribution from a positive spin up charge current, as shown in Fig.5.10 right panel. These two contributions make for a pure spin current, more than three times the magnitude of the previous regime, very close to the Fermi level E_{F_1}. The range of fluxes in which this happens is as wide as it takes for the second level to emerge from the Fermi sea i.e. $\Delta(\Phi/\Phi_0) = \sqrt{1+(\omega_{SO}/\Omega)^2} - 1$, at which point we start with the scenario on the left panel and repeat the whole periodic oscillation. For the second Fermi level the scenario is identical but it occurs for small fluxes in the center of the spectrum

(Fig.5.9 bottom panel). Figure 5.12 shows how the spin currents, coming from different parts of the spectrum explored by the magnetic flux, can be tuned by the spin-orbit interaction at fixed coupling to the reservoir. One can see how positive and negative spin currents can be enhanced and change the range of fluxes for which they arise.

It is interesting to note that the smaller spin current coming from levels deeper in the Fermi sea is more robust to decoherence than the contributions coming from close to the Fermi level, resembling thermal effects previously discussed. On the other hand, as discussed for the charge currents, the Buttiker model is unable to completely degrade spin currents.

The coupling with the reservoir acts degrading the charge currents, consequently the spin current diminish its magnitude since the electrons lifetime on those states is lesser but not produces total decoherence. See Fig 5.11. The intensity of the spin current is also modified in this scenario by the SO interaction, the strength of the Rashba coupling, which can be modulated by an electric field perpendicular to the plane of the ring, acts on the local phases as Aharonov-Casher contribution, changing the polarization on the crossing points in the spectrum as can be seen in Fig. 5.12.

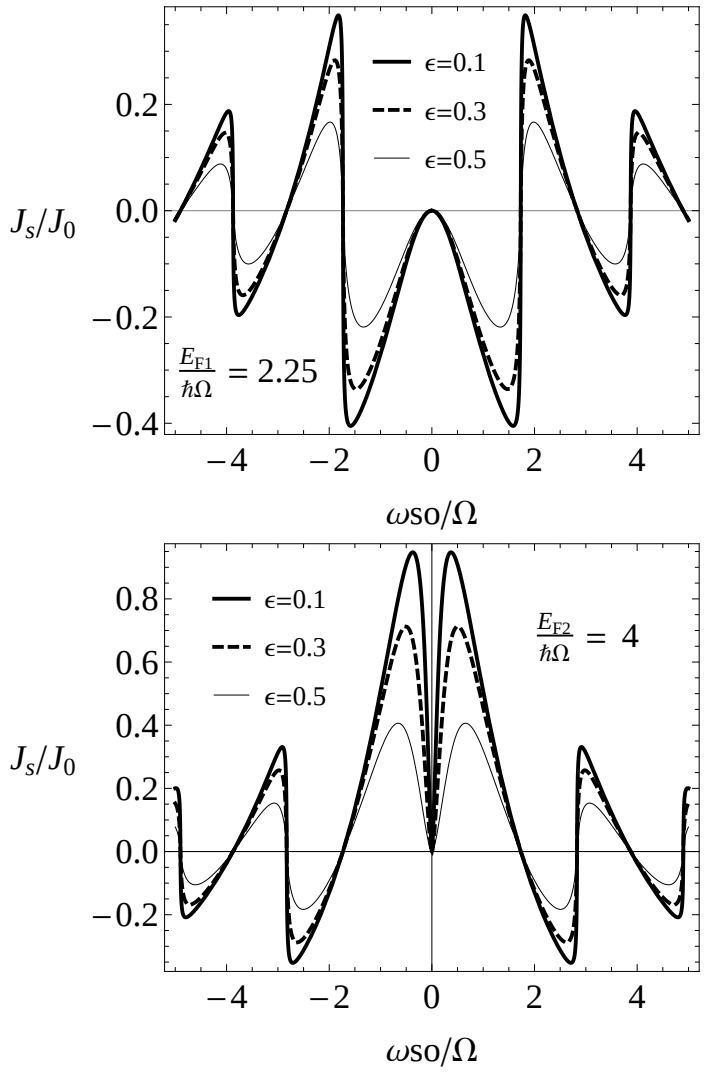

Figure 5.11: Spin persistent current as a function of the SO coupling for three values of ε. The number of electrons is 6 (top) and 8 (bottom).

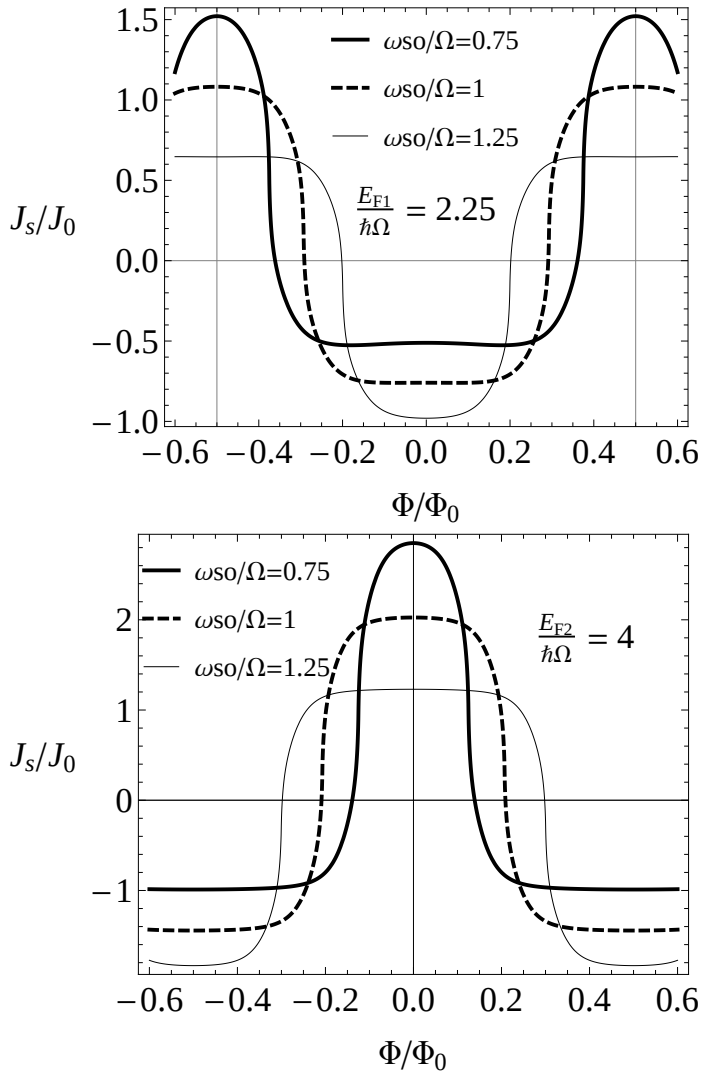

Figure 5.12: Spin persistent current as a function of the magnetic flux for three values of ω_{so}/Ω with finite temperature, $T/T_0 = 0.1$ and $\epsilon = 0.1$. The number of electrons is 6 (top) and 8 (bottom).

Chapter 6

Carbon two Dimensional Structure - Graphene

In this chapter we reviewed the some aspects of graphene that will be in the interest of our work. We focus on the basic definitions leaving to the more curious reader references to the most relevant literature on the subject.

6.1 The honeycomb lattice

In this chapter we introduce the more relevant features for graphene, that will be relevant in the next chapters. It is known that qraphene has turned out to be a wonderful material with high expectations about its applicability in so many different areas that it has be named the "miraculous material". It is essentially a monolayer of carbon atoms arranged in a honeycomb structure. In its pure state, close at the Fermi level, the band structure becomes linear in the so called "long-wavelength regime". In this linear regime the system can be essentially thought as consisting in effective massless electron, described by the Dirac equation [14, 3]. This particular behavior, now found in others materials, has given rise to an enormous and interesting bulk of theoretical work, giving the already known results in the Dirac systems and its extrapolations to condensed matter. Let us begin by considering a honeycomb lattice structure, which in the case of Graphene consists of carbon atoms in each lattice site.
The honeycomb lattice is not a Bravais lattice, so it is more convenient to describe it by the superposition of two triangular lattices often called A and B in the literature. Since these are periodical Bravais lattices we can make the description by means of a two atoms basis per unit

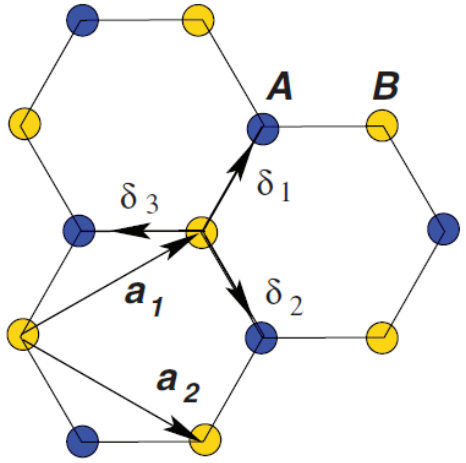

Figure 6.1: Unit cell for the honeycomb lattice as shown in reference [14]

cell, usually referred as sublattices. It is convenient to use the unit cell shown in the Figure 6.1 as in most of the literature.
Refering to the Fig. 6.1 we can write the lattice vectors,

$$\boldsymbol{a}_1 = a\left(\frac{3}{2}, \frac{\sqrt{3}}{2}\right) \tag{6.1}$$

$$, \boldsymbol{a}_2 = a\left(-\frac{3}{2}, \frac{\sqrt{3}}{2}\right). \tag{6.2}$$

The three vectors which connect a site on the A sublattice with a nearest neighbor (nn) on the B sublattice are given by δ_1, δ_2 and δ_3.

$$\boldsymbol{\delta}_1 = \frac{a}{2}\left(1, \sqrt{3}\right), \tag{6.3}$$

$$\boldsymbol{\delta}_2 = \frac{a}{2}\left(1, -\sqrt{3}\right), \tag{6.4}$$

$$\boldsymbol{\delta}_3 = -a\left(1, 0\right). \tag{6.5}$$

While the next nearest neighbor (nnn) connecting vectors are,

$$\boldsymbol{\delta}'_1 = \pm\boldsymbol{a}_1 \tag{6.6}$$
$$\boldsymbol{\delta}'_2 = \pm\boldsymbol{a}_2 \tag{6.7}$$
$$\boldsymbol{\delta}'_3 = \pm(\boldsymbol{a}_2 - \boldsymbol{a}_1). \tag{6.8}$$

6.2 Carbon atoms in a honeycomb lattice

Because the electrons wavefunctions are very localized around each site (atom sites), it is useful to write the Bloch functions of the two Bravais lattices in a localized basis. In the case of graphene this can be justified by thinking about the structure of carbon atoms in the lattice. Carbon is the 6th element of the periodic table, in the atomic ground state, the 6 electrons are in the configuration $1s^2 2s^2 2p^2$, i.e. 2 electrons fill the inner shell $1s$, which is close to the nucleus and which is irrelevant for chemical reactions, whereas 4 electrons occupy the outer shell of $2s$ and $2p$ orbitals. Because the $2p$ orbitals ($2p_x$, $2p_y$, and $2p_z$) are roughly ~ 4eV higher than the $2s$ orbital, it is energetically favorable to find 2 electrons in the $2s$ orbital and only 2 of them in the $2p$ orbitals. In the excited state, we have four equivalent states, $|2s\rangle$, $|2p_x\rangle$, $|2p_y\rangle$, and $|2p_z\rangle$. A superposition of the state $|2s\rangle$ with n $|2p_j\rangle$ states is called sp^n hybridisation, which play an essential role in covalent carbon bonds. For graphene is a superposition of the $2s$ and $2p$ orbitals. If we choose $|2p_x\rangle$ and $|2p_y\rangle$ then we have an sp^2 (σ bonds) hybridization.
The quantum states are written,

$$\begin{aligned}
|sp_1^2\rangle &= \frac{1}{\sqrt{3}}|2s\rangle - \sqrt{\frac{2}{3}}|2p_y\rangle, \\
|sp_2^2\rangle &= \frac{1}{\sqrt{3}}|2s\rangle + \sqrt{\frac{2}{3}}\left(\frac{\sqrt{3}}{2}|2p_x\rangle + \frac{1}{2}|2p_y\rangle\right), \\
|sp_3^2\rangle &= -\frac{1}{\sqrt{3}}|2s\rangle + \sqrt{\frac{2}{3}}\left(-\frac{\sqrt{3}}{2}|2p_x\rangle + \frac{1}{2}|2p_y\rangle\right).
\end{aligned}$$

The orbitals are in the xy-plane and have 120° between each other. The remaining $|2p_z\rangle$ is perpendicular to the plane (π bonds).
Therefore the dynamics of the electrons occurs in the localized π orbitals. Based on this, we

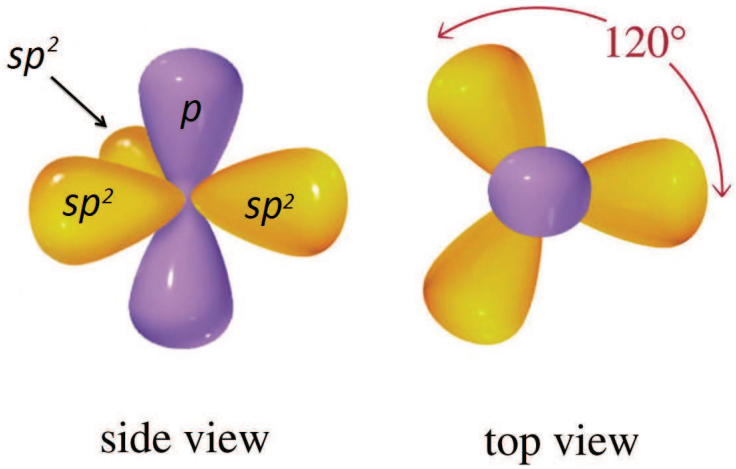

start the electronic structure derivation by the following ansatz,

$$\Psi_{\boldsymbol{k}}(\boldsymbol{x}) = \sum_{\boldsymbol{R}} e^{i\boldsymbol{k}\cdot\boldsymbol{R}}\phi(\boldsymbol{x}-\boldsymbol{R}), \tag{6.9}$$

where the sum is over all the lattice vectors $\boldsymbol{R} = n\boldsymbol{a}_1 + m\boldsymbol{a}_2$ [1].
The $\phi(\boldsymbol{x}-\boldsymbol{R})$ are the atomic wavefunctions which are built in order to fullfil the Bloch condition,

$$\Psi_{\boldsymbol{k}}(\boldsymbol{x})e^{i\boldsymbol{k}\cdot\boldsymbol{R}} = \Psi_{\boldsymbol{k}}(\boldsymbol{x}+\boldsymbol{R})$$

There are two atoms per unit cell, then the atomic wavefunction must have two contributions, each due to the corresponding hexagonal sublattice (A,B)

$$\phi(\boldsymbol{x}) = b_A\phi_A(\boldsymbol{x}+\boldsymbol{\delta}_A) + b_B\phi_B(\boldsymbol{x}+\boldsymbol{\delta}_B)$$

where the b_i are complex functions of $\boldsymbol{k}$. Using this in the equation (6.9),

$$\Psi_{\boldsymbol{k}}(\boldsymbol{x}) = \sum_{\boldsymbol{R}} e^{i\boldsymbol{k}\cdot\boldsymbol{R}} b_A\phi_A(\boldsymbol{x}-\boldsymbol{R}+\boldsymbol{\delta}_A) + \sum_{\boldsymbol{R}} e^{i\boldsymbol{k}\cdot\boldsymbol{R}} b_B\phi_B(\boldsymbol{x}-\boldsymbol{R}+\boldsymbol{\delta}_B). \tag{6.10}$$

[1] $\sum_{\boldsymbol{R}}$ is a shortcut for $\sum_n \sum_m$, with n and m integers

6.2.1 Tight-Binding approach to Graphene

In order to construct the tight-binding (TB) Hamiltonian for electrons in graphene we will consider that electrons can hop to both nearest- and next-nearest-neighbor atoms. Let us start with the Hamiltonian of a single electron in the atomic potential due to all carbon atoms in the lattice,

$$H = \frac{p^2}{2m} + \sum_{\boldsymbol{R}} \left(V_a(\boldsymbol{x} - \boldsymbol{\delta}_A - \boldsymbol{R}) + V_a(\boldsymbol{x} - \boldsymbol{\delta}_B - \boldsymbol{R}) \right) \tag{6.11}$$

The action of this Hamiltonian on the atomic wavefuntions gives,

$$\begin{aligned} H\phi(\boldsymbol{x}) &= \left(\frac{p^2}{2m} + V_a(\boldsymbol{x} - \boldsymbol{\delta}_{A,B}) \right) \phi_{A,B}(\boldsymbol{x} + \boldsymbol{\delta}_{A,B}) + \\ &+ \sum_{\boldsymbol{R} \neq 0} \left(V_a(\boldsymbol{x} - \boldsymbol{\delta}_A - \boldsymbol{R}) + V_a(\boldsymbol{x} - \boldsymbol{\delta}_B - \boldsymbol{R}) + V_a(\boldsymbol{x} - \boldsymbol{\delta}_{B,A}) \right) \phi_{A,B}(\boldsymbol{x} + \boldsymbol{\delta}_{A,B}) \\ &= H_a \phi_{A,B}(\boldsymbol{x} + \boldsymbol{\delta}_{A,B}) + \Delta U_{A,B} \phi_{A,B}(\boldsymbol{x} + \boldsymbol{\delta}_{A,B}) \\ &= \epsilon_{\boldsymbol{k}} \phi_{A,B}(\boldsymbol{x} + \boldsymbol{\delta}_{A,B}) + \Delta U_{A,B} \phi_{A,B}(\boldsymbol{x} + \boldsymbol{\delta}_{A,B}), \end{aligned}$$

where H_a is the atomic Hamiltonian of the carbon atom on the corresponding site and $\Delta U_{A,B}\phi_{A,B}(\boldsymbol{x}) = \sum_{\boldsymbol{R} \neq 0} \left(V_a(\boldsymbol{x} - \boldsymbol{\delta}_A - \boldsymbol{R}) + V_a(\boldsymbol{x} - \boldsymbol{\delta}_B - \boldsymbol{R}) + V_a(\boldsymbol{x} - \boldsymbol{\delta}_{B,A}) \right)$.

The atomic wavefunctions $\phi_{A,B}(\boldsymbol{x})$ are solutions of the crystal Hamiltonian, given the b_i.

$$\begin{pmatrix} b_A^* & b_B^* \end{pmatrix} (H_{\boldsymbol{k}} - E_{\boldsymbol{k}} S_{\boldsymbol{k}}) \begin{pmatrix} b_A \\ b_B \end{pmatrix} = 0,$$

for arbitrary $b's$, excluding the trivial solution $b_A = b_B = 0$. with,

$$H_{\boldsymbol{k}} = N(\epsilon_{\boldsymbol{k}} S_{\boldsymbol{k}} + t_{\boldsymbol{k}}) \tag{6.12}$$

where $\epsilon_{\boldsymbol{k}}$ are the eigenvalues of the carbon atomic Hamiltonian H_a. We find the matrix elements and define the hopping matrix $t_{\boldsymbol{k}}$ and the overlap matrix $S_{\boldsymbol{k}}$,

$$
\begin{aligned}
t^{ij}_{\boldsymbol{k}} &= \sum_{\boldsymbol{R}_l} e^{i\boldsymbol{k}\cdot\boldsymbol{R}_l} \int \phi^*_i(\boldsymbol{x}+\boldsymbol{\delta}_i)\Delta U \phi_j(\boldsymbol{x}-\boldsymbol{R}_l+\boldsymbol{\delta}_j)d\boldsymbol{x}, \\
S^{ij}_{\boldsymbol{k}} &= \sum_{\boldsymbol{R}_l} e^{i\boldsymbol{k}\cdot\boldsymbol{R}_l} \int \phi^*_i(\boldsymbol{x}+\boldsymbol{\delta}_i)\phi_j(\boldsymbol{x}-\boldsymbol{R}_l+\boldsymbol{\delta}_j)d\boldsymbol{x}.
\end{aligned}
$$

Since each atoms has the same electronic configuration, the contribution due to each atomic energy $\epsilon_{\boldsymbol{k}}$ is the same, hence it is a shift to energy spectrum. Without losing generality we set $\epsilon_{\boldsymbol{k}} = 0$ as a reference energy. Taking the origin on the sites of the sublattice A, we see that,

$$
\begin{aligned}
\boldsymbol{\delta}_A &= 0 \\
\boldsymbol{\delta}_B &= \boldsymbol{\delta}_{BA} = \boldsymbol{\delta}.
\end{aligned}
$$

By using this we can write the matrix elements explicitly,

$$
t^{AB}_{\boldsymbol{k}} = (t^{BA}_{\boldsymbol{k}})^* \approx \int \phi^*_A(\boldsymbol{x})\Delta U_B \phi_B(\boldsymbol{x}+\boldsymbol{\delta})d\boldsymbol{x} + e^{-i\boldsymbol{k}\cdot\boldsymbol{a}_1}\int \phi^*_A(\boldsymbol{x})\Delta U_B \phi_B(\boldsymbol{x}+\boldsymbol{\delta}+\boldsymbol{a}_1)d\boldsymbol{x} + \\
+e^{-i\boldsymbol{k}\cdot\boldsymbol{a}_2}\int \phi^*_A(\boldsymbol{x})\Delta U_B \phi_B(\boldsymbol{x}+\boldsymbol{\delta}+\boldsymbol{a}_2)d\boldsymbol{x}.
$$

The non-diagonal elements are the nearest neighbor (nn) hopping terms. This can be seen by noting that any nn hopping will drop-on in different sublattice, ($A, B \to nn \to B, A$).
It is useful to note that the we are allowed to sum over all the lattice vectors $\boldsymbol{R}$ that hop to a different sublattice (e.g. nnn hopping), but we will keep only nn terms due to the extremely localized nature of the wave function. Since each nn hopping has the same amplitude, then the hopping integrals has the same value. Given this,

$$
t^{AB}_{\boldsymbol{k}} = (t^{BA}_{\boldsymbol{k}})^* \approx t\left(1 + e^{-i\boldsymbol{k}\cdot\boldsymbol{a}_1} + e^{-i\boldsymbol{k}\cdot\boldsymbol{a}_2}\right) = t\alpha(\boldsymbol{k})^*,
$$

with t the hopping nn amplitude.
The diagonal elements are the next nearest neighbor (nnn) contributions. As before it can be argued that a displacement to a second neighbor or nnn, drops on the same sublattice

$(A, B \to nnn \to A, B)$ but the higher orders in the sum are dismissed because they correspond to even higher contributions, where the localized atomic wavefunctions is almost absent.

$$t_{\boldsymbol{k}}^{AA} = t_{\boldsymbol{k}}^{BB} \approx t' \left(e^{i\boldsymbol{k}\cdot\boldsymbol{a}_1} + e^{i\boldsymbol{k}\cdot\boldsymbol{a}_2} + e^{-i\boldsymbol{k}\cdot\boldsymbol{a}_1} + e^{-i\boldsymbol{k}\cdot\boldsymbol{a}_2} + e^{-i\boldsymbol{k}\cdot(\boldsymbol{a}_2-\boldsymbol{a}_1)} + e^{i\boldsymbol{k}\cdot(\boldsymbol{a}_2-\boldsymbol{a}_1)} \right),$$

where the hopping amplitude between nnn is the same in each direction (given the symmetry of the lattice) and t' is the nnn amplitude. We can rewrite this in terms of $\alpha(\boldsymbol{k})$,

$$t_{\boldsymbol{k}}^{AA} = t_{\boldsymbol{k}}^{BB} \approx t' \left(|\alpha(\boldsymbol{k})|^2 - 3 \right).$$

Then the overlap matrix elements is,

$$S_{\boldsymbol{k}}^{AB} = (S_{\boldsymbol{k}}^{BA})^* \approx s \left(1 + e^{-i\boldsymbol{k}\cdot\boldsymbol{a}_1} + e^{-i\boldsymbol{k}\cdot\boldsymbol{a}_2} \right) = s\alpha(\boldsymbol{k})^*,$$

with s the overlapping of the wavefuntions between nn. The overlapping between each nn is considered to be of the same magnitude due to the symmetry of the lattice. The non-diagonal terms again are those that connect two different sublattices, and we kept only nn since the overlapping of the localized wavefuntions decay rapidly off-site.

Using the same argument as above, the diagonal elements that connects nnn are

$$S_{\boldsymbol{k}}^{AA} = S_{\boldsymbol{k}}^{BB} \approx s' \left(|\alpha(\boldsymbol{x})|^2 - 3 \right)$$

We will neglect the nnn contribution due to the overlapping.

6.3 The band structure

in order to construct the band structure we solve the obtained Hamiltonian in the TB approach. The secular equation reads,

$$\det\begin{pmatrix} E_{\boldsymbol{k}} - t'(|\alpha(\boldsymbol{k})|^2 - 3) & (sE_{\boldsymbol{k}} - t)\alpha(\boldsymbol{k})^* \\ (sE_{\boldsymbol{k}} - t)\alpha(\boldsymbol{k}) & E_{\boldsymbol{k}} - t'(|\alpha(\boldsymbol{k})|^2 - 3), \end{pmatrix} = 0$$

$$\begin{aligned} (E_{\boldsymbol{k}} - t'(|\alpha(\boldsymbol{k})|^2 - 3))^2 &- (sE_{\boldsymbol{k}} - t)^2\alpha(\boldsymbol{k})\alpha^*(\boldsymbol{k}) = 0 \\ 3t' - t'|\alpha(\boldsymbol{k})|^2 + E_{\boldsymbol{k}} &= \mp t|\alpha(\boldsymbol{k})| \pm sE_{\boldsymbol{k}}|\alpha(\boldsymbol{k})| \\ E_{\boldsymbol{k}} &= \frac{3t' - t'|\alpha(\boldsymbol{k})|^2 \pm t|\alpha(\boldsymbol{k})|}{\pm s|\alpha(\boldsymbol{k})| - 1}, \end{aligned}$$

which defining $\lambda = \mp$ is,

$$E_{\boldsymbol{k}} = \frac{t'|\alpha(\boldsymbol{k})|^2 - 3t' + \lambda t|\alpha(\boldsymbol{k})|}{1 + \lambda s|\alpha(\boldsymbol{k})|}.$$

This expression can be expanded under the assumption that the overlapping is very small ($s \ll 1$) and the nnn hopping is also small compared with the nn hopping ($t' \ll t$), then,

$$E_{\boldsymbol{k}} \approx \left(t'|\alpha(\boldsymbol{k})|^2 - 3t' + \lambda t|\alpha(\boldsymbol{k})|\right)\left(1 - \lambda s|\alpha(\boldsymbol{k})|\right),$$

$$\begin{aligned} E_{\boldsymbol{k}} &\approx t'|\alpha(\boldsymbol{k})|^2 - 3t' + \lambda t|\alpha(\boldsymbol{k})| - \lambda s t'|\alpha(\boldsymbol{k})|^3 + \lambda 3t's|\alpha(\boldsymbol{k})| - st|\alpha(\boldsymbol{k})|^2 \\ &= t\left(\frac{t'}{t}|\alpha(\boldsymbol{k})|^2 - 3\frac{t'}{t} + \lambda|\alpha(\boldsymbol{k})| - \frac{t'}{t}\lambda s|\alpha(\boldsymbol{k})|^3 + \frac{t'}{t}\lambda 3s|\alpha(\boldsymbol{k})| - s|\alpha(\boldsymbol{k})|^2\right) \\ &\approx t\left(\lambda|\alpha(\boldsymbol{k})| - s|\alpha(\boldsymbol{k})|^2\right) \\ &\approx t\lambda|\alpha(\boldsymbol{k})| - ts|\alpha(\boldsymbol{k})|^2, \end{aligned}$$

and where,

$$|\alpha(\boldsymbol{k})| = \sqrt{3 + 2\cos(\boldsymbol{k}\cdot\boldsymbol{a}_1) + 2\cos(\boldsymbol{k}\cdot\boldsymbol{a}_2) + 2\cos(\boldsymbol{k}\cdot(\boldsymbol{a}_2 - \boldsymbol{a}_1))}.$$

Which is explicitly written as

$$|\alpha(\boldsymbol{k})| = \sqrt{1+4\cos\left(a\frac{k_x}{2}\right)\cos\left(a\frac{\sqrt{3}}{2}k_y\right)+4\cos\left(\frac{a}{2}k_x\right)^2}.$$

We finally write,

$$E_{\boldsymbol{k}} = t\lambda\sqrt{1+4\cos\left(a\frac{k_x}{2}\right)\cos\left(a\frac{\sqrt{3}}{2}k_y\right)+4\cos\left(\frac{a}{2}k_x\right)^2} - \\ -ts\left(1+4\cos\left(a\frac{k_x}{2}\right)\cos\left(a\frac{\sqrt{3}}{2}k_y\right)+4\cos\left(\frac{a}{2}k_x\right)^2\right),$$

which for $s \ll 1$ is,

$$E_{\boldsymbol{k}} = t\lambda\sqrt{1+4\cos\left(a\frac{k_x}{2}\right)\cos\left(a\frac{\sqrt{3}}{2}k_y\right)+4\cos\left(\frac{a}{2}k_x\right)^2}.$$

The conduction and valence bands touch in six inequivalent points around the Fermi level (in absence of impurities and external perturbations).
Around these points the energy is linear with respect to $|\boldsymbol{k}|$. As can be seen in the Figure 6.3. The corners are called Dirac points, due to the strong similarity with the linear dispersion relation with the Dirac equation for massless electrons, they correspond to $\alpha(\boldsymbol{k}) = 0$, or,

$$\boldsymbol{K} = (\frac{4\pi}{3a}, 0), \tag{6.13}$$

$$\boldsymbol{K}' = (-\frac{4\pi}{3a}, 0) = -\boldsymbol{K}. \tag{6.14}$$

Other Dirac points can be connected through a linear combinations of $\boldsymbol{K}$ or $\boldsymbol{K}'$ through the reciprocal lattice vectors.

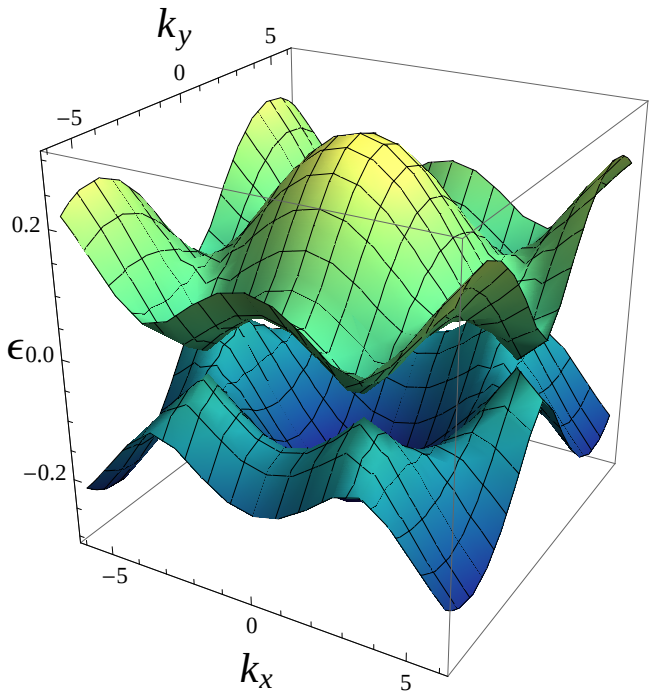

Figure 6.2: The bandstructure for a pure sample of flat graphene calculated with Tight-binding. The border of the zone touches at six point, the Dirac points.

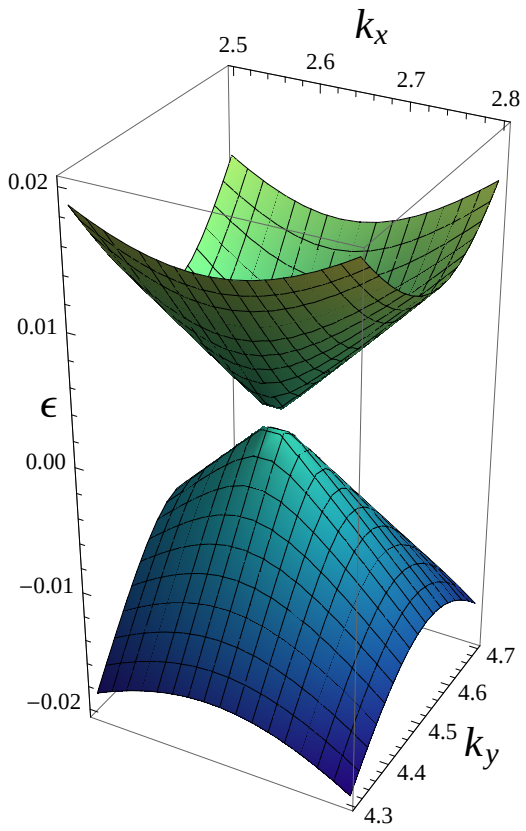

Figure 6.3: Closer to the gapless point the spectrum behaves linearly, the conical shape emulates massless Dirac particles.

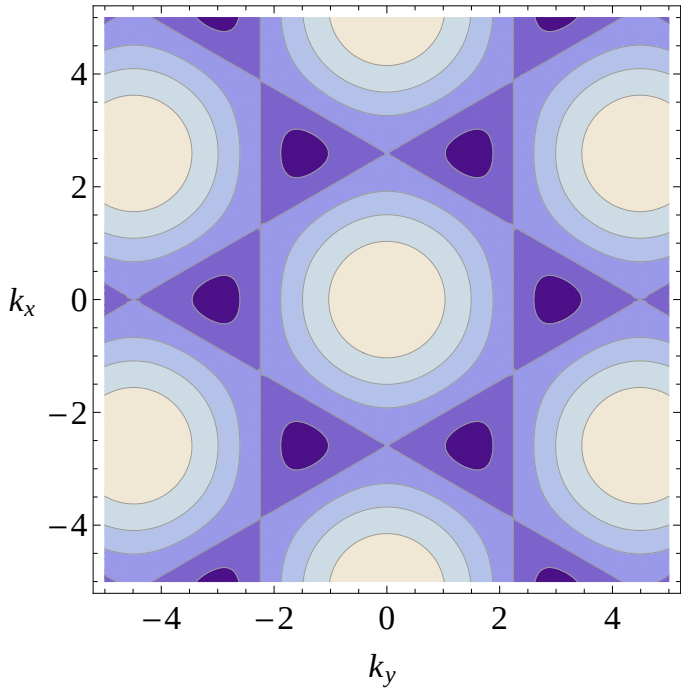

Figure 6.4: Inequivalent Dirac K points. The corners of the zone (in dark blue) where the conduction and valence band are gapless.

6.4 The long wavelength limit - Dirac-like Hamiltonian

Since there are no external interactions or impurities the low energy excitations at the Fermi level are around the Dirac points. We may expand the energy dispersion around the points K and K', then the wave vector is decomposed as $\boldsymbol{k} = \boldsymbol{K} + \boldsymbol{k}$.
We make th expansion of the term $\alpha(\boldsymbol{K} + \boldsymbol{k})$ obtaining,

$$\alpha(\boldsymbol{K} + \boldsymbol{k}) \approx a\frac{\sqrt{3}}{2}\left(k_x - ik_y\right). \tag{6.15}$$

Similarly for $\boldsymbol{K}'$

$$\alpha(\boldsymbol{K}' + \boldsymbol{k}) \approx a\frac{\sqrt{3}}{2}\left(k_x + ik_y\right).$$

We can write then

$$\alpha(\pm\boldsymbol{K} + \boldsymbol{k}) \approx a\frac{\sqrt{3}}{2}\left(k_x \pm ik_y\right) = a\frac{\sqrt{3}}{2}\left(k_x + \tau ik_y\right),$$

where $\tau = \pm$ and labels the corresponding Dirac point.
From the equation (6.12), neglecting the overlapping contributions (tight binding approach) we can write,

$$H_t = t'(|\alpha(\boldsymbol{k})|^2 - 3)\begin{pmatrix} 1 & 0 \\ 0 & 1 \end{pmatrix} + t\begin{pmatrix} 0 & \alpha(\boldsymbol{k})^* \\ \alpha(\boldsymbol{k}) & 0 \end{pmatrix}. \tag{6.16}$$

Using the $\boldsymbol{k} = \tau\boldsymbol{K} + \boldsymbol{k}$ approximation, neglecting the nnn hopping terms and defining $v_F = at\frac{\sqrt{3}}{2\hbar}$, we obtain,

$$H_t = \hbar v_F\left(k_x\boldsymbol{\sigma}_x + \tau k_y\boldsymbol{\sigma}_y\right). \tag{6.17}$$

The Hamiltonian resembles the Dirac-Weyl "free" Hamiltonian that describes masless electrons. The σ are the Pauli matrices and τ stands for the respective Dirac point $\boldsymbol{K}$. The $\boldsymbol{\sigma}$ operates mixing the A and B sublattice. This can be seen from equation (6.12), where the matrices acts

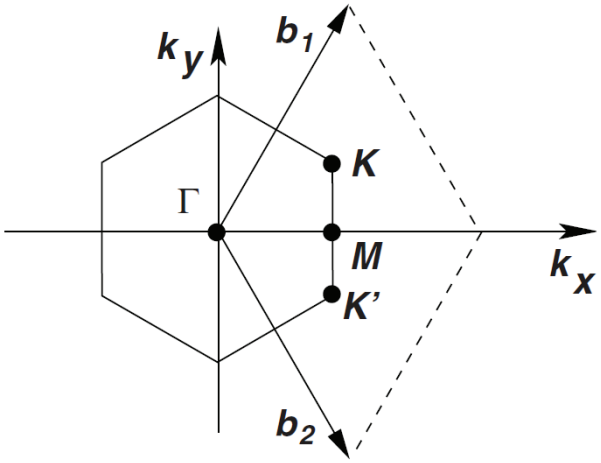

Figure 6.5: Figure from [14]. The first Brillouin zone is a hexagonal lattice. The time reversal symmetry can be seen as a reflection along the k_x axis from the point M.

on two components spinors, each of the components describes an specific sublattice. Then on the construction of equation (6.16) is clear that $\boldsymbol{\sigma}$ matrices acts on the sublattice space. This will translate into a two band energy description in Fourier space as the electron(particles) and holes(antiparticles) components of the spinor. The resemblance with Dirac massless equation is remarkable, nevertheless the $\boldsymbol{\sigma}$'s has not to be associated with the real spin although it is a two level state, will in the next chapter that it plays a relevant role in the conservation of the total angular momentum for a graphene ring. It is clear that the effective Hamiltonian (6.17) is made of two copies of the massless Diraclike Hamiltonian, one holding for $\boldsymbol{q}$ around $\boldsymbol{K}$ and the other for $\boldsymbol{q}$ around $\boldsymbol{K}'$. The wavefunction, in momentum space, around the Dirac points is

$$\Psi_{\boldsymbol{K}}(\boldsymbol{k}) = \frac{1}{\sqrt{2}} \begin{pmatrix} e^{-i\phi_{\boldsymbol{K}}/2} \\ \pm e^{i\phi_{\boldsymbol{K}}/2} \end{pmatrix}, \tag{6.18}$$

where $\theta_{\boldsymbol{K}} = \tan^{-1}\left(\frac{k_y}{k_x}\right)$. The wave functions in the point $\boldsymbol{K}$ is connected by time reversal symmetry with the wave function at the point $\boldsymbol{K}'$. Setting the origin of coordinates in the M point time reversal is a reflection along the k_x axis. See Fig. 6.4
Note that a rotation in $\theta = 2\pi$ change the sign of the wave function, a characteristic feature of spinors. As in relativistic quantum mechanics the helicity is often used to characterize the eigenfunctions. In the context of graphene is defined as the projection of the momentum

operator in the pseudospin direction. It has the form

$$\hat{h} = \frac{1}{2}\boldsymbol{\sigma} \cdot \frac{\boldsymbol{p}}{|\boldsymbol{p}|}. \tag{6.19}$$

Where it can be seen that the "free" Hamiltonian eigenstates are also states of the helicity, with eigenvalues $\pm\frac{1}{2}$.

Chapter 7

Mesoscopic Graphene Ring in the Continuous Limit

As an interesting alternative to semiconductors ring we can focus on graphene as active media, with SO interaction, both due to its crystal field (ISO) and external field (Rashba type) coupling. A quasi one-dimensional ring of finite width, is cut out from a flat graphene monolayer as shown in Fig.7.1. Localized and discrete confined modes exist in the radial direction (see [55] for the case of carbon nano ribbons), while the angular direction is free, though appropriate closing conditions for the wave functions are to be applied. The Hamiltonian is given in[2], where there is SO interaction in the so called long wavelength limit around the Dirac points,

$$\begin{aligned} H &= -i\hbar v_F(\boldsymbol{\tau}_z\boldsymbol{\sigma}_x\mathbb{1}_s\partial_x + \mathbb{1}_\tau\boldsymbol{\sigma}_y\mathbb{1}_s\partial_y) \\ &\quad +\Delta_{\mathrm{SO}}\boldsymbol{\tau}_z\boldsymbol{\sigma}_z\mathsf{s}_z + \lambda_{\mathrm{R}}(\boldsymbol{\tau}_z\boldsymbol{\sigma}_x\mathsf{s}_y - \mathbb{1}_\tau\boldsymbol{\sigma}_y\mathsf{s}_x). \end{aligned} \tag{7.1}$$

The first term is the kinetic energy, it has the form $v_F\boldsymbol{\sigma}\cdot\mathbf{p}$, with the additional $\boldsymbol{\tau}_z-$Pauli matrix which acts on the "valley" index and distinguishes between the Dirac points in the band structure, $\mathbf{k}=\tau\mathbf{K}=\tau(4\pi/3c,0)$ where c is the distance between the bravais lattice points and τ takes on values of ±1. The $\boldsymbol{\sigma}_i-$Pauli matrices encodes for the sublattice distinction. The s_i represents the real spin of the charge carriers. Products of matrices in the Hamiltonian are understood as tensor products between different sub-spaces. Where to clarify the usual notation, when only two operators or less are present, identity 2×2 matrices is implied for each of the omitted subspaces.

The second term in (7.1) is the intrinsic spin orbit (ISO) coupling[16], that due to the electric

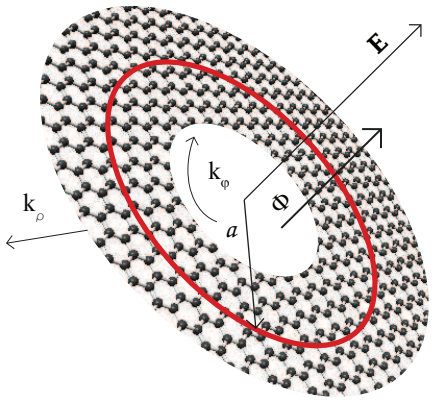

Figure 7.1: A quasi one-dimensional graphene ring in the long wavelength approach inherits all the internal symmetries the lattice structure. The Corbino ring is cut out from a graphene monolayer. The figure shows the (ρ, φ) coordinates, z being perpendicular to the plane. The average radius of the ring is a, represented by the red line. The ring is pierced by a perpendicular magnetic flux and electric field.

fields of the carbon atoms. From a tight binding point of view, this interaction comes from second neighbor hopping contribution that preserves all the symmetries of graphene. The last term in Hamiltonian (7.1) is the Rashba SO interaction which results from the action of an external electric field that breaks the spin mirror symmetry[56].
The operators tha act on spaces σ_i and s_i are dimensionless and normalized as $\sigma_i^2 = \mathbb{1}_\sigma$ and $\mathsf{s}_i^2 = \mathbb{1}_s$ (Pauli matrices), and the parameters $\Delta_{\rm SO}$ and $\lambda_{\rm R}$ have dimensions of an energy.
Since the valley operator τ_z is diagonal, the Hamiltonian can be split into two different contributions, one for each valley in $\mathbf{k}$ space, thus reducing the model to two copies of a 4×4 matrix system, instead of the full 8×8 direct product space. One then gets two separate valley Hamiltonians,

$$\begin{aligned} H_+ &= -i\hbar v_F(\boldsymbol{\sigma}_x\partial_x + \boldsymbol{\sigma}_y\partial_y) \\ &\quad +\Delta_{\rm SO}\boldsymbol{\sigma}_z\mathsf{s}_z + \lambda_{\rm R}(\boldsymbol{\sigma}_x\mathsf{s}_y - \boldsymbol{\sigma}_y\mathsf{s}_x), \qquad (7.2) \\ H_- &= -i\hbar v_F(-\boldsymbol{\sigma}_x\partial_x + \boldsymbol{\sigma}_y\partial_y) \\ &\quad -\Delta_{\rm SO}\boldsymbol{\sigma}_z\mathsf{s}_z - \lambda_{\rm R}(\boldsymbol{\sigma}_x\mathsf{s}_y + \boldsymbol{\sigma}_y\mathsf{s}_x). \qquad (7.3) \end{aligned}$$

so each valley can be treated separately.

7.1 Ring Hamiltonian and Boundary Conditions

A few important general points for the Hamiltonian in polar coordinates are worth to review, since they are frequently overlooked in the literature. The first that concerns us is the boundary conditions imposed on the wave function in a non-simply connected geometry, and the other, the form of the Hamiltonian used when a change in coordinate system is involved. We will first derive the closed ring Hamiltonian of radius a of pure kinetic energy by performing the proper coordinate mapping[51]. Then we will discuss the boundary conditions (BCs) on the ring geometry. The salient features of this model relevant to the full Corbino disk Hamiltonian will be transparent.

When using coordinates other than Cartesian, one must take care of subtleties in constructing an hermitian Hamiltonian[57, 51], whose correct form avoids spurious features in the spectrum. In the $\tau = 1$ valley, keeping only the kinetic energy and omitting the spin degree of freedom, the coordinate change applied to Eq. (7.2) results in

$$H = -i\frac{\hbar v_F}{a}(\boldsymbol{\sigma}_y \cos\varphi \, - \boldsymbol{\sigma}_x \sin\varphi \,)\partial_\varphi, \tag{7.4}$$

after removing the radial part. The difficulty comes from the observation that this Hamiltonian is not hermitian[58], since $\langle F \mid H \mid G\rangle^* \neq \langle G \mid H \mid F\rangle$, where $|\, F\rangle$ and $|\, G\rangle$ are 2-components spinors. This can be repaired by adding to Eq. (7.4) a term proportional to $i(\boldsymbol{\sigma}_y \sin\varphi \, + \tau\boldsymbol{\sigma}_x \cos\varphi)$ [51] and one is easily led to the form,

$$\begin{aligned} H_\tau = \; & - \; i\frac{\hbar v_F}{a}[(-\tau\boldsymbol{\sigma}_x \sin\varphi \, + \boldsymbol{\sigma}_y \cos\varphi \,)\partial_\varphi + \\ & - \; \tfrac{1}{2}(\boldsymbol{\sigma}_y \sin\varphi \, + \tau\boldsymbol{\sigma}_x \cos\varphi \,)]. \end{aligned} \tag{7.5}$$

Not including this term would also lead to real, but physically incorrect eigenvalues and eigenstates[58]. The reason for real eigenvalues, in spite of non-hermiticiy, follows from the operator being PT (parity and time reversal) symmetric[59].

As in [51] the derivation of the correct Hamiltonian can be pictured as follows: Le us start with the Hamiltonian $H = v_F\boldsymbol{\sigma}\cdot\mathbf{p}$, changing directly in polar coordinates, one gets

$$H \;\; = \;\; -i\hbar v_F\Big(\boldsymbol{\sigma}_\rho\partial_\rho + \rho^{-1}\boldsymbol{\sigma}_\varphi\partial_\varphi\Big), \tag{7.6}$$

fixing $\rho = a$ and taking care to properly symmetrize the product $\boldsymbol{\sigma}_\varphi \partial_\varphi$, one obtains a ring

$$H_{\text{ring}} = -i\hbar v_F a^{-1}(\boldsymbol{\sigma}_\varphi \partial_\varphi - \tfrac{1}{2}\boldsymbol{\sigma}_\rho), \tag{7.7}$$

that corresponds to the expression in (7.5) using $\boldsymbol{\sigma}_\rho = \boldsymbol{\sigma}_x \cos\varphi + \boldsymbol{\sigma}_y \sin\varphi$ and $\boldsymbol{\sigma}_\varphi = -\boldsymbol{\sigma}_x \sin\varphi + \boldsymbol{\sigma}_y \cos\varphi$. The term $\frac{1}{2}\boldsymbol{\sigma}_\rho$ in (7.7) is essential since it renders the derivative in polar coordinates covariant by introducing the connection that correctly rotates the internal degree of freedom so as to keep the pseudo spin parallel to the momentum. This form of the Hamiltonian for the angular dependence is arrived independently in the shape of the confining potential applied radially[57, 55]. The details of the confining potential will arise as effective coefficients in the form of (7.7).

The eigenstates of (7.7) are of the form

$$\psi(\varphi, z) = \frac{e^{im\varphi}}{\sqrt{2}} \begin{pmatrix} -i\kappa e^{-i\varphi} \\ 1 \end{pmatrix}, \tag{7.8}$$

with m a half positive integer for metallic rings and $\kappa = \pm 1$ describing electrons and holes respectively. The corresponding energies are $E = \frac{\kappa\hbar v_F}{a}(m - 1/2)$. It is easy to verify that $\langle\boldsymbol{\sigma}\rangle = \kappa(-\sin\varphi, \cos\varphi) = \kappa\mathbf{k}/|\mathbf{k}|$, as can be derived in Cartesian coordinates. In spite of the fact that pseudo-spin follows the momentum, it is endowed with proper angular momentum[60]. This can be verified by noting that the Hamiltonian of (7.7) does not commute with the orbital angular momentum alone $L_z = -i\hbar\partial_\varphi$ but with the combination $J_z = L_z + \frac{1}{2}\hbar\sigma_z$ (and with $(L_z \mathbf{u}_z + \frac{1}{2}\hbar\boldsymbol{\sigma})^2$. Note that if L_z does not commute with the Hamiltonian, there is a torque on the orbital momentum. This torque is compensated by a torque on the pseudo spin angular moment so that the total J_z is conserved. Thus, with the pseudo spin there is associated "lattice spin" presumably from the rotation the electron sees of the A-B bond. We will see in the next section, how this extra angular momentum combines with the regular electron spin to generate a total conserved angular momentum.

The wave function nevertheless, preserves spin-like properties. One can verify that the the ring eigenfunctions are anti-periodic, thus $\psi(\varphi + 2\pi) = -\psi(\varphi)$, a property which finds its origin in the effect of the 2π rotation on the connection $\frac{1}{2}\sigma_\rho$. The factor $\frac{1}{2}$ corresponds to a Berry phase, discussed as a very crucial feature of graphene (e.g. by Katsnelson [3], Guinea et al [14]) and of carbon nanotubes (e.g. in Ref. [61]). We will reemphasize these points in our derivation in the following sections which several previous references have overlooked (see

references [58, 15, 62, 51]).

7.2 Closing the wave function on a graphene ring

In this section, we are interested in discussing graphene rings described with the effective Dirac theory in the vicinity of the K points with appropriate boundary conditions. Recalling that according to Bloch's theorem, the wave function $\psi(\mathbf{r}) = u_{\mathbf{k}}(\mathbf{r})\mathbf{e}^{\mathbf{ik}\cdot\mathbf{r}}$ should exhibit the ring periodicity, while the Bloch amplitude $u_{\mathbf{k}}(\mathbf{r})$ has the lattice periodicity. The periodic boundary conditions imposed on the Bloch wave function do not necessarily imply periodic boundary conditions for the eigenfunctions of the effective theory [16]. Indeed, $\mathbf{k}$ is measured from the Brillouin zone center (Γ point). The effective theory is related to the wave vector $\mathbf{q} = \mathbf{p}/\hbar$ in the neighborhood of the Dirac points through $\mathbf{k} = \mathbf{K}_D + \mathbf{q}$.
Generalizing the boundary conditions for the case of a ring with linear dispersion (see previous section) we introduce a twist phase θ_0 in the closing of the wave function

$$\psi(\varphi + 2\pi) = e^{-i\theta_0}\psi(\varphi). \tag{7.9}$$

The eigenstates are now of the form

$$\psi(\varphi) = e^{i(m-\theta_0/2\pi)\varphi}\begin{pmatrix} Ae^{-i\varphi} \\ B \end{pmatrix}, \tag{7.10}$$

with m an integer, with corresponding eigenvalues

$$E = \pm\frac{\hbar v_F}{a}\left|m - \tfrac{\theta_0}{2\pi}\right|, \tag{7.11}$$

where $\kappa = \pm 1$ refers to particles (conduction band) and holes (valence band). As we discussed in the previous section, in the case of a graphene ring, antiperiodic BCs (ABC) should be chosen[16, 14]; this means $\theta_0 = \pi$ for graphene in a Corbino geometry, but for different boundary conditions, such as those that occur in carbon nanotubes with arbitrary chiralities, can also be described. Note that the twist phase plays the same role as a magnetic flux through the ring, that can modify its conducting properties by manipulating the gap at the Dirac point.
Let us extend the boundary conditions discussion for the proposed ring. The discussion on graphene nano ribbons have been addressed in detail[63]. For the approximation addressed here,

the zig-zag nano-ribbons are the closest relative, since it has been shown[17] that a generically cut honeycomb lattice has approximately zig-zag boundary conditions to a high accuracy. For graphene ribbons with zigzag edges there is the concern that longitudinal and transverse states are coupled[63] and slicing the graphene band using the boundary conditions is not warranted for small ribbon widths $N \sim 1$ (number of transverse lattice sites). Nevertheless, for wide ribbons ($N \gg 1$) this approximation becomes increasingly good as can be judged from the relation coupling the longitudinal k and transverse p modes $\sin \mathrm{p}N + w \cos(\mathrm{k}/2) \sin \mathrm{p}(N+1) = 0$ where the wavectors in units of the magnitude of the primitive translation vectors of the lattice. When $N \gg 1$ then $\mathrm{p} = m\pi/N$ independent of k. One final concern is the existence of one localized state that for nano ribbons for a critical value of the longitudinal wavevector, nevertheless, the restriction also disappears in the limit $N \gg 1$ in which our continuum approximation is based. In the next section we will discuss the possible coupling of the transverse modes due to the spin-orbit interaction.

The vicinity to the Dirac points is an important issue here, since the linear range of the spectrum is subject to the lattice parameter and the radius of the ring. The estimated limiting value of the momentum ignoring lattice effects[64] is $k_l \approx 0.25\mathrm{nm}^{-1}$. The carrier limiting energy at this point is $E_l = \hbar v_F k_l$. Equating this value with (7.11) we obtain the maximum number of states, hence,

$$\left| m - \tfrac{\theta_0}{2\pi} \right| \lesssim k_l a. \tag{7.12}$$

As a reference estimation based on an analogous ring already present in nature (in fact a carbon nanotube section has a kinetic term of the same form as the Corbino); a single wall carbon nanotube has radius that goes from 10 nm to 100 nm, this gives order of magnitudes from $m \sim 2$ to $m \sim 25$ that varies depending whether it is an armchair or zigzag tube. For a carbon nanotube with a smaller radius than 4 nm, the allowed states will be outside the linear region establishing a threshold for the values of a in the long wavelength approach.

7.3 Spin-Orbit coupling

Having set up the correct Hamiltonian and boundary conditions to describe a graphene ring, we can incorporate SO interactions in the ring geometry to obtain the equivalent of Eqs. (7.2) and (7.3). The spectrum becomes independent of the valley index τ, so we will only deal with

$\tau = +1$ in polar coordinates:

$$\begin{aligned} H_+ &= -i\hbar v_F a^{-1}(\boldsymbol{\sigma}_\varphi \partial_\varphi - \tfrac{1}{2}\boldsymbol{\sigma}_\rho) \\ &\quad + \Delta_{\rm SO}\boldsymbol{\sigma}_z \mathsf{s}_z + \lambda_{\rm R}(\boldsymbol{\sigma}_\rho \mathsf{s}_\varphi - \boldsymbol{\sigma}_\varphi \mathsf{s}_\rho). \end{aligned} \tag{7.13}$$

For the ISO only case we assume a 4−component vector to represent the electronic states, incorporating electron spin, $\Psi = e^{im\varphi}\left(A_\uparrow^{\kappa,\delta}e^{-i\varphi}, A_\downarrow^{\kappa,\delta}, B_\uparrow^{\kappa,\delta}, B_\downarrow^{\kappa,\delta}e^{i\varphi}\right)^T$, where $A_{\uparrow,\downarrow}^{\kappa,\delta}$ ($B_{\uparrow,\downarrow}^{\kappa,\delta}$) is the wavevector amplitude on sublattice A (B) with spin $\delta = \uparrow\downarrow$. The ansatz for the spinor is constructed in order to account for the conservation of the total angular momentum. All components carry the same angular momentum J_z, adding in units of $\hbar$ a purely orbital contribution (respectively $m-1$, m, m, and $m+1$ for the four compoents), a pseudo-spin or lattice contribution (resp. $+\frac{1}{2}$, $+\frac{1}{2}$, $-\frac{1}{2}$ and $-\frac{1}{2}$), and the spin contribution (resp. $+\frac{1}{2}$, $-\frac{1}{2}$, $+\frac{1}{2}$ and $-\frac{1}{2}$).

The eigenenergies, assuming these wave functions (with constant amplitudes A an B), are

$$E_{m,\Delta}^{\kappa,\delta} = \kappa\sqrt{\Delta_{\rm SO}^2 + \epsilon^2(m-\delta/2)^2}, \tag{7.14}$$

where $\kappa = \pm 1$ is the particle-hole index and $\delta = \pm 1$ the SO index, and $\epsilon = \frac{\hbar v_F}{a}$. $\kappa\epsilon|(m-\delta/2)|$ corresponds to the electron energies in the absence of ISO. On the other hand when only the Rashba interaction is present the energy is given by

$$E_{m,\lambda_{\rm R}}^{\kappa,\delta} = \frac{\kappa}{2}\sqrt{\epsilon^2(1+4m^2) + 8\lambda_{\rm R}^2 - 4\delta\sqrt{(m^2\epsilon^2+\lambda_{\rm R}^2)(\epsilon^2+4\lambda_{\rm R}^2)}}, \tag{7.15}$$

which has the correct zero SO coupling limit. These energies correspond to the angular wavectors satisfying the closed ring boundary conditions. The spectrum is shown in Fig. 7.2. We assume that the transverse mode is in the basis state using again as reference the transverse modes for the graphene zigzag ribbons. The spinor wave functions for the ribbons depend on both longitudinal and transverse indices. Choosing the basis state in the $N \gg 1$ limit permits writing an explicit expression for the wave functions and assess the coupling of the free transverse modes in the presence of the SO couplings. If the coupling is large compared to the transverse level separation, it must be contemplated in our analysis[65]. Writing the ribbon wave functions in the basis above, we computed that in the $N \gg 1$ limit the coupling between transverse modes is negligible. So that the single transverse mode approximation is warranted.

Although the possible wave vectors take on discrete half integer values, they will trace a continuous change when a gauge field is applied. Close to the point of closest approach between the valence and conduction bands. For the ISO coupling these points are around $m = \pm 1/2$ and the expansion takes the form

$$E^{\kappa,\delta}_{m,\Delta} = \kappa|\Delta_{\rm SO}| + \frac{\kappa\epsilon^2}{2|\Delta_{\rm SO}|}(m \pm 1/2)^2 + O\left((m \pm 1/2)^4\right), \tag{7.16}$$

while for the Rashba coupling the behavior is

$$E^{\kappa,\delta}_{m,\lambda_{\rm R}} = \frac{\kappa|m \pm 1/2|}{\sqrt{2}(\epsilon^2 + 4\lambda_{\rm R}^2)} + O\left((m \pm 1/2)^2\right). \tag{7.17}$$

The intrinsic spin-orbit term will open a gap in the vicinity of ($m = \pm 1/2$) which is simply $2\Delta_{\rm SO}$ where the electrons exhibit an effective mass of $m^*_{\rm ISO} = \Delta^2_{\rm SO}/v_F^2$ which is small, both because v_F is large and $\Delta_{\rm SO}$ is in the range of meV for graphene. For the Rashba coupling there is no gap at $m = \pm 1/2$ but we will see a spin dependent gap opens continuously as the magnetic field is applied. Note also that this is a gap between spin-orbit up states. The gap between spin-orbit down states is given by $\sqrt{\epsilon^2 + 4\lambda_{\rm R}^2} + 2\lambda_{\rm R}$. One can define an effective mass of the spin down states as $m^*_\downarrow = \kappa\lambda_{\rm R}\hbar^2/[2\epsilon^2(2\lambda_{\rm R} + \sqrt{\epsilon^2 + 4\lambda_{\rm R}^2})]$.
The limit in which the SO coupling goes to zero is singular, since both gaps close and the dispersion becomes linear as $\kappa\hbar v_F q_\varphi$. This limit highlights another feature of the Rashba spectrum; in the vicinity of the Dirac points K, and K', the electron behaves as a hole (has negative mass) in the conduction band and has negative charge (positive mass). From the expression above $m^*_\uparrow = -m^*_\downarrow$ at the Dirac Point.
The typical values used for intrinsic coupling are estimated in Ref. [56] using a microscopic tight-binding model with atomic spin orbit interaction. The Rasha interaction comes from the atomic spin orbit and Stark interactions and the intrinsic from the mixing between σ and π bands due to atomic spin orbit interaction. The coupling constants are given by the expressions,

$$\begin{aligned} \Delta_{\rm SO} &= \frac{|s|\xi^2}{18(sp\sigma)^2}, \\ \lambda_{\rm R} &= \frac{eEz_0\xi}{3(sp\sigma)}, \end{aligned}$$

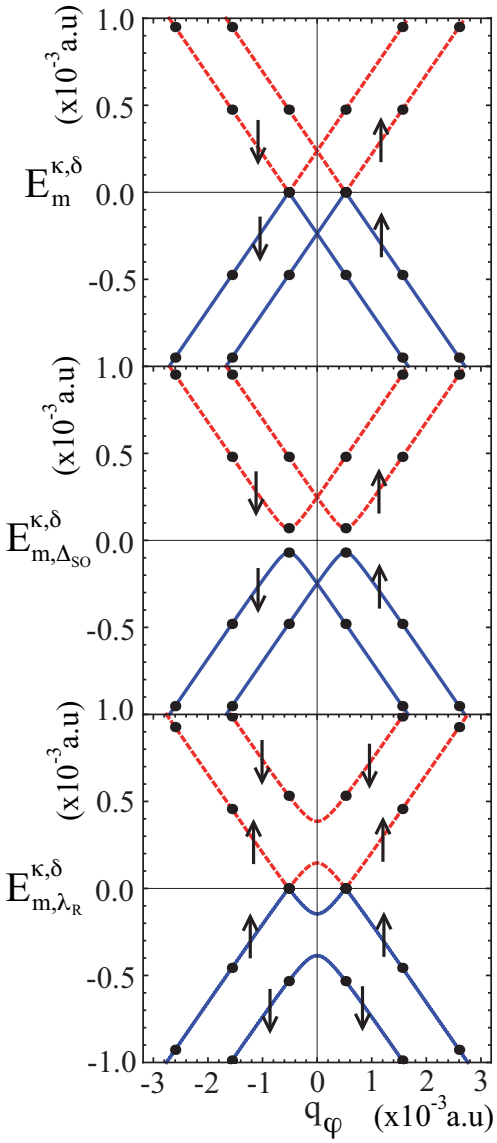

Figure 7.2: Dispersion relations for metallic rings for the free (top panel) and both SO interactions (intrinsic middle and Rashba bottom, panels). The ISO has been drawn for $\Delta_{\rm SO} = 0.25$, and opens a gap of size $2\Delta_{\rm SO}$ with separate branches for each spin label. The Rashba interaction is depicted for $\lambda_{\rm R} = 0.4$, the allowed values of m are indicated by the full dots. Note the spin asymmetry introduced by the Rashba coupling, that will have striking consequences for the charge and spin persistent currents.

where $|s|$ and $(sp\sigma)$ are hopping parameters in the tight-binding model, $s = -8.868$ eV and $(sp\sigma) = 5.580$ eV, $\xi = 6$ meV is the atomic SO strength of carbon, and $z_0 \sim 3 \times a_B$ (a_B is the Bohr radius), is proportional to its atomic size. $\lambda_{\rm R}$ is proportional to the electric field, $E \approx 50$ V/300 nm, perpendicular to the graphene sheet. This gives values for the SO parameters $\lambda_{\rm R} \approx 0.1$ K and $\Delta_{\rm SO} \approx 0.01$ K.

The split bands open a gap symmetrically between the δ states when $\Delta_{\rm SO} = 0$. If $\Delta_{\rm SO} \neq 0$ the contributions for each gap are different [66, 67]. In this parametrization the blue and the red curves (dashed and continuous respectively) represent the levels in the quantization axis of the RSO interaction, i.e. in the SO basis[48].

As we will see below, the velocity operator merits a non-trivial treatment in the context of graphene. For this reason we will derive the eigenfunctions for both SO couplings to compute the charge and spin persistent currents using the velocity operator, and compare it with the linear response relation. For the ISO only we have the wavefunctions

$$\Psi^{\kappa,\delta}_{m,\Delta}(\varphi) \;=\; \frac{e^{im\varphi}}{2|E^{\kappa,\delta}_{m,\Delta}|}\begin{pmatrix} \delta_{\delta,+}[\epsilon(m-\frac{1}{2})-i(\Delta_{\rm SO}+E^{\kappa,\delta}_{m,\Delta})]e^{-i\varphi} \\ \delta_{\delta,-}[\epsilon(m+\frac{1}{2})+i(\Delta_{\rm SO}-E^{\kappa,\delta}_{m,\Delta})] \\ \delta_{\delta,+}[\epsilon(m-\frac{1}{2})-i(\Delta_{\rm SO}-E^{\kappa,\delta}_{m,\Delta})] \\ \delta_{\delta,+}[\epsilon(m+\frac{1}{2})+i(\Delta_{\rm SO}+E^{\kappa,\delta}_{m,\Delta})]e^{i\varphi} \end{pmatrix}, \tag{7.18}$$

labelled by κ and δ as $\Psi^{\kappa,\delta}_{m,\Delta}$. The polarization of this state is given by the expectation value of the operator $(\hbar/2)\mathbb{1}_\sigma \mathbf{s}$,

$$\langle \mathsf{s}_z \rangle = \frac{\hbar}{2}(\Psi^{\kappa,\delta}_{m,\Delta}(\varphi))^\dagger \mathbb{1}_\sigma \mathsf{s}_z \Psi^{\kappa,\delta}_{m,\Delta}(\varphi). \tag{7.19}$$

and all the states are polarized perpendicular to the Corbino disk i.e. the $\mathbf{z}$ direction. This is also the direction of the effective magnetic field implied by the rewriting of the ISO term as $(\Delta_{\rm SO}\boldsymbol{\sigma})\cdot\mathbf{s} = (\Delta_{\rm SO}\sigma_z)\mathsf{s}_z$, a field that aligns the spins in opposite direction on different sublattices, in the z direction. The result is zero global spin-magnetization while each sub lattice is spin-magnetized in opposite directions. This is in accordance with the fact that the intrinsic SO interaction operates as a local magnetic field in each sublattice with opposite sign, and thus not breaking of time reversal symmetry.

The pseudo spin polarizations are computed in an analogous fashion

$$\begin{aligned}\langle\boldsymbol{\sigma}\rangle &= \frac{\hbar}{2}(\Psi^{\kappa,\delta}_{m,\Delta}(\varphi))^{\dagger}\boldsymbol{\sigma}\mathbb{1}_s\Psi^{\kappa,\delta}_{m,\Delta}(\varphi),\\ &= \frac{\kappa\hbar}{2}\frac{\delta\hat{\boldsymbol{z}}\Delta_{SO}+(m-\delta/2)\epsilon\hat{\boldsymbol{\varphi}}}{E^{\kappa,\delta}_{m,\Delta}},\end{aligned} \tag{7.20}$$

where we note the ordering go the matrix direct product. One sees both orbital and spin-orbit contributions, so the pseudo spin does not simply follow the electron momentum.
The Rashba eigenfunctions are

$$\Psi^{\kappa,\delta}_{m,\lambda_{\rm R}}(\varphi) = \frac{e^{im\varphi}}{\sqrt{\Lambda}}\begin{pmatrix}\frac{-2iE^{\kappa,\delta}_{m,\lambda_{\rm R}}(m\epsilon^2+2\lambda_{\rm R}^2+\delta\Gamma_m)}{(4m^2-1)\epsilon^2\lambda_{\rm R}}e^{-i\varphi}\\ \frac{-2iE^{\kappa,\delta}_{m,\lambda_{\rm R}}}{\epsilon(2m+1)}\\ \frac{m\epsilon^2-2\lambda^2+\delta\Gamma_m}{\epsilon\lambda_{\rm R}(2m+1)}\\ e^{i\varphi}\end{pmatrix}, \tag{7.21}$$

where $\Gamma_m=\sqrt{(m^2\epsilon^2+\lambda_{\rm R}^2)(\epsilon^2+4\lambda_{\rm R}^2)}$ and $\Lambda=4\Gamma_m\left(\Gamma_m-\delta(2\lambda_{\rm R}^2-m\epsilon^2)\right)/(2m+1)^2\epsilon^2\lambda_{\rm R}^2$. The polarization of the Rashba eigenvectors is given by

$$\begin{aligned}\langle\mathbf{s}\rangle &= \frac{\hbar}{2}(\Psi^{\kappa,\delta}_{m,\lambda_{\rm R}}(\varphi))^{\dagger}\mathbb{1}_{\sigma}\mathbf{s}\Psi^{\kappa,\delta}_{m,\lambda_{\rm R}}(\varphi),\\ &= \delta\left(\frac{\hbar}{2}\right)\frac{m\epsilon(2\lambda_{\rm R}\hat{\boldsymbol{\rho}}+\epsilon\hat{\mathbf{z}})}{\Gamma_m},\end{aligned} \tag{7.22}$$

where two contributions are evident, the polarization points outward in the radial direction and has a component due to the orbital rotation of the electrons.
Following previous expressions the Rashba pseudo-spin polarizations are

$$\begin{aligned}\langle\boldsymbol{\sigma}\rangle &= \frac{\hbar}{2}(\Psi^{\kappa,\delta}_{m,\lambda_{\rm R}}(\varphi))^{\dagger}\boldsymbol{\sigma}\mathbb{1}_s\Psi^{\kappa,\delta}_{m,\lambda_{\rm R}}(\varphi),\\ &= \frac{\hbar}{2}\frac{\delta m\epsilon E^{\kappa,\delta}_{m,\lambda_{\rm R}}(\delta m\gamma+\Gamma_m)\hat{\boldsymbol{\varphi}}}{(m-1/2)(\delta m\epsilon^2\Gamma_m+m^2\epsilon^2\gamma+\lambda_{\rm R}^2(\gamma-2\delta\Gamma_m))},\end{aligned} \tag{7.23}$$

where $\gamma=\epsilon^2+4\lambda_{\rm R}^2$.

7.4 Charge persistent currents

Persistent equilibrium currents are a direct probe of energy spectrum of the system in the vicinity of the Fermi energy. Although such currents are typically small and are detected by the magnetic moment they produce[68], recent experiments, where many rings form dense arrays on a cantilever, boost the magnetic signal allowing both measurement of the current signal and the use of the set up as a sensitive magnetometer. The Corbino disk geometry can be easily built with high precision by using new techniques[69] manipulating nano-particles as cutters and hydrogenating the open bonds.
The spectrum of the system is modified by a field flux perpendicular to the Corbino disk as follows

$$E^{\kappa,s}_{m,\Delta}(\Phi) = \kappa\sqrt{\Delta^2_{\rm SO}+\epsilon^2(m-\delta/2+\Phi/\Phi_0)^2}, \tag{7.24}$$

$$E^{\kappa,\delta}_{m,\lambda_{\rm R}}(\Phi) = \frac{\kappa}{2}\sqrt{8\lambda^2_{\rm R}+\epsilon^2\left(4(m+\Phi/\Phi_0)^2+1\right)-4\delta\sqrt{\left(4\lambda^2_{\rm R}+\epsilon^2\right)\left(\lambda^2_{\rm R}+\epsilon^2(m+\Phi/\Phi_0)^2\right)}}, \tag{7.25}$$

where the Zeeman coupling has been neglected at small enough fields. The addition of a magnetic field, in the form of a $U(1)$ minimal coupling with flux Φ threading the ring, breaks time reversal symmetry allowing for persistent charge currents[6]. In the case of a ring of constant radius threaded by a perpendicular magnetic flux, the angular component of the gauge vector $A_\varphi = \Phi/2\pi a$ may be eliminated via a gauge transformation $A'_\varphi = A_\varphi + a^{-1}\partial_\varphi\chi = 0$, $\Psi'(\varphi) = \Psi(\varphi)e^{ie\chi/\hbar}$ at the expense of modifying the BCs on the ring to

$$\Psi'(\varphi+2\pi) = e^{-i\theta_0}e^{-2i\pi\Phi/\Phi_0}\Psi'(\varphi), \tag{7.26}$$

where Φ_0 is the normal quantum of magnetic flux (h/e). As mentioned before, the twist in the BCs and the field accomplish the same effect, so one can use them interchangeably while satisfying the relation

$$E^{\kappa,\delta}_{m,\Phi}(\theta_0) = E^{\kappa,\delta}_{m,0}(\theta_0+2\pi\Phi/\Phi_0), \tag{7.27}$$

hence $m \to m-\theta_0/2\pi+\Phi/\Phi_0$, as discussed in Eq.(7.11). The energy dispersion for the graphene ring is illustrated in Fig. 7.3 (left panel), where the different colors (online) (see caption) refer to the conduction band ($\kappa=+1$, dashed line) and valence band ($\kappa=-1$, full line). As expected, the energy levels display a periodic variation with the magnetic flux (right panel in the figure). The charge persistent current in the ground state can be derived using the linear response

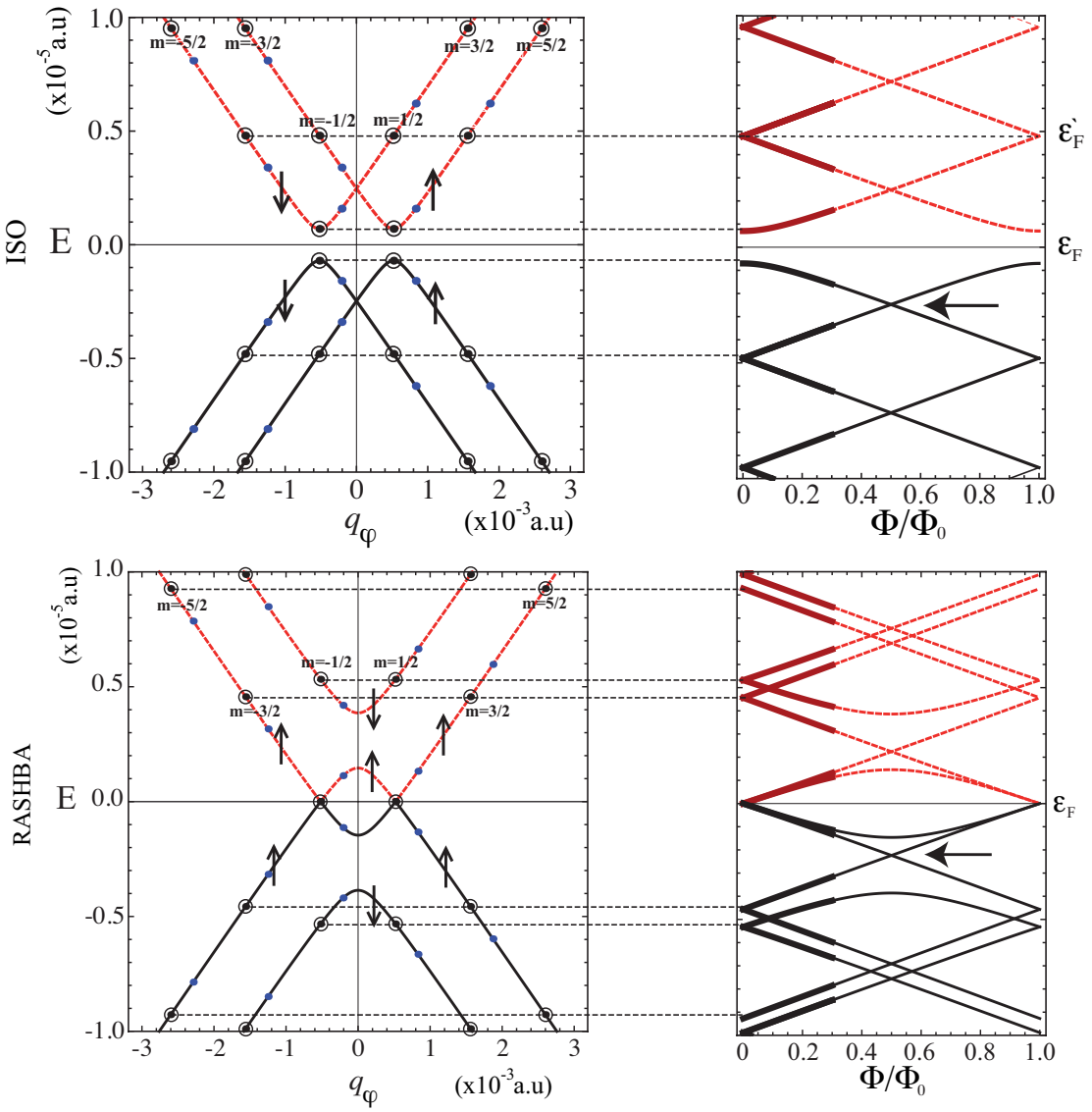

Figure 7.3: The energy dispersion for the ISO (top panel with $\Delta_{\rm SO} = 7\times10^{-7}$ a.u. see ref.([56])) and Rashba coupling (bottom panel with $\lambda_{\rm R} = 1.2 \times 10^{-6}$a.u.) as a function of wave-vector q_φ (for continuum range of values; solid and dashed lines). The circled dots represent the allowed values of the energies on the ring at zero magnetic flux. The uncirled dots (blue online) represent the shift of the allowed energies due to a finite flux. On the right panel, the energy bands are plotted against Φ/Φ_0. On this panel the trajectory of the allowed values of the energy is followed as a function of the field. The solid lines represent the valence bands and the dashed the conduction bands. The Fermi energy is assumed to be zero, except for the Rashba where a finite value for the Fermi energy is also illustrated. The bold arrow on the right panels indicate level crossing discussed in the text.

definition $J_Q = -\sum'_{m,\kappa,\delta} \frac{\partial E}{\partial \Phi}$, where the primed sum refers to all occupied states only. Since the current is periodic in Φ/Φ_0 with a period of 1, we can restrict the discussion to the window $0 \leq \Phi < \Phi_0$ where the occupied states are in the valence band $\kappa = -1$, since the Fermi level is chosen at the zero of energy. We will first discuss the simple ISO coupling. The analytical expression is given by

$$J^{\kappa}_{Q,\Delta} = -\frac{\epsilon^2 \kappa}{\Phi_0} \sum_{m,\delta}{}' \frac{(m - \delta/2 + \Phi/\Phi_0)}{E^{\kappa,\delta}_{m,\Delta_{\rm SO}}(\Phi)}. \tag{7.28}$$

In Fig.7.3, on the left panel, the spin-orbit branches of the spectrum labeled with their spin quantum number have been depicted. The encircled dots are the allowed energy values, due to quantization on the ring, at zero magnetic field. When the field is turned on, these dots are displaced (no longer encircled) on the energy curve.

On the right panel we depict the trajectory of these dots as the magnetic field is increased for both the filled (full lines in figure) and unfilled (dashed lines) states. The negative derivative of the curves on the right panel added over the occupied states (both spin quantum numbers) is the net charge persistent current. For the range of energies shown, the only net contribution is from the levels closest and below the Fermi level. The lower levels have currents that tend to compensate in pairs. Following the curve on the right, below the Fermi energy and from zero field, the current first increases linearly and then bends over to reach a maximum value before two levels cross (crossing indicated by arrow on the right panel of Fig.7.3). At that point, one follows the level closest to the Fermi energy (from below), the current changes sign and increases crossing the zero current level, whereupon the whole process repeats periodically. Such behavior is shown in Fig.7.4 top panel. Changing the Fermi level can change the scenario qualitatively. For example adjusting the Fermi level to ε'_F (see Fig.7.3), the currents would follow a square wave form, alternating between constant current blocks of opposite signs.

For the Rashba coupling, represented in the bottom panels in Fig.7.3, the current is derived in a similar way, but now there is a striking asymmetry between spin branches. The analytical form for the charge current is

$$J^{\kappa}_{Q,\lambda_{\rm R}} = -\frac{\epsilon^2 \kappa}{\Phi_0} \sum_{m,\delta}{}' \frac{\left(2 - \frac{\delta(\epsilon^2 + 4\lambda_{\rm R}^2)}{\sqrt{(\epsilon^2+4\lambda_{\rm R}^2)(\lambda_{\rm R}^2 + \epsilon^2(m+\Phi/\Phi_0)^2)}}\right)(m + \Phi/\Phi_0)}{E^{\kappa,\delta}_{m,\lambda_{\rm R}}(\Phi)}. \tag{7.29}$$

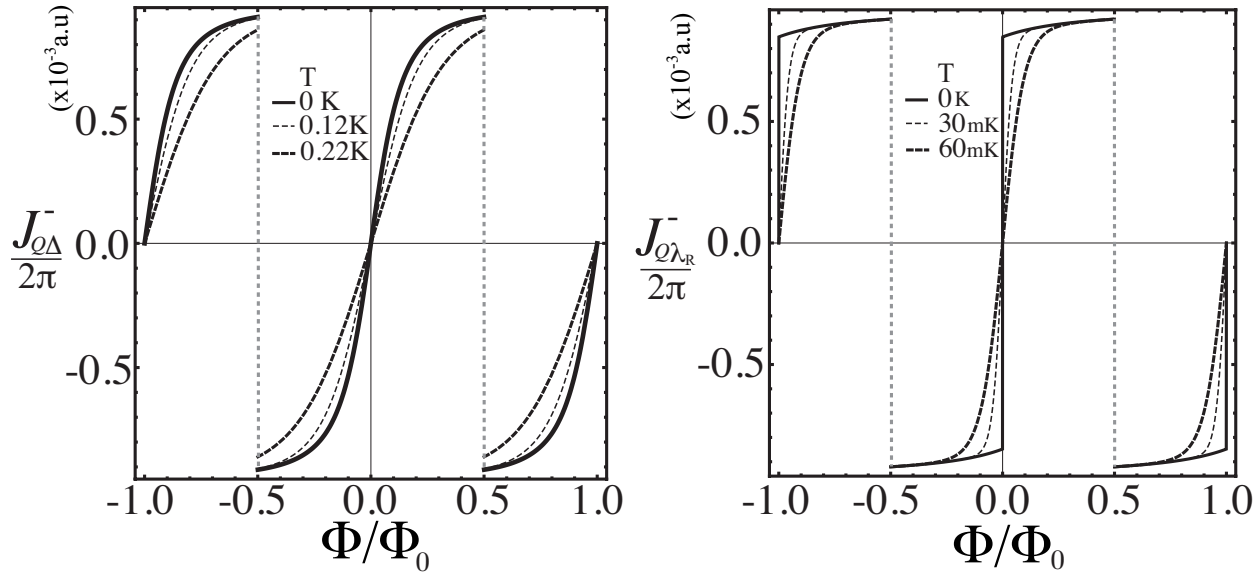

Figure 7.4: The equilibrium charge currents for both ISO and Rashba interactions. The ring is considered to have a radius of $a = 20nm$, $\Delta_{\rm SO} = 0.4$ and $\lambda_{\rm R} = 0.25$. The variations of the current are given by the slopes of the Figure 7.3. At each flux region, the states up to ε_F are taken into account.

The spin branch closest to the Fermi energy is non monotonous, making for two different contributions to the charge current for the up spin contribution. Note also that we have taken into account the current coming from the spin down branch which does not have the same effective mass as the corresponding branch of the opposite spin. The results are depicted in Fig.7.4 bottom panel. The structure of the spectrum being asymmetric between spin branches makes for the possibility of net spin currents as we will see below. The charge persistent current can be manipulated with $\lambda_{\rm R}$ since the Rashba parameter can be tuned by a field perpendicular to the plane of the ring. In contrast, the intrinsic SO cannot be easily tuned by applying external fields. Nevertheless, it has been established experimentally[70] that light covering of graphene with covalently bonded hydrogen atoms modifies the carbon hybridization and can enhance the intrinsic spin-orbit strength by three orders of magnitude[70]. Regulating this covering may then be a tool to manipulate charge currents.

One can contemplate the effect of temperature on the robustness of persistent charge currents by considering the occupation of the energy levels. The Fermi function has then to be factored

into the computation of the currents

$$J^{\kappa}_{Q,\lambda_{\rm R}}(T) = -\sum_{m,\delta} \frac{\partial E^{\kappa,\delta}_{m,\lambda_{\rm R}}(\Phi)}{\partial \Phi} f(E^{\kappa,\delta}_{m,\lambda_{\rm R}}, \varepsilon_F, T), \tag{7.30}$$

where $f(E, \varepsilon_F, T) = (1 + \exp{(E - \varepsilon_F)/k_B T})^{-1}$ is the Fermi occupation function for the case of the Rashba coupling. There is no need now to restrict the energy levels contemplated since the filling is determined by the Fermi distribution.

Figure 7.4, shows the effect of a temperature energy scale of the order of the SO strength for both intrinsic and Rashba couplings. The deep levels will be fully occupied while the shallow levels (close to the Fermi energy) will have a temperature dependent occupancy. Occupation depletion affects mostly the current contributions from levels within $k_B T$ of the Fermi level. This typically happens in the vicinity of the integer values of the normalized flux Φ/Φ_0, but at half integer fluxes the contributing levels dig into the Fermi sea where carrier depletion is less pronounced and current discontinuities tend to be protected from temperature effects. From Fig.7.3 one can estimate the depth in energy of the crossing to be $\sim 3 \times 10^{-4}$ a.u which amounts to a temperature equivalent of $\sim$1 K before degradation of spin currents is observed at half integer fluxes. This is an important feature of the linear dispersions in graphene, and in enhanced SO coupling scenarios could be of applicability for magnetometer devices at relatively higher temperatures.

7.5 Equilibrium spin currents

We now contemplate spin equilibrium currents. In the absence of a direct linear response definition one can obtain them from the charge currents by distinguishing the velocities of different spin branches. We define a spin equilibrium current as

$$J_{\rm S} = J_Q(\delta = -1) - J_Q(\delta = 1), \tag{7.31}$$

where one weighs the asymmetry in velocities of the different occupied spin branches. As we mentioned in the previous section there is no spin asymmetry both for the free case and for the ISO, so no spin current can result in this case, i.e. both spin branches contribute charge current with the same amplitude so they cancel in the above expression. With the Rashba coupling, the inversion symmetry is broken inside the plane and the spin branches are asymmetrical for

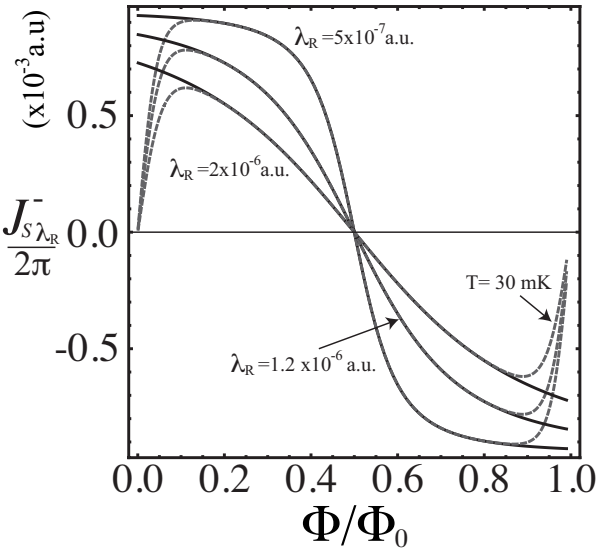

Figure 7.5: Spin current for the Rashba SO coupling indicated by the legends as a function of the magnetic field, as derived form the charge currents distinguished by spin components. The large spin currents at small fields are due to dominant charge currents for a single spin orientation. Temperature affect currents at the integer values of flux, while toward haslf integer values currents are protected.

a range of q_φ values.

The peculiar separation of the spin branches makes for velocity differences of the two spin projections and a spin current ensues as shown in Fig.7.5. The figure shows a large spin current for small fluxes that can be traced back to the large charge currents coming from a single spin branch in Figure 7.3. Toward half integer flux quantum's the opposite spin charge current increases until it cancels out the spin current completely. Beyond half integer flux the spin current is reversed in sign and at zero temperature there is a discontinuity approaching integer fluxes. As discussed for charge currents, the spin currents are also most susceptible to thermal depletion of carriers at integer fluxes, while toward half integer fluxes these are protected.

A striking feature, that survives temperature effects, is that the spin currents increase as one lowers $\lambda_{\rm R}$. The Rashba coupling breaks inversion symmetry in the plane even for small $\lambda_{\rm R}$. The symmetry breaking determines the spin labeling of the energy branches that take part in the spin current. It is only for $\lambda_{\rm R} = 0$ that the free Hamiltonian symmetry is re-established and the spin currents are destroyed. A combination of the described symmetry effect and the thermal shielding from deep levels make for these effects observable experimentally.

7.6 Velocity operators for graphene

As discussed in section III, there are two ways to compute the effect of the magnetic field: either putting the description in the Hamiltonian as a gauge vector or performing a gauge transformation and passing all field information to the wave function. For SU(2) gauge theory applied to the present case, this process cannot be done directly because of the lack of gauge symmetry[11]. We have solved the problem fully for the "gauge fields" in the Hamiltonian and determined the eingenfunctions. Such eigenfunctions contain the full information of the state, and the velocities as a function of the magnetic field can be derived by using the canonical equations $v_\varphi = a\dot{\varphi} = \frac{a}{i\hbar}[\varphi, H]$ where the commutator takes the value $[\varphi, H] = i\hbar v_F a^{-1}\boldsymbol{\sigma}_\varphi \mathbb{1}_s$ and compute

$$J_Q = \frac{ev_F}{a}\sum_{m,\delta}{}' \left(\Psi_m^{\kappa,\delta}(\varphi,\Phi)\right)^\dagger \boldsymbol{\sigma}_\varphi \mathbb{1}_s \Psi_m^{\kappa,\delta}(\varphi,\Phi). \tag{7.32}$$

Taking the ISO wave functions and substituting $m \to m + \Phi/\Phi_0$ we determine the appropriate $\Psi_m^{\kappa,\delta}(\varphi,\Phi)$. We could also, leave the wave function untouched and include a U(1) gauge vector in the momentum operator. Let us explicitly write out an expectation value

$$\begin{aligned}
&J_{Q,\Delta}^{+,+} = -ev_F \left(\Psi_{m,\Delta}^{+,+}(\varphi,\Phi)\right)^\dagger \sigma_\varphi \mathbb{1}_s \Psi_{m,\Delta}^{+,+}(\varphi,\Phi) = \\
&\frac{1}{4|E_{m,\Delta}^{+,+}|^2}\begin{pmatrix} \left[\epsilon(m-\frac{1}{2}+\frac{\Phi}{\Phi_0}) + i(\Delta_{\rm SO}+E_{m,\Delta}^{+,+})\right]e^{i\varphi} \\ 0 \\ \epsilon(m-\frac{1}{2}+\frac{\Phi}{\Phi_0}) + i(\Delta_{\rm SO}-E_{m,\Delta}^{+,+}) \\ 0 \end{pmatrix}^T \begin{pmatrix} 0 & -ie^{-i\varphi} \\ ie^{i\varphi} & 0 \end{pmatrix} \otimes \\
&\begin{pmatrix} 1 & 0 \\ 0 & 1 \end{pmatrix} \begin{pmatrix} \left[\epsilon(m-\frac{1}{2}+\frac{\Phi}{\Phi_0}) - i(\Delta_{\rm SO}+E_{m,\Delta}^{+,+})\right]e^{-i\varphi} \\ 0 \\ \epsilon(m-\frac{1}{2}+\frac{\Phi}{\Phi_0}) - i(\Delta_{\rm SO}-E_{m,\Delta}^{+,+}) \\ 0 \end{pmatrix} \\
&= -\frac{\epsilon^2}{\Phi_0}\frac{(m-1/2+\Phi/\Phi_0)}{E_{m,\Delta}^{+,+}},
\end{aligned} \tag{7.33}$$

which coincides with the expression of (7.28). With either of the two procedures one retrieves the same charge current of (7.28). This is a simple but interesting connection between linear

response relations used to compute the current and a canonical exact calculation in principle. Note also that this expectation value corresponds to the procedure that eliminates Zitterbewegung from the Dirac definition of the velocity operator $\langle c\boldsymbol{\alpha}\rangle$ where $\boldsymbol{\alpha} = \sigma_\varphi \mathbb{1}_s$ and $c = v_F$. One can also obtain the linear response result using the group velocity operator applied to the free wave functions[71], where the group velocity operator is then

$$\hat{J}^{\kappa,\delta}_{Q,\Delta} = \frac{v_F^2 \hat{\mathbf{p}}}{\kappa\sqrt{\Delta_{\mathrm{SO}}^2 + \epsilon^2(m - \delta/2)^2}}, \tag{7.34}$$

where $\hat{\mathbf{p}} = (-i\hbar/a)\partial_\varphi$. The first procedure above does not work for the Rashba coupling, that is, the mean value of the ordinary velocity operator in between the Rashba wave functions does not yield the linear response result. The second, group velocity approach depends on finding an appropriate Foldy-Wouthuysen transformation we believe is not currently known in the literature.

Conclusions

We reviewed briefly a non-Abelian gauge theory suited to deal with non-relativistic quantum mechanics in the presence of various types of spin-orbit interactions. This formulation has the advantage of a correct definition of the spin current density and is a very elegant way to study spintronics.

We proposed a perfect spin filtering device based on a Mach-Zehnder type spin interferometer. The regimes of operation are subject to no limitations on the spin-orbit strengths and interferometer dimensions as in previous work. The treatment can be easily extended to unequal arm lengths and angles of incidence on the splitters. Such a generalization would provide additional parameters to manipulate filtering conditions. In the simpler analysis above involving scalar mirrors, we find both a non-tilted and tilted axis spin filtering solutions referred to the axis of quantization in which one writes the input states and for arbitrary incoming energies. The non-tilted case is not found in the scenario where the $SU(2)$ gauge field is approximated by a $U(1)$ like gauge, and is peculiar to the full non-Abelian treatment. This solution has the advantage of simplicity. On the other hand, the tilted axis solutions are shown to be well approximated by the Abelianized forms of reference [43] valid for certain reasonable conditions of SO strengths in relation to the interferometer arm lengths. When realistic mirrors/beam splitters are introduced, the mixing of the spinor components leads only to non-tilted solutions when $\pi/4$ reflections are contemplated. In this situation we run out of adjustable parameters to tune a non-tilted solution, that should be recovered when other incidence angles are considered. The qualitative scenarios for the operation of the diagonal and non-diagonal mirrors are the same and only the parameter combinations for filtering change.

Perfect filtering means that all spins in one of the detectors are polarized always in the same axis and orientation. This has the drawback that the current is not steady since the probability of producing a completely polarized electron varies with the initial projection, of the input spinor, onto the chosen quantization axis. This projection is random as electrons are injected

from the Fermi sea[48]. A density matrix approach should be implemented so that one can also assess finite temperature effects on the filter operation. It should be also noted that the interference setup does not produce a pure spin current, since polarization is accompanied by a charge current.

An interesting insight, exploiting the analogy with the Aharonov-Bohm effect in the Abelian case, comes from observing the role of Λ in the non-Abelian case. Λ and the voltage V essentially play the same role as the pair $2\pi\varphi_B$ and magnetic flux. Indeed, for a purely Pauli type SO interaction, as $\Lambda = (mL/\hbar)\alpha$ and $\alpha = \hbar eE/(m^2c^2)$, then Λ can be rewritten as $2\pi EL/(2\pi mc^2/e) = 2\pi V_E/V_0$, where $V_E = EL$, the voltage along the arm of length L in an electric field of strength E. V_0 is a quantum of voltage. Although V_0 is very large for this calculation, the material Rashba coefficient would lower it to the order of 1 eV/e.

We have analytically solved the problem of a spin-orbit active ring coupled to a voltage probe and threaded by a magnetic field. The uncoupled ring spinor wave-functions were used as a basis for the scattering problem involving a lead coupled to an electron reservoir with a zero current condition and which does not distinguish spin. The spectrum of the couple ring was obtained in terms of the density of states, that showed a broadened spectrum in direct relation to the coupling strength to the electron reservoir. The temperature only determined the electron filling of the ring and was not accounted for in the broadening of the energy levels. The level broadening was level dependent, the higher energy being more coupled than the lower. This implied a level dependent decay time for this model which will be connected to the Fermi level considered.

We also computed the equilibrium charge and spin currents in the SO active ring coupled to the reservoir and obtained their coupling dependence to the electron reservoir and their temperature dependence. While the coupling to the reservoir uniformly degraded the coherent currents the thermal effects were characteristic in the sense that currents in certain flux ranges are protected by a dispersion dependent gap to the Fermi energy. This gap can be tailored by fixing the Fermi level and or the field flux. Spin currents are obtained in steplike ranges in flux only for Rashba spin-orbit active material. The currents steps are also rounded by coupling to the reservoir, and as these currents are built from charge currents, distinguished in spin, they are endowed with the same protective gap as the former. There is then a range of fluxes where the spin current is thermally protected.

We have discussed equilibrium currents in a Corbino graphene ring, taking into account Rashba and intrinsic spin-orbit couplings separately. The ring is threaded by a magnetic flux and an

electric field perpendicular to the graphene surface in order to tune the Rashba coupling. A discussion was given for setting up the correct Hamiltonian in polar coordinates and for the spinor wave functions closure conditions. Twisted boundary conditions are discussed as a gauge freedom useful in our treatment where the magnetic flux can be translated from the Hamiltonian to the wave function. Four quantum numbers are necessary to describe the energy eigenvalues, the valley index τ the particle hole index κ, the spin-orbit quantum number δ, labeling the spin quantization axis and the angular momentum quantum number m.

The charge equilibrium currents are directly calculated from the spectrum, using linear response relations, for small magnetic fluxes (so the Zeeman coupling can be neglected) and as a function of the spin-orbit couplings. We were able to derive an explicit simple form for the four spinor in the case of zero Rashba interaction. The charge currents are induced by the magnetic flux, as expected. While spin-orbit interactions do not induce charge currents by themselves (they preserve time reversal symmetry) we showed that at a non-zero fixed flux, away from $\pm h/2e$, they can modify the charge current. This is done through the Rashba coupling that can be varied by gate voltages in the Corbino geometry.

Temperature effects have been addressed to determine wether persistent currents computed here are robust at experimentally accessible conditions. The equilibrium current turn out to be more temperature sensitive in the vicinity of integer flux, while for half-integer flux (where they are the largest) the currents are protected because they arise from contributions of levels submerged in the Fermi sea. For the SO strengths considered, equilibrium currents would be strong even at temperatures close to 1K.

We derived equilibrium spin currents on the Corbino disk, by combining charge current contributions from opposite spin-orbit labels. Spin currents only exist for Rashba type SO coupling (they cancel exactly of ISO interactions) and they exhibit the same temperature dependence as the charge currents, but in contrast, they are the more robust when their magnitude is smaller. A brief discussion was made regarding alternative definitions of equilibrium currents that are only successful for ISO type interactions. Analogous formulations for Rashba interactions are left for future work.

Bibliography

[1] Winkler R. *Spin-Orbit Coupling Effects in Two Dimensional Electron and Hole Systems* (springer). 2003.

[2] F. Guinea D. Huertas-Hernando and A. Brataas. Phys. Rev. B, 74:155426, 2006.

[3] I. Katsnelson. *Graphene, carbon in two dimensions*, cambridge university press. 2012.

[4] Dresselhaus G. Phys. Rev., 100:580, 1955.

[5] Rashba E. I. Bychkov Y. A. Sov. Phys. Solid State, 17:6039, 1984.

[6] Y. Imry M. Büttiker and R. Landauer. Phys. Lett. A, 96,, 1983.

[7] N. Bolívar A. López, E. Medina and B. Berche. Journal of Physics Condensed Matter, 22:115303, 2010.

[8] E. Medina M. Ellner, N. Bolívar and B. Berche. Physical Review B, Accepted, 2014.

[9] M. Buttiker. Phys. Rev. B, 32:1846, 1985.

[10] Tokatly I. V. Phys. Rev. Lett., 101:106601, 2008.

[11] E. Medina B. Berche and A. López. Europhysics Lett., 97:67007, 2012.

[12] A. López B. Berche, N. Bolívar and E. Medina. Condensed Matter Physics, 12:707, 2009.

[13] Bolívar N. López A., Medina E. and Berche B. arXiv:cond-mat/0902.4635., Preprint, 2009.

[14] A. H. Castro Neto et al. Rev. Mod. Phys., 81:109, 2009.

[15] F. Guinea J. González and J. Herrero. Phys. Rev. B, 79:165434, 2009.

[16] C. L. Kane and E. J. Mele. Phys. Rev. Lett., 78:1932, 1997.

[17] A. R. Akhmerov and C. W. J. Beenakker. Phys. Rev. B, 77:085423, 2008.

[18] E. Medina N. Bolívar and B. Berche. Physical Review B, 89:125413, 2014.

[19] L. Foldy and S. A. Wouthuysen. Physical Review, 78:29, 1950.

[20] P. Mohanty. Ann. Phys., 8:549, 1999.

[21] V. Chandrasekhar et al. Phys. Rev. Lett., 67:3578, 1991.

[22] D. Mailly et al. Phys. Rev., 70:1220,, 1993.

[23] Y. Aharonov and D. Bohm. Phys. Rev., 115:485, 1959.

[24] W. Ehrenberg and R. Siday. Proceedings of the Physical Society. Series B, 62:8, 1949.

[25] Datta S. and Das B. Appl. Phys. Lett., 56:665, 1990.

[26] A.A. Burkov et al. Phys. Rev. B, 70:155308, 2004.

[27] S. Zhang and Z. Yang. Phys. Rev. Lett., 94:066602, 2005.

[28] D. Xiao J. Shi, P. Zhang and Q. Niu. Phys. Rev. Lett., 96:076604, 2006.

[29] L. H. Ryder. *Quantum Field Theory*, (cambridge university press). 1985.

[30] A. Rebei and O. Heinonen. Phys. Rev. B, 73:153306, 2006.

[31] Li Y. Q Jin P. Q. and Zhang F. C. Phys. A: Math. Gen., 39:7115, 2006.

[32] A. S. Goldhaber. Phys. Rev. Lett., 62:482, 1989.

[33] Frohlich J and Studer U M. Rev. Mod. Phys., 65:733, 1993.

[34] Santiago D. I. Leurs B. W. A., Nazario Z. and Zaanen J. Ann. Phys., 323:907, 2008.

[35] Rashba E. I. Sov. Phys. Solid State, 2:1109, 1960.

[36] Nitta J. and Koga T. J. Supercond., 16:689, 2003.

[37] Fabian J. Zutić I. and Das Sarma S. Rev. Mod. Phys., 76:323, 2004.

[38] Usaj G. and Balseiro C. A. Europhys. Lett., 72:631, 2005.

[39] Peskin M. E. and Schroeder. *Quantum Field Theory*. 1995.

[40] S. Weinberg. *The Quantum Theory of Fields*. Cambridge University Press, II, 1996.

[41] E. I. Rashba. Phys. Rev. B, 70:201309, 2004.

[42] Orenstein J. Bernevig B. A. and Zhang S. C. Phys. Rev. B, 70:161302, 2004.

[43] Chen S. H. and Chang C. R. Phys. Rev. B., 77:045324, 2008.

[44] Ting D. Z. Y and Cartoixa X. Phys. Rev. B., 68:235320, 2003.

[45] Miller J. B. et al. Phys. Rev. Lett., 90:076807, 2003.

[46] et al. Studer M. Phys. Rev. Lett., 103:027201, 2009.

[47] Liu R C Oliver W D, Kim J and Yamamoto Y. Science. 284:299, 1999.

[48] M. Aranzana G. Feve. W. D. Oliver and Y. Yamamoto. Phys. Rev. B, 66:155328, 2002.

[49] Shirasaki R. Hatano N. and Nakamura H. Phys. Rev. A, 5:032107, 2007.

[50] Y. Aharonov and A. Casher. Phys. Rev. Lett., 53:319, 1984.

[51] C. Chatelain B. Berche and E. Medina. Eur. J. Phys., 31:1267, 2010.

[52] Y. Imry M. Büttiker and M. Ya. Azbel. Phys. Rev. A, 30:1982, 1984.

[53] S. Oh and C. Ryu. Phys. Rev. B, 51:13441, 1995.

[54] F. M. Peeters B. Molnár and P. Vasilopoulos. Phys. Rev. B, 69:155335, 2004.

[55] L. Brey and H. Fertig. Phys. Rev. B, 73:235411, 2006.

[56] H. Min et al. Phys. Rev. B, 74:165310, 2006.

[57] A. F. Morpurgo F. E. Meijer and T. M. Klapwijk. Phys. Rev. B, 66:033107, 2002.

[58] I. I. Cotaescu et al. J. Phys.: Condens. Matter, 19:242406, 2007.

[59] M. V. Berry C. M. Bender and A. Mandilara. J. Phys. A: Math. Gen., 35:L467, 2002.

[60] M. Mecklenburg and B. C. Regan. Phys. Rev. Lett., 106:116803, 2011.

[61] T. Nakanishi T. Ando and R. J. Saito. Phys. Soc. Jap., 67:2857, 1998.

[62] P. Recher et al. Phys. Rev. B., 76:235404, 2007.

[63] T. Nakanishi K. Wakabayashi, K. Sasaki and T. Enoki. Sci. Technol. Adv. Mater., 11:054504, 2010.

[64] E. H. Hwang D. Sarma, Shaffique Adam and E. Rossi. Rev. Mod. Phys., 83:407, 2011.

[65] J. C. Egues et al. Phys. Rev. B, 72:235326, 2005.

[66] Jaen-Seung and Hyun-Woo. Phys. Rev. B, 80:075409, 2009.

[67] D. C. Ralph F. Kuemmeth, S. Ilani and P. L. McEuen. Nature, 452:448, 2008.

[68] A. C. Blezynski-Jayich et al. Science, 326:272, 2009.

[69] L. Ci et al. Nano Research, 1:116, 2008.

[70] J. Balakrishnan et al. Nature Physics, 9:284, 2013.

[71] G. Baym. *Lectures in quantum mechanics*, westview press, new york. 1990.

Théorie de jauge non abélienne pour l'interaction spin-orbite de Rashba et Dresselhaus

Une formulation de jauge non-abélienne pour les hamiltoniens Rashba et Dresselhaus, relevants dans l'électronique de spin des matériaux non centro-symétriques est développée. Les champs de jauge définis sont proportionnels aux générateurs $SU(2)$ et aux gradients des potentiels de extrinsèque et intrinsèque d'origine, ce qui se traduit par une structure $U(1) \times SU(2)$. Nous avons déduit du lagrangien correspondant les équations du mouvement et les courants de spin conservés. On montre que la présence obligatoire d'un terme de masse de type Proca fixe la jauge et résout en conséquence la dépendance de la jauge dans le courant de spin et donc les ambiguïtés du courant de spin rapportées dans la littérature.
Nous avons analysé certaines conséquences topologiques, mettant l'accent sur les modéles d'interféromètres et l'apparition de conditions de quantification semblables à celles de l'effet Hall quantique entier.
Un dispositif de filtrage de spin par interférences est proposé dans un gaz d'électrons quasi-bidimensionnels GaAs/AlGaAs qui possède à la fois les couplages Rashba et Dresselhaus et un champ magnétique externe appliqué. Nous proposons un interféromètre de Mach Zehnder, accessible en électronique expérimentale et nous déterminons les conditions de filtrage de spin parfait. Nous trouvons deux régimes de filtrage de spin, celui oú le filtrage est réalisé dans la base de quantification du faisceau entrant, qui tire parti de la nature purement non-abélien de rotations de spin, et l'autre, oú l'on a besoin d'un axe préférentiel incliné pour observer le spineur de sortie polarisé.
Nous étudions les états électroniques d'un anneau mésoscopique en présence de couplage spin-orbite Rashba et d'un champ de jauge $U(1)$. Un couplage à un conducteur idéal est mis en œuvre à la suite de la sonde de tension de Büttiker. Les courants permanents de charge et de spin sont calculés en présence de l'interaction SO et le couplage du réservoir pour deux scénarios distincts de la fraction d'électrons de remplissage. La dégradation des courants permanents dépend de manière uniforme du couplage du réservoir.
Le problème des courants permanents de charge et de spin est également considéré sur un disque de Corbino construit à partir d'une feuille de graphène. L'hamiltonien en coordonnées cylindriques est soigneusement examinée afin de refléter hermiticité et la covariance. Nous utilisons la définition de la réponse linéaire afin de déterminer les courants persistants. Nous déterminons aussi les polarisations de spin et de pseudospin associées à ces courants d'équilibre. Les courants maximaux sont protégés contre les effets thermiques, ce qui les rend observables à des températures facilement accessibles.

Non- Abelian gauge theory for Rashba and Dresselhaus Spin-Orbit Interaction

A non-Abelian gauge formulation for the Rashba and Dresselhaus hamiltonians, relevant in spintronics of non-centrosymmetric materials, is studied. The gauge fields defined are proportional to the $SU(2)$ generators and also to potential gradients of extrinsic and intrinsic origin which results in a $U(1) \times SU(2)$ formulation. We derived from the corresponding lagrangian the equations of motion and conserved spin currents. It is shown that the mandatory presence of a Proca mass type term fixes the gauge and solves in consequence the gauge dependence of the spin current and therefore the ambiguities of the spin current reported in the literature. The invariant gauge subgroup of this theory will be studied.
We will analyze some topological consequences of the gauge formulation of Rashba and Dresselhaus focusing on interferometers models and quantization conditions similar to the integer quantum Hall effect.
A Spin filtering device, through quantum spin interference, is addressed in a quasi-2 dimensional GaAs/AlGaAs electron gas that has both Rashba and Dresselhaus spin-orbit couplings and an applied external magnetic field. We propose an experimentally feasible electronic Mach Zehnder Interferometer that determines perfect spin filtering conditions. We find two spin filtering regimes, one where filtering is achieved in the original incoming quantization basis, that takes advantage of the purely non-Abelian nature of spin rotations, and the other, where one needs a tilted preferential axis to observe the polarized output spinor.
We also address the electronic states of a mesoscopic ring in the presence of Rashba Spin Orbit coupling and a $U(1)$ gauge field. Spin symmetric coupling to an ideal lead is implemented following Büttiker's voltage probe. The spin and charge persistent currents are computed in the presence of the SO interaction and the reservoir coupling for two distinct scenarios of the electron filling fraction. The degradation of the persistent currents depends uniformly on the reservoir coupling but due to the fact that currents emerge from different depths of the fermi sea, they depend non uniformly in temperature, "shielding" the currents with a protective gap.
Finally the problem of persistent charge and spin currents is addressed on a Corbino disk built from a graphene sheet. We consistently derive the Hamiltonian including kinetic, intrinsic (ISO) and Rashba spin-orbit interactions in cylindrical coordinates. The Hamiltonian is carefully considered to reflect hermiticity and covariance. We use the linear response definition in order to determine the charge persistent currents. We also determine the spin and pseudo spin polarizations associated with such equilibrium currents. For the intrinsic case one can also compute the correct currents by properly defining the bare velocity operator associated with ISO problem or alternatively the ISO group velocity operator associated with the free case. Charge currents for both SO couplings reach maximal values in the vicinity of half integer flux quanta. Such maximal currents are protected from thermal effects because contributing levels plunge ($\sim$1K) into the Fermi sea at half integer flux values. Such a mechanism, makes them observable at readily accessible temperatures. Spin currents only arise for the Rashba coupling, due to the spin symmetry of the ISO spectrum. For the Rashba coupling, spin currents are canceled at half integer fluxes but they remain finite in the vicinity, and the same scenario above protects spin currents.

Interacción espín-órbita tipo Rashba y Dresselhaus como una teoría de calibre no-Abeliana

Se estudia una formulación de calibre no abeliana de los hamiltonianos Rashba y Dresselhaus, relevantes en espintrónica de materiales no centrosimétricos. Los campos de calibre definidos son proporcionales a los generadores $SU(2)$ y también a los gradientes de potencial de origen extrínseco e intrínseco que se traducen en una formulación $U(1) \times SU(2)$. Derivamos del Lagrangiano correspondiente las ecuaciones del movimiento y las corrientes de espín conservadas. Se demuestra que la presencia obligatoria de un término de masa tipo Proca fija el calibre y resuelve en consecuencia la dependencia de calibre en la corriente de espí y, por lo tanto, las ambigüedades asociadas a la definición de la corriente de espín reportadas en la literatura. Se estudia el subgrupo invariante de esta teoría.
Analizamos algunas de las consecuencias topológicas de la formulación de calibre de Rashba y Dresselhaus centrándonos en modelos de interferómetros y condiciones de cuantización similares al efecto Hall cuántico entero.
Se propone un dispositivo de filtrado de espín basado en interferencia cuántica de espín, en un gas de electrones cuasi-bidimiensional GaAs/AlGaAs que posee acoplamientos spin-órbita tanto Rashba como Dresselhaus y un campo magnético externo aplicado. Proponemos un interferómetro electrónico tipo Mach-Zehnder experimentalmente factible que determina perfectamente las condiciones de filtrado de espín. Nos encontramos con dos regímenes, un primer régimen donde se logra el filtrar en la base original de cuantización, que toma ventaja de la naturaleza puramente no abeliana de las rotaciones de esín, y el otro, donde se necesita un eje preferencial inclinado (tilted) para observar el espinor polarizado de salida.
Estudiamos los estados electrónicos de un anillo mesoscópico en presencia de acoplamiento espín orbita tipo Rashba y un campo de calibre $U(1)$. El acoplamiento simétrico en espín a un cable ideal se implementa siguiendo el procedimiento de punta de prueba de Büttiker. La corrientes persistentes de carga y de espín se calculan en presencia de la interacción SO acopladas con un reservorio, tomando en cuenta dos escenarios distintos para de la fracción de electrones de llenado. La degradación de las corrientes persistentes depende de manera uniforme del acoplamiento con el reservorio debido al hecho de que las corrientes emergen de diferentes profundidades del mar de Fermi, y por lo tanto para algunos regímenes particulares de flujo magnético dependen de manera no uniforme de la temperatura, produciendo un " blindaje" de las corrientes frente a la temperatura mediante una brecha de energía protectora.
Se aborda el problema de las corrientes persistentes de carga y espín en un disco Corbino, construido a partir de una hoja de grafeno. Consistentemente derivamos el Hamiltoniano incluyendo su parte cinética, interacciones espín - órbita intrínseca (ISO) y Rashba en coordenadas cilíndricas. El Hamiltoniano es construido cuidadosamente para reflejar la hermeticidad y covariancia. Utilizamos teoría de respuesta lineal con el fin de determinar las corrientes persistentes de carga. También determinamos las polarizaciones de espín y de pseudoespín asociados con estas corrientes de equilibrio. Para el caso intrínseco también se pueden calcular las corrientes definiendo correctamente el operador velocidad (bare) y calculando con las funciones de onda ISO o alternativamente, el operador de velocidad de grupo ISO para las funciones de onda libres. Las corrientes de carga para ambos acoplamientos SO alcanzan valores máximos en las proximidades de semi-enteros de cuantos de flujo. Tales corrientes máximas están protegidos de los efectos térmicos ya que los niveles que contribuyen se hunden ($\sim$ 1K) en el mar de Fermi para valores semi-enteros de flujo. Este mecanismo los hace observable a temperaturas de fácil acceso. Las corrientes de espín sólo surgen en presencia de acoplamiento Rashba, debido a la simetría de espín del espectro ISO. Para el acoplamiento Rashba, las corrientes de espín se cancelan en flujos semi-enteros pero se mantienen finitas en su vecindad. El mismo escenario anterior protege las corrientes de espín.